Fakultät für Physik der Technischen Universität München
Institut E 18

Ultra-Cold Neutron Transport and Spin Manipulation System for the Measurement of the Neutron Electric Dipole Moment

Thorsten Sven Zechlau

Vollständiger Abdruck der von der Fakultät für Physik der Technischen Universität München zur Erlangung des akademischen Grades eines

Doktors der Naturwissenschaften

genehmigten Dissertation.

Vorsitzender: Univ.-Prof. Dr. Martin Beneke

Prüfer der Dissertation:

1. Univ.-Prof. Dr. Peter Fierlinger
2. Univ.-Prof. Dr. Winfried Petry

Die Dissertation wurde am 27.09.2016 bei der Technischen Universität München eingereicht und durch die Fakultät für Physik am 21.10.2016 angenommen.

Abstract

The search for the neutron electric dipole moment (nEDM) is a key experiment in the field of low energy physics with neutrons and engages physicists since several decades. All this effort is motivated by the time (T) reversal symmetry violating nature of this phenomenon. Assuming the invariance of nature under the combined symmetry operations CPT the existence of an EDM is equivalent with CP violation. In addition this parameter is a significant contribution to the huge discrepancy between matter and antimatter. A non zero nEDM is a clear indicator for new physics beyond the Standard Model (SM). Also, in parallel the high energy physics with accelerator experiments.
So far only upper limits of the nEDM were found. Over the years, the measurements were limited by statistical precision and systematical uncertainties. To achieve better results these limits had to be improved by means of Ultra-Cold Neutrons (UCN) instead of a neutron beam. With these improvement mainly in statistical precision, also the control of systematic issues had to be enhanced.
At the Technische Universität München (TUM) a nEDM measurement with a systematic uncertainty budget of $\sigma_{d,sys} < 2 \cdot 10^{-28}$ e·cm and a statistical accuracy of $\sigma_{d,stat} < 5 \cdot 10^{-28}$ e·cm is under construction. Compared with the actual limit this is a planned improvement of two orders of magnitude for both error budgets. To reach these sensitivities all components of the apparatus have to be state-of-the-art.
Within this work the improvement of the statistical uncertainties is of major interest. Especially neutron handling and neutron spin manipulation is in the focus.
By increasing the number of detected UCNs after storage and transport, the sensitivity can be improved by the square root of the number of neutrons. Those improvements are not connected to stronger UCN sources and are invaluable for the Munich nEDM experiment. The production and characterization of neutron optical components with high transmission, high neutron optical potential and a low loss per wall collision probability, is described in this thesis. UCN guides coated with 500 nm NiMo (85/15 wt%) showed a transmission of $T_m = 96.1 \pm 0.6\,\%$ per m. The corresponding loss per wall collision was determined to be of the order of $\eta = 2.7 \pm 0.3 \cdot 10^{-4}$. Further, different UCN optical components, like bend sections, switches, shutters and beam splitters were build and characterized and showed also high transmission values.

Another factor, influencing the sensitivity linearly is the coherence time of the freely precessing spin during the measurement. This factor can be maximized by using a material in the precession chamber with a high effective neutron lifetime τ_{eff} and a high polarization lifetime T_1. Different materials have been tested for their suitability for the future Munich nEDM experiment. For a full scale nEDM precession chamber with NiMo coated electrodes and a quartz insulator an effective lifetime of 106 ± 7 s was achieved and the polarization lifetime T_1 is determined to 2307 ± 119 s. The optimization of the visibility of the two spin components was also part of this work, which influences the sensitivity linearly. Connected to this topic are also the neutron spin polarization and the spin conservation, while the UCNs are guided through the setup. Furthermore this part includes also the development and characterization of a simultaneous spin analyzer. Therefore, a so called super polarizer with a polarization power of over 99 % was developed. With this super polarizer the analyzing power of the simultaneous spin analyzing system for a precession chamber with electrodes coated with NiMo (85/15 wt%) and a quartz ring is determined to be $84 \pm 1\%$ for a storage time of 200 s. This is an improvement of approximately 20 % compared to previously visibilities in nEDM experiments.
With the developments performed in this thesis project a functioning neutron optical system and a spin guiding and manipulation system is presented and can be deployed for the future nEDM experiment.

Zusammenfassung

Seit mehreren Jahrzehnten beschäftigen sich Physiker im Forschungsbereich der Niedrigenergiephysik mit der Suche nach dem elektrischen Dipolmoment des Neutrons (nEDM). Diese Messung ist von besonderem Interesse, da ein mögliches nEDM eine direkte Verletzung der T Parität darstellt und unter Beachtung des CPT Theorems folgt somit auch eine CP Verletzung. Würde ein nEDM oder auch ein permanentes Dipolmoment eines anderen elementaren Teilchens nachgewiesen, würde dies weitere Möglichkeiten eröffnen die große Diskrepanz zwischen Materie und Antimaterie zu erklären, die mit dem Standard Modell der Teilchen (SMT) nicht erklärbar ist. Außerdem ist ein nEDM ungleich null ein eindeutiges Zeichen für neue Physik außerhalb des SMT. Neben der Hochenergiephysik mit Beschleunigerexperimenten stellen diese Messungen einen weiteren Bereich der Physik dar, um neue Physik zu untersuchen.
Alle nEDM Experimente haben bisher nur eine obere Grenze für ein elektrisches Dipolmoment aufgrund von statistischen und systematischen Grenzen finden können. Um bessere Ergebnisse zu erreichen, wurden ultrakalte Neutronen (UCN) anstatt eines Neutronenstrahls verwendet. Durch diese Verbesserung konnte eine starke Verringerung der oberen Grenze erreicht werden.
An der Technische Universität München (TUM) befindet sich zur Zeit ein nEDM Experiment im Aufbau mit dem Ziel eine systematische Unsicherheit von $\sigma_{d,sys} < 2 \cdot 10^{-28}$ e·cm und eine statistische Genauigkeit von $\sigma_{d,stat} < 5 \cdot 10^{-28}$ e·cm zu erreichen. Diese Werte liegen über zwei Größenordnungen unter dem aktuellen Grenzwert. Dieses Ziel kann nur erreicht werden, wenn alle Teilsysteme des Apparates optimiert werden und außerdem neue Methoden erprobt werden.
In dieser Arbeit wurde besonders an den Bereichen des Experiments gearbeitet, die zur Verringerung der statistischen Unsicherheiten führen. Zu diesen zählen das UCN Leitersystem und das Spin Manipulationssystem für UCN. Durch einen möglichst verlustarmen Neutronentransport kann die statistische Genauigkeit des Experiments erhöht werden. Die Anzahl der Neutronen geht mit der Wurzel in die statistische Unsicherheit ein. Die Konstruktion, Produktion und Erprobung der hierfür erforderlichen Komponenten wurde in dieser Arbeit durchgeführt. Hierbei wurde darauf geachtet, dass die verwendeten Materialien ein hohes optisches Potential und einen möglichst geringen Verlustfaktor pro Wandstoß für Neutronen haben. Unter diesen

Vorgaben wurden UCN Leiter mit 500 nm NiMo (85/15 wt%) Beschichtung hergesellt. Die Messungen ergaben eine Transmission von $T_m = 96.1 \pm 0.6\,\%$ pro m. Der Verlustfaktor ergab sich zu $\eta = 2.7 \pm 0.3 \cdot 10^{-4}$. Auch weitere benötigte neutronenoptische Komponenten wie Bögen, Switches, Shutter und Strahlteiler wurden hergestellt und charakterisiert.
Ein weiterer Faktor, der die statistische Ungenauigkeit beeinflusst ist die freie Präzissionszeit des Spins. Sie beeinflusst die statistische Genauigkeit des nEDMs linear und wird zum Einen durch die Speicherzeit der Neutronen in der Präzissionskammer beeinflusst und zum Anderen durch die Lebensdauer der Polarisation T_1 . Durch eine hohe effektive Lebensdauer und eine hohe Lebensdauer der Polarisation wird deren limitierender Einfluss auf die freie Präzissionszeit des Spins verringert. Hierfür wurden verschiedene Konfigurationen von Materialen getestet. Für eine nEDM Kammer mit Elektroden, beschichtet mit einer NiMo (85/15 wt%) Legierung und einem Isolatorring aus Quarz ergab sich eine effektive Neutronen Lebensdauer von $106 \pm 7\,$s. Die zugehörige Lebensdauer der Polarisation wurde zu $T_1 = 2307 \pm 119\,$s bestimmt. Der Kontrast zwischen den Spinorientierungen geht linear in die statistische Genauigkeit ein und ist ein Maß für die Depolarisation im Experiment. Zur Verbesserung des Kontrastes zwischen den Spinorientierungen wurden im Rahmen dieser Arbeit Systeme entwickelt, gebaut und erprobt. Zur Untersuchung muss die Polarisation des Spins und dessen erhalt auf dem Weg durch das gesamte Experiment untersucht werden.
Ein System zur simultanen Spin Analyse wurde ebenso im Rahmen dieser Arbeit entwickelt. Hierfür wurden sogenannte Super Polarisatoren entwickelt, die eine Polarisation von über 99 % ermöglichen. Das System zur simultanen Spin Analyse erreichte eine Kontrast zwischen den Spinorientierungen für eine Präzessionskammer, beschichtet mit NiMo (85/15 wt%) und einem Quarz Isolatorring von $84 \pm 1\%$ bei einer Speicherzeit von 200 s.
Mit den in dieser Arbeit vorgestellten Entwicklungen wurde ein funktionierendes Neutronenleiter System entwickelt. Außerdem wurde ein Spin Transport- und Manipulations-System entwickelt. Alle Komponenten können für ein zukünftiges nEDM Experiment in München eingesetzt werden.

Contents

Chapter 1

Introduction

1.1 Motivation and Status

For clearing the remaining open questions in the early universe high precision measurements with ultra cold neutrons (UCNs) are of major interest. In the following sections the theoretical background concerning the properties of UCN (Ch.1.2.1) and their production (Ch.1.2.2). Further in Ch. 1.3 all required technologies concerning the measurement of the electric dipole moment of the neutron (nEDM) are described.

1.1.1 The Importance of the nEDM Measurement

Based on the well known concept of variation of Ramsey's technique of separated oscillatory fields, which employs the Zeeman interaction of the spin with a magnetic field, the intend of the future nEDM is to perform precision clock comparison measurements preferably deploying the new source of UCN at the Forschungs-Neutronenquelle Heinz Maier-Leibnitz (FRMII) research reactor in Garching. The concept extends proven and already known technologies of former measurements with the goal to achieve a statistical limit of $< 5 \cdot 10^{-28}$ e·cm and a corresponding budget of systematic uncertainties of $< 2 \cdot 10^{-28}$ e·cm. The main improvements are (i) a strong source of UCN, (ii) sufficient control of magnetic and electric fields, (iii) improved storage times of the EDM measurement chambers, which should exceed > 250s, (iv) improved UCN polarization $> 98\%$ and (v) improved possibilities to test for systematic effects.

1.1.2 nEDM Experiments: State-of-the-Art

Since fundamental interactions in the Standard Model (SM) of particle physics are dominated by symmetries and their violation, physicists are searching especially for symmetry breaking processes to solve the mystery of the early Universe. This is tried with on the one hand with high precision experiments like EDMs and on the other hand with high energy regions up to a total collision energy of 14 TeV like at the Large Hadron Collider (LHC) at Cern [1].
With the discovery of the proposed Higgs Boson an important missing puzzle piece in the SM at the LHC at Cern [2] and [3] by Peter W. Higgs [4] and Francois Englert in 1964 [5] predicted , the search for EDMs is the most promising way to find physics beyond the SM. However, there are still a lot of open questions left in the SM, like the nature of Dark Matter or the baryon asymmetry problem. The latter is manifested in the discrepancy between matter and antimatter. By measurements of the Cosmic Microwave Background Radiation the ratio of the baryon and anti baryon number densities to the photon number density is calculated to be [6]:

$$\eta = \frac{n_b - n_{\bar{b}}}{n_\gamma} = 6.14 \pm 0.25 \cdot 10^{-10}. \tag{1.1}$$

In 1967 Sakharov [7] formulated three fundamental condition to be satisfied for a Baryon asymmetry, if the universe is symmetric at $t = 0$.

- There have to be interactions in the SM, where the Baryon number has to be violated.
- The thermodynamical equilibrium has to be perturbed.
- The fundamental Charge (C) and Charge & Parity (CP) symmetries have to be broken during interactions.

But so far the discovered CP violations in processes, like the K^0 decay [8] or the B meson oscillations [9] are to small to explain the matter antimatter mystery.
Therefore the measurements of EDMs become key experiments to understand these processes in the early Universe. An EDM of a fundamental particle would be equivalent to the fact of a broken fundamental symmetry in the early universe and an indication of physics beyond the SM. The goal of all EDM experiments is to measure the effective interaction energy of the particle of interest with an electric field. If an EDM exists a splitting like the Zeeman effect for magnetic fields would occur for an electric field. Such an effect is not invariant under parity and time reversal symmetry operation. Following the CPT theorem [10] CP is also broken. So far only

an upper limit for EDMs of fundamental particles can be given by experiments (see Tab. 1.1). Nevertheless in SM the EDMs are predicted but the calculated values are beyond the current limits of actual experiments (for neutron EDM compare Fig.1.1). Tab. 1.1 illustrates the discrepancy for some fundamental particles between the SM model prediction and the actual experimental limit. But for proofing charge and parity non-invariance in supersymmetry the limits of actual EDM measurements is acceptable.

	Exp. limit [e·cm]	SM prediction [e·cm]
Electron	$8.7{\cdot}10^{-29}$(90%CL) [11]	10^{-40} [12]
Neutron	$2.9{\cdot}10^{-26}$(90%CL) [13]	10^{-33}-10^{-31} [14]
^{199}Hg	$3.1{\cdot}10^{-29}$(95%CL) [15]	

Table 1.1: Experimental limits and SM prediction of some fundamental particles

As depicted in Fig. 1.1 and Tab. 1.1 the experimental limit so far is accomplished by the RAL-Sussex-ILL collaboration in 2006 [13], with an upper limit on the neutron EDM of $d_n < 2.9 \cdot 10^{-26}$ e·cm. Further analysis and with new awareness a new limit with $d_n < 3.0 \cdot 10^{-26}$ e·cm for a nEDM was published in 2015 [16].
One of the most promising concepts to reach the SM prediction in Tab. 1.1 listed for the nEDM are CryoEDMs. Here the entire instrument is working in a cryogenic environment at a temperature region of 0.7 K [17]. The UCN are produced in a super thermal UCNs source and stored within the super fluid Helium in a storage cell [18]. Here, a magnetic and an electric field is applied on the stored UCN. This concept has the big advantage of much higher UCN densities in the storage chamber, but the construction is much more complex than for a room temperature nEDM. Such an EDM was started to build with the CryoEDM [17], [19], [20] at the ILL, but had to be stopped because of funding issues.

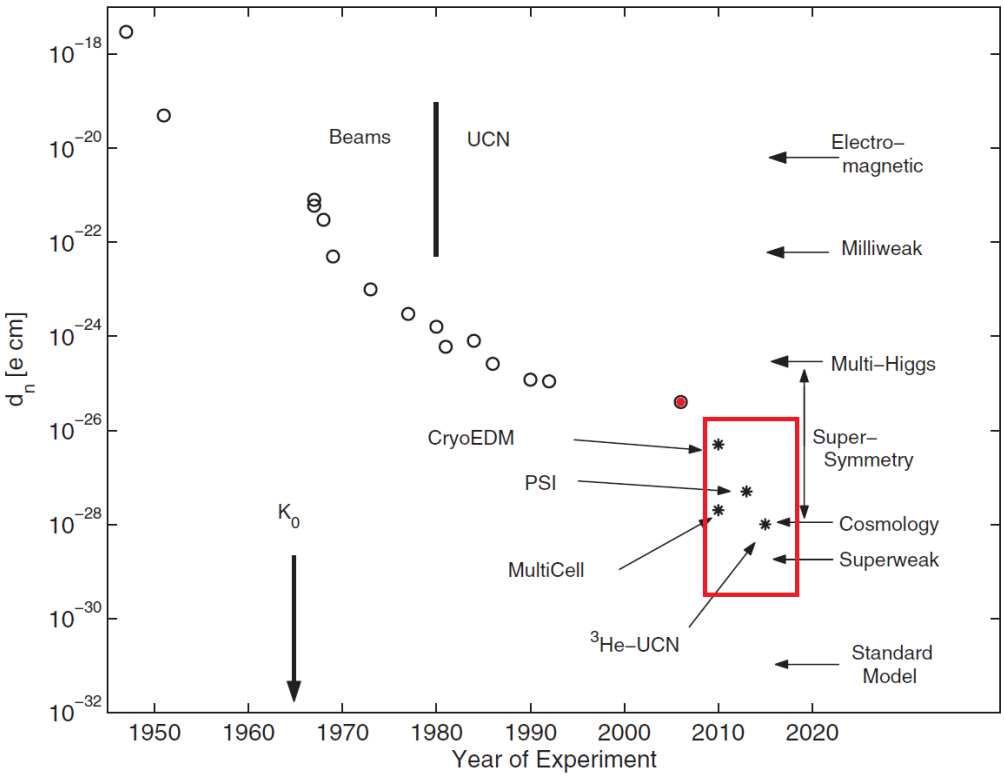

Figure 1.1: Time line of the sensitivity of nEDM research. The red marked value is the current upper limit on the neutron EDM of $d_n < 2.9 \cdot 10^{-26}$ e·cm [13]. Stars in the red marked box are illustrating the goals of current and future experiments. The in the red box shown experiments are delayed because of different reasons and have to be shifted to the 2020 region. Taken from [12] Fig.1

1.2 Ultra-Cold Neutrons

Since the discovery of the neutron in 1932 by Chadwick, a lot of different experiments with this particle were performed. The free neutron participates on all fundamental interactions, except the interaction with an electric field due to its neutrality. Further, more the success of nEDM projects all over the world is strongly linked to the characteristics of the free neutron especially the UCNs, which will be discussed in Ch. 1.2.1 following [21] and [22]. In Ch. 1.2.2 the different possibilities of producing UCN will be depicted.

1.2.1 Properties and Interaction of Neutrons

As a Baryon the neutron is composed of one up quark and two down quarks. The scattering cross section of the neutron is strongly associated with the velocity of the neutron and it is possible to classify them according to this, as shown in Tab. 1.2. With the following equation the energy (E) of the neutrons can be converted into their velocity or the de Broglie wavelength:

$$E = \frac{1}{2}mv^2 = \frac{h^2}{2m\lambda^2} \tag{1.2}$$

Here h is the Planck constant and λ is the wavelength of the neutron.

Name	Energy E [eV]	Velocity v[m/s]
Ultracold Neutrons	$< 0.3 \cdot 10^{-6}$	< 8
Very cold Neutrons	$0.3 \cdot 10^{-6}$ ... $0.05 \cdot 10^{-3}$	8 ... 100
Cold Neutrons	$0.05 \cdot 10^{-3}$... $25 \cdot 10^{-3}$	100 ... 2000
Thermal Neutrons	... $25 \cdot 10^{-3}$	... 2200
Epithermal Neutrons	0.1 ... $500 \cdot 10^{3}$	4400 ... $1 \cdot 10^{7}$
Fast Neutrons	$> 500 \cdot 10^{3}$	$> \cdot 10^{7}$

Table 1.2: Classification of neutrons by their energy and velocity

Weak Interaction

As previously mentioned the neutron underlies weak interactions. The mean lifetime of the free neutron is $\tau_n = (880.3 \pm 1.1)$s [23]. Because of this interaction the free neutron is not stable and decays in the following reaction

$$n \longrightarrow p + e + \bar{\nu}_e + 782keV \tag{1.3}$$

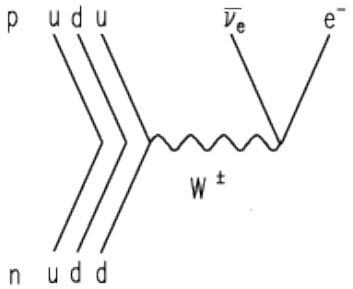

Figure 1.2: Feynman diagram of the neutron β^- decay. One d-quark changes its flavour into an u-quark and a W^- boson is emitted and decays in an electron and a $\bar{\nu}_e$. Figure taken from [24]

In this reaction a d-quark is transferred to an u-quark inside a nucleus and the neutron becomes a proton. In this interaction a W^- boson is interchanged, which decays into an electron and an anti electron neutrino. In the Standard Model of particle physics this decay is described by semileptonic vector and axial vector currents and is linked by the following equation with the first element of the quark mixing matrix (CKM- matrix):

$$|V_{ud}|^2 = \frac{(4908.7 \pm 1.9)s}{\tau_n(1 + 3\lambda^2)} \tag{1.4}$$

with $\lambda = g_A/g_V$ is the ratio of the current coupling strengths and τ_n is the free neutron lifetime. The coupling strength can be extracted from the probability distribution of the β- decay defined by:

$$W dE_e d\Omega_e d\Omega_\nu \sim p_e E_e (E_0 - E_e)^2 dE_e d\Omega_e d\Omega_\nu \tag{1.5}$$

$$\times \left[1 + a\frac{\vec{p}_e\vec{p}_\nu}{E_e E_\nu} + b\frac{m_e}{E_e} + \langle\vec{\sigma}_n\rangle\left(A\frac{\vec{p}_e}{E_e} + B\frac{\vec{p}_\nu}{E_\nu} + D\frac{\vec{p}_e \times \vec{p}_\nu}{E_e E_\nu}\right)\right] \tag{1.6}$$

here p represents the momentum, E the energy and σ the spin of the neutron and its decay products. The coefficients a, b, A, B and D are derived from experiments measuring correlations between the neutron spin and the decay products as listed below: The parametrization for the free neutron decay with Φ is the angle between

a	$=$	$\frac{1-\lvert\lambda\rvert^2}{1+3\lvert\lambda\rvert^2}$	$=$	-0.103 ± 0.0029	electron - antineutrino asymmetry
b	$=$	0	$=$	0	Fierz interference
A	$=$	$-2\frac{\lvert\lambda\rvert^2+\lvert\lambda\rvert\cos\Phi}{1+3\lvert\lambda\rvert^2}$	$=$	-0.1173 ± 0.0013	spin-electron asymmetry
B	$=$	$2\frac{\lvert\lambda\rvert^2-\lvert\lambda\rvert\cos\Phi}{1+3\lvert\lambda\rvert^2}$	$=$	-0.981 ± 0.004	spin-anti neutrino asymmetry
D	$=$	$\frac{\lvert\lambda\rvert\sin\Phi}{1+3\lvert\lambda\rvert^2}$	$=$	$-4 \pm 6 \cdot 10^{-4}$	T-odd triple-product

the coupling constants g_A and g_V. The equations and values are taken from [25]. Beside the mean neutron lifetime, which is a main parameter to investigate the unitarity of the CKM matrix and for testing the standard model of particles. These relations between the products are investigated in different experiments, like by the collaborations Perkeo III [24] and Perc [26].

Magnetic Interaction

As a fermion with a 1/2 spin the neutron has a magnetic moment $\mu_n = \gamma \cdot \vec{S}$, whose orientation is contrary to the neutron spin. γ is the gyromagnetic ratio and is given by $\gamma = -183.25 MHz/T$. $\vec{S}$ is the neutron spin and defined as $\frac{1}{2}\hbar\vec{\sigma}$. With the magnetic moment μ_n the neutron couples to a magnetic fields $\vec{B}$. The negative magnetic moment can be described as $\mu_n = -1,91\,\mu_K$, with the nuclear magneton $\mu_N = \frac{e\hbar}{2m_P}$. If a neutron interacts with an inhomogeneous magnetic field it experiences the Stern- Gerlach force:

$$\vec{F}_m = -\nabla[-\vec{\mu_n} \cdot \vec{B}] = \pm\,|\vec{\mu}_n|\,\nabla|\vec{B}| \tag{1.7}$$

Following this equation neutrons with spin parallel to the field will be accelerated to higher field strength, neutrons with an anti parallel direction are repelled.
For the magnetic potential in an external magnetic field can be described by:

$$V_m = -\vec{\mu}_n \cdot \vec{B} = \pm 60,3\ neV/T \cdot B \tag{1.8}$$

The algebraic sign results from the relative direction of the spin to the magnetic field.
The interaction of a neutron with a magnetic field results in a Zeeman splitting of the kinetic energy of

$$\Delta E_{kin} = 2\,|\mu|\,B \approx 120\frac{neV}{T} \cdot B \tag{1.9}$$

If neutrons enter a strong magnetic field spin up neutrons will be decelerated by the interaction and reflected. Following this theory the transmitted part is 100 %

polarized. More details on this can be found in Ch.1.3.4 section Polarizing UCNs. The magnetic interaction enables experiments using polarized neutrons and high magnetic fields in the Tesla regime. It is possible to store polarized neutrons in magnetic bottle as it is planned for the Penelope experiment [27].

Gravitational Interaction

For most experiments in particle physics gravitational interaction is negligible. But for experiments with UCNs, corresponding to a kinetic energy of a few 100 neV this is not possible, because the energy of the neutrons is in the same order of magnitude. In the earth gravitational field the potential of a neutron with a mass of $m_n = 939,56\ MeV$ is given by

$$V_g = m_n \cdot g \cdot h = 102 \cdot 10^{-9}\ eV \tag{1.10}$$

With this interaction the UCN spectrum can be manipulated by guiding the neutrons upwards or downwards. Hence, this effect is an useful tool to adjust the energy spectrum in storage experiments, like in nEDM measurements. It is also applied in lifetime experiments for storing UCN with a certain energy like in [28]. The acceleration of an UCN in the gravitational field is also used for passing the separation window in an UCN detector or an analyzing foil coated with iron as will be described in Ch. 6.

Strong Interaction and Theoretical Contemplation for Neutron Optics

Protons and neutrons are bound by strong interaction in the nucleus. The binding force between the nucleons can be approached at low energies as a spherical square-well potential with a depth of ≈ 50 MeV. The radius is defined as $R = R_0 \cdot A^{1/3}$ with $R_0 = 1{,}21$ fm.
There are two possibilities for collisions of neutrons with a nucleus. The neutron can be scattered or absorbed, where scattering can be elastic and inelastic. However, the scattering process can not be described by perturbation theory, since the energy of the UCN and the nucleus differ drastically from each other. To solve this problem Fermi introduced a pseudo potential for the nuclear potential using a δ-function.The

pseudo potential enabled him to use perturbation theory to describe the scattering process.
The wave function of a neutron, scattered by a nucleus, can be described by an incoming plane wave and a scattered spherical wave with an angle dependent scattering amplitude $f(\Theta)$:

$$\Psi = e^{i\vec{k}\cdot\vec{r}} + f(\Theta)\frac{e^{ikr}}{r} \tag{1.11}$$

where $\vec{k}$ is the wave vector of the free neutron. Since the neutron De Broglie wavelength is much lager than the interaction length of the strong interaction, there will be no angular momentum exchange and the interaction is predominated by a s - wave scattering. Hence the scattering amplitude becomes scattering angle independent and is given by the negative scattering length a:

$$f(\Theta) = const. = -a \tag{1.12}$$

A very slow neutron will always interact with a multitude of nuclei due to its large wavelength. Therefore, the resulting pseudo potential is a superposition of all nuclei and can be described as a sum of the potential at the position $\vec{r_i}$ with a scattering length a_i

$$V_F(\vec{r}) = \frac{2\pi\hbar^2}{m_n}\sum_i a_i\delta(\vec{r} - \vec{r_i}) \tag{1.13}$$

with m_n being the neutron mass. For slow neutron a huge amount of pseudo potential are in the range of the wavelength which results in an interference of all scattered waves and the potential becomes:

$$V_F(\vec{r}) = \frac{2\pi\hbar^2}{m_n}\sum_j a_j N_j \tag{1.14}$$

where N_j is the number density of molecules and a_j is the scattering length of the material.
In UCN physics this potential is known as the neutron optical potential or Fermi Potential, saying that neutrons with an energy $E < V_F$ will be reflected from the surface under any angle of incidence. Tab. 1.3 shows a collection of the most common materials used in UCN physics with their neutron optical potential and the corresponding loss coefficient.

Nevertheless UCNs also can get lost although their energy is less than the neutron optical potential. However, while the neutron is reflected from the material a part of

its wave function penetrates the material as an evanescent wave (see Fig. 1.3). The following two processes lead to UCN losses in matter. First the up scattering process describes an energy transfer from UCN to the material, which is discussed in Ch. 1.2.2 for UCN production. The UCN absorbs a phonon in the reflecting material. By this absorption the energy rises and the neutron will not be reflected from the wall material, crosses it unhindered and gets lost. The up scattering probability is represented by the cross section σ_u and increases with the material temperature.
Second, the UCN can be captured by a nucleus in the material by absorption. The probability is described by the cross section σ_a. The sum of these two results in the total loss cross section

$$\sigma = \sigma_u + \sigma_a \tag{1.15}$$

. These losses due to absorption and up scattering arise from the finite probability density inside the material for the neutron, leading to an imaginary potential W. This potential has to be considered in the neutron optical potential as follows:

$$U = V_F - \imath W \tag{1.16}$$

here W is defined by:

$$W = \frac{\hbar}{2} \sum_j N_j \sigma_j v_n \tag{1.17}$$

σ_j is the total loss cross section for the material and N_j is the number density of molecules. Using this Equation and Equation 1.14 the neutron optical potential is given by:

$$U = \frac{2\pi\hbar^2}{m} N \left(a_r - \imath \frac{m_n v_n}{4\pi} \sigma \right) \tag{1.18}$$

Equation 1.17 shows the proportionality of the imaginary part to the total loss cross section σ_j. Because $\sigma_j \propto 1/v_n$, W becomes independent of the neutron velocity.
The ratio of the imaginary part and the real part of U in Equation 1.18 is known as the loss factor for a material:

$$\eta = \frac{W}{V_F} = \frac{m_n v_n \sigma}{4\pi\hbar a} = \frac{p_n \sigma}{2ha} = \frac{\sigma}{2a\lambda_{dB}} \tag{1.19}$$

Here the definition of the De Broglie wavelength $\lambda_{dB} = h/p$ was used. For guiding or storing UCN a high V_F with a low W is claimed. This is a measure of the suitability of a material for neutron physics. For an absorbing material η can reach values up to 1. In Tab.1.3 the ratio η is given for materials used in UCN experiments. Since W and V are velocity independent, also η is a velocity independent loss factor.
For the interaction of a neutron with a step potential, like depict in Fig. 1.3, the

reflection coefficient for $W \ll V_F$ results in:

$$|R|^2 = 1 - 2\eta \left(\frac{E_\perp}{V_F - E_\perp} \right)^{\frac{1}{2}} = 1 - 2\eta \left(\frac{E cos^2\theta}{V_F - E cos^2\theta} \right)^{\frac{1}{2}} \equiv 1 - \mu(E, \theta) \tag{1.20}$$

here $\mu(E, \theta)$ is the loss probability per wall bounce and θ is the angle of incidence to the surface normal.
If the UCNs are stored in a chamber they perform several wall collisions and the UCNs are isotropic. With this assumption μ can be averaged over the angle of incidence for a given energy and the rate of particles incident on a surface is proportional to

$$\cos\theta d\Omega = 2\pi \cos\theta \sin\theta d\theta = 2\pi \cos\theta d(\cos\theta) \tag{1.21}$$

With this the average loss probability per bounce for UCN of energy E is defined by

$$\bar{\mu}(E) = 2 \int_0^1 \mu(E, \theta) \cos\theta d(\cos\theta) \tag{1.22}$$

$$\bar{\mu}(E) = 2\eta \left[\frac{V}{E} \cdot \arcsin \left(\frac{E}{V} \right)^{1/2} - \left(\frac{V}{E} - 1 \right)^{1/2} \right] \tag{1.23}$$

With this Equation the following relation follows for $E/V = 0.5$: $\bar{\mu} = \eta$.

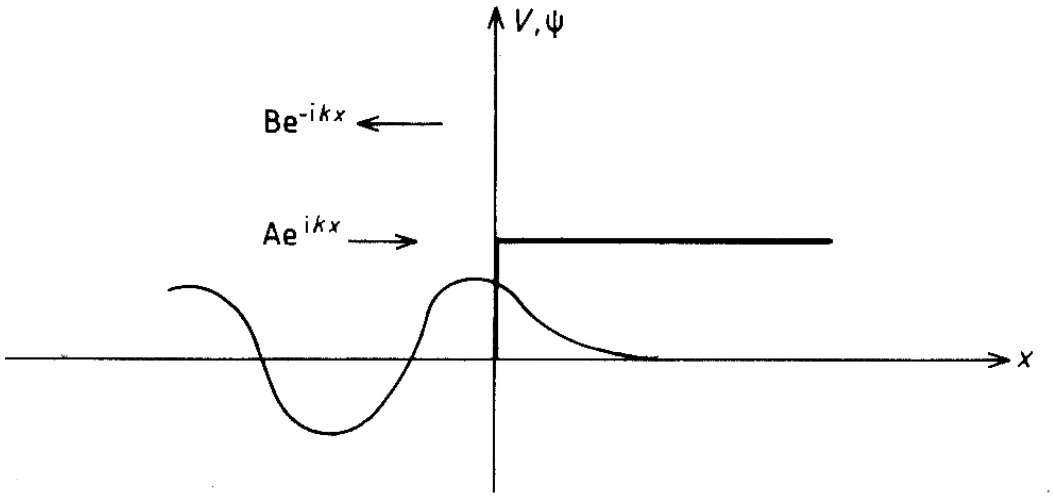

Figure 1.3: Neutron wave function of a neutron reflected at a step potential. For an energy $E < V_F$ the neutron has a finite probability density inside the material. Taken from [21] p.19

Comparing the energy ($\approx -50\,\text{MeV}$) and the range of the nucleus potential ($10^{-15}\,\text{m}$ with the energy $\approx 100\,\text{neV}$) and the wavelength of UCN ($10^{-8}\,\text{m}$), it shows

Material	V_F [neV]	$\eta = W/V_F$
Ni^{58}	335	$8.6 \cdot 10^{-5}$
BeO	261	$1.35 \cdot 10^{-5}$
Ni	252	$12.5 \cdot 10^{-5}$
Be	252	$0.5 \cdot 10^{-5}$
Cu	168	$15.5 \cdot 10^{-5}$
Ti	- 48	-
Al	54	$2.25 \cdot 10^{-5}$
Diamond-like carbon (DLC)	249 [29]	$3.1 \cdot 10^{-4}$ [30]
NiMo (85/15 wt%)	221 (see Ch. 3.2)	$2.5 \cdot 10^{-4}$ (see Ch.3.2)
Deuterated polyethylene (dPE)	214 [31]	$1.3 \cdot 10^{-4}$ [31]
SiO_2 (quartz)	95 [32]	$4 \cdot 10^{-4}$ [32]

Table 1.3: Neutron optical potentials and loss coefficients of different frequently used materials for guiding and storing UCNs. If not else referred, the values are taken from [21].

a clear discrepancy of many orders of magnitude. Therefore this process is almost independent of the energy of the neutron. Considering this, the absorption cross section σ_a shows a $1/v$ dependence for energies lower than 1 eV.

1.2.2 UCN Production

Free neutrons decay due to weak interaction, as previously described in Ch. 1.2.1, therefore neutrons only exist bounded in nuclei. Hence, free neutrons have to be produced continuous, for the use in experiments by setting them free from the nuclei in two different nuclear reactions.
The first possible process is spallation, like it is used at the Paul Scherrer Institut (PSI) in Villingen or the European Spallation Source (ESS) in Lund. The second possibility is to make use of nuclear fission in reactors such as done at the ILL or at Forschungsneutronenquelle Heinz Maier-Leibnitz (FRMII) in Garching. In both processes fast neutrons (Tab. 1.2) are released and have be moderated with different materials such as H_2O, D_2O or graphite to thermal neutrons (Tab. 1.2). The neutrons reach a thermal equilibrium with the moderator. For further cooling a cold moderator like liquid hydrogen or deuterium are employed to reach energies of about 2 meV.
A further energy loss can be achieved by extracting UCNs from the lower energy tail

of the Maxwell-Boltzmann distribution, referred to as the thermal UCN source, or by inelastic down scattering in a superthermal UCN source, which will be described in the following section.

UCN Source of the past

The concept of a thermal UCN source is based on the thermal equilibrium with the moderating material. For this process the neutron temperature and the moderator temperature have to be comparable equal. The UCNs temperature is of the order of a few mK. In a reactor environment this equilibrium is not achievable due to the heat load of the fission. The Maxwell-Boltzmann distribution for neutrons in thermal equilibrium is given by [21]:

$$\frac{d\phi}{dE} = \Phi_0 \frac{E}{(k_B T_{mod})^2} e^{-\frac{E}{k_B T_{mod}}} \tag{1.24}$$

where ϕ_0 is the total neutron flux and k_B the Boltzmann- constant. A lower temperature of the moderator (E < V_F) leads to a higher amount of UCN in the Maxwell-Boltzmann distribution as it is shown in Fig. 1.4.

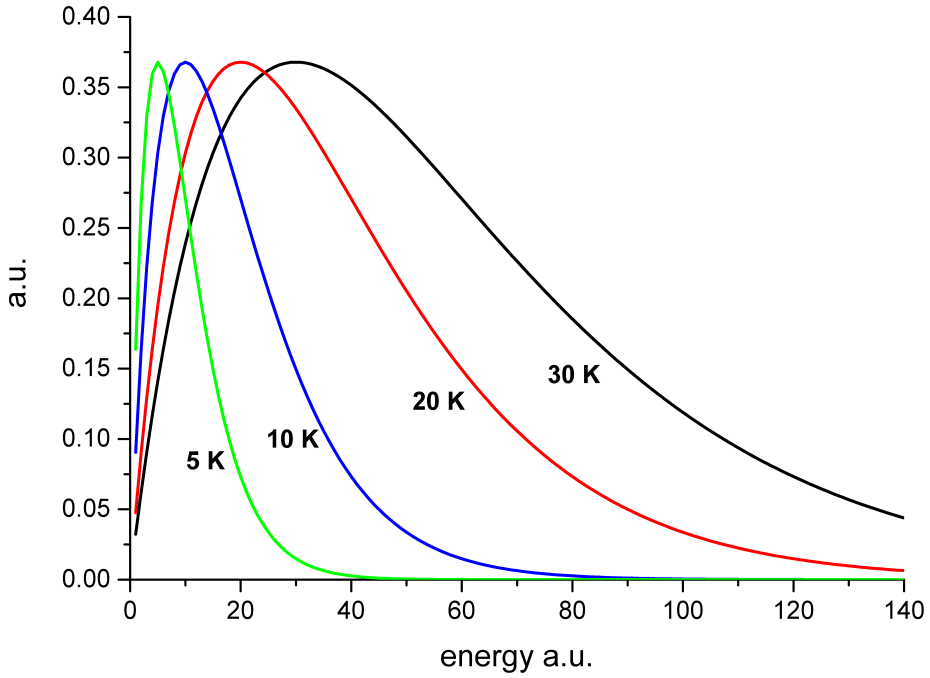

Figure 1.4: Illustration of the temperature dependence of the Maxwell-Boltzmann distribution described by equation 1.24.

The UCN density in a thermal source with walls of a Fermi potential V_F is defined as:

$$\rho_{UCN} = \int_0^{V_F} \frac{1}{v}\left(\frac{d\Phi}{dE}dE\right) = \frac{2}{3}\frac{\Phi_0}{\alpha}\left(\frac{V_F}{k_B T_{mod}}\right)^{\frac{3}{2}} \tag{1.25}$$

with $\alpha = (2k_B T_{mod}/m_N)^{1/2}$, T_{mod} is the temperature of the moderator and Φ_0 is the total thermal flux. The most powerful UCN source at present days is at the ILL in Grenoble [33]. In the cold source [Fig.1.5 (1)] the UCN density is of the order of $\approx$ 1000 UCN/cm^3, but these UCNs are not directly useable because they are confined by the wall potential of the vessel. Therefore, VCN with a velocity of $\approx$ 50 m/s are extracted and guided through a vertical guide [Fig.1.5 (2)] upwards to slow down the neutrons by the gravitational interaction mentioned in Ch. 1.2.1. Part (3) of Fig. 1.5 shows the upper part of the guide, which is curved to reduce the high energy neutron flux and the γ load at the exit. At the upper end of the guide the Steyerl Turbine is installed [Fig.1.5 (4)], serving as a mechanical UCN generator. It is build of many neutron reflecting mirrors mounted on a rotating wheel, with a velocity of $u \approx v/2$ away from the incident neutrons. Here v is the velocity of the neutrons. Following this the reflected neutrons have a velocity of:

$$v' = v - 2u \approx 0. \tag{1.26}$$

The so slowed down VCNs are behind the turbine UCN [Fig.1.5 (5)] and are divided by a switch to the different experiment places.

More technical details and the characterization can be found in [34] and [35]. This source delivers an UCN density of 50 UCN/cm^3 at the turbine exit [33] and at the different beam positions up to 10 UCN/cm^3 under optimal conditions.

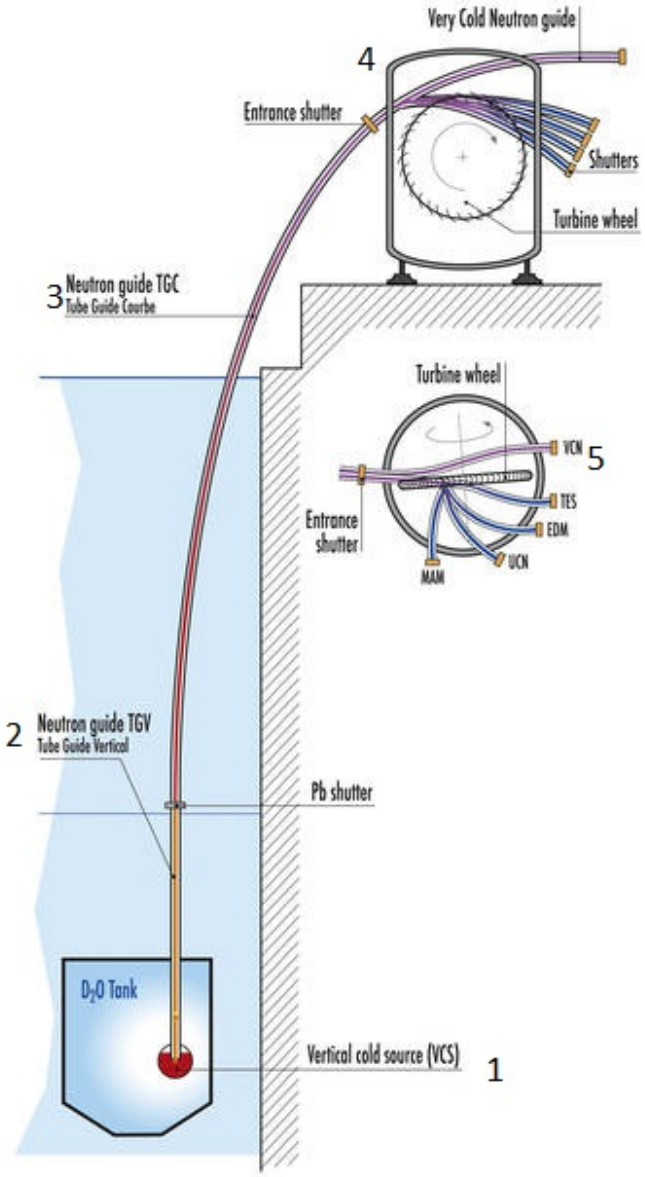

Figure 1.5: Schematic illustration of the UCN source at the ILL. Sections are: (1) Cold source, (2) vertical guide, (3) vertical guide with smooth bending, (4) turbine, (5) distribution to the experimental area. Taken from [33].

Super-thermal UCN Sources of the future

The concept of a super-thermal UCN source is based on scattering incident neutrons at a converter material, where the neutron looses its kinetic energy almost completely [21], [36]. In contrast to a thermal source here the neutron is not in thermal equilibrium with the moderator.
The converter has a ground state $E_0 \approx E_{UCN}$ and an excited state $E_0 + \Delta$. If the

converter material is cold enough, corresponding to $E_0 \ll \Delta$, almost all particles will populate to the ground state. Only few particles have enough energy to occupy the excited energy level. Following [21] the probability for a transition from the ground state to the excited state is defined as:

$$\sigma\left(E_0 \rightarrow E_0 + \Delta\right) = \frac{E_0 + \Delta}{E_0} e^{-\Delta/(k_B T_{konv})} \cdot \sigma\left(E_0 + \Delta \rightarrow E_0\right) \tag{1.27}$$

here $\sigma\left(E_0 + \Delta \rightarrow E_0\right)$ is the inelastic cross- section of the down scattering and T_{konv} the temperature of the converter. From equation 1.27 follows, that the up scattering process becomes negligible, because the Boltzmann function is temperature dependent.

A neutron flux with a temperature of $T_0 \approx \Delta$ will interact with the converter, hence the neutrons will be down scattered into the energy region of $E_0 \approx E_{UCN}$ while the converter material is excited to an upper energy level. By cooling the converter this heat load can be redirected away from the source and the reverse process, the upscattering, will be suppressed. With this kind of source the UCN production rates in the converter material is high. However, it is the challenge to extract the neutrons from the converter material without loosing to many neutrons.
The described two level system can be achieved with super fluid ^4He as converter material. More details on this converter material can be found in [37]. UCN sources using super fluid ^{4}He were build at the ILL [38] [39] and at KEK in Japan [40].
For deuterium the described two level system is not suitable, because deuterium is a molecule with more degrees of freedom compared to helium. Although the temperature of the converter is low the occupation of the phonon states is further possible. This results in a higher up scattering probability. In principle for such a process the UCN density in the crystal grows proportional to $(E_{UCN}/\Delta)e^{\Delta/k_B T}$ (see Fig. 1.6). Here the UCN density scales with the converter temperature $1/T^2$. For the case $T_0 = T \ll \Delta$ (Fig. 1.6) the super thermal enhancement is not expected any more.
The production for UCN per second in a volume V is definded as [21]:

$$P = N \int_0^{E_{UCN}} \int_0^{\infty} \frac{d\Phi_0}{dE_n} \cdot \sigma_{down}(E_n, E') \cdot dE_n dE' \tag{1.28}$$

here N is the particle density in the converter, $\sigma_{down}(E_n, E')$ the cross section for down scattering with an energy E_n for the incident neutrons and $d\Phi_0/dE_n$ is the incident differential neutron flux. Due to the one- phonon- approximation the production rate is direct dependent from the phonon excitation spectrum.
Using Deuterium as a converter implies also different loss channels. The first loss

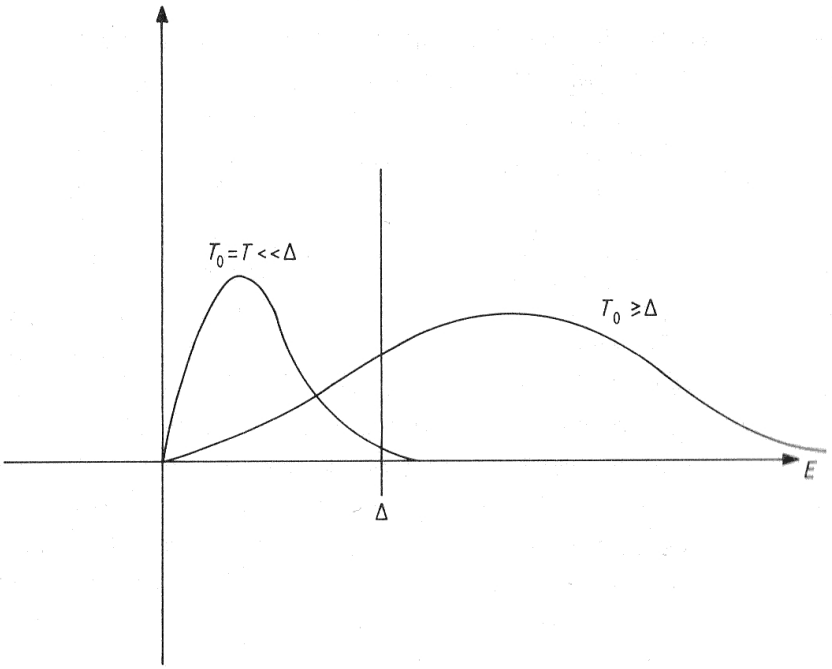

Figure 1.6: The figure shows the Maxwell Boltzmann energy distribution in equilibrium at a temperature of $T_0 \ll \Delta$ and $T_0 \geq \Delta$, here Δ is the excitation energy of a two level system. Taken from [21].

possibility is given by absorption in the deuterium converter. By the reaction

$$d + n \rightarrow t + \gamma \tag{1.29}$$

neutrons can get lost with a cross section of $\sigma_{abs}(therm.) = 5,19 \cdot 10^{-4}\, barn$ [41]. A second process for UCN losses is owing to the pollution of the deuterium by hydrogen and is described by

$$p + n \rightarrow d + \gamma \tag{1.30}$$

The absorption cross section for hydrogen is $\sigma_{abs}(therm.) = 0,3326\, barn$ [41] and is much higher than for deuterium. To suppress this loss channel a high deuterium purity is necessary.
An additional loss possibility is given by up scattering due to phonons, which can be suppressed in a low temperature regime being in the same magnitude as other loss processes [42]. UCNs can also be lost by a spin flip due to para- deuterium leading to an energy gain. These neutrons are no longer storeable and are therefore lost. This can be suppressed by using a high enriched ortho- deuterium in the low energy spin state [42]. By virtue of these loss channels the mean free path for neutrons in a deuterium converter can be calculated to $\lambda \approx 6,2\,\mathrm{cm}$ [42]. Following this the UCN lifetime in the deuterium is $\tau_n \approx 21\,\mathrm{ms}$ [42]. The very low neutron lifetime in the

crystal limits the thickness of the deuterium converter crystal.
UCN sources based on deuterium were build at spallation sources or reactors all over the world. The current running UCN sources based on this concept deliver UCN densities up to 34 UCN/cm^3 [43] in experiments.
At the FRM II in Munich an UCN source is under construction, where at one beam position the nEDM will be measured. A schematic illustration is shown in Fig. 1.7. The source is placed close to the fuel element. The neutrons will be extracted on the right side. From the left side the supply lines for Helium and the pre moderator gas are inserted. It is planned to reach UCN densities of several 1000 UCN/cm^3 [44].
A more detailed description of UCN sources based on deuterium can be found in [45], [42], [46] and [44].

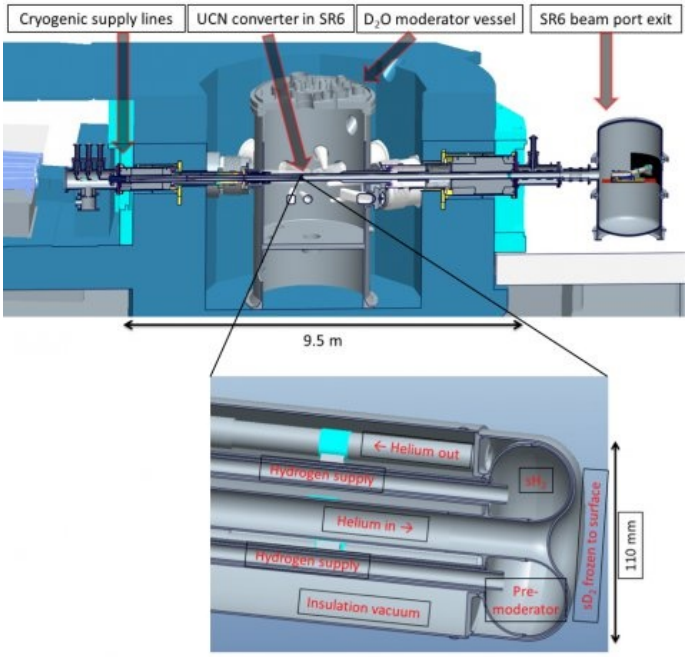

Figure 1.7: Schematic drawing of the future UCN source at the FRMII. Taken from the UCN source homepage [47].

1.3 Neutron Technology

In this section the theoretical basics for building the neutron optical components within this thesis are discussed. First topic will be the the neutron transport in section 1.3.1 followed by the storage of UCN in section 1.3.2. Then in section 1.3.3 a short introduction into the field of surface coating by using magnetron sputtering will be given. The last section 1.3.4 in this chapter will deal with the spin manipulation of UCN.

1.3.1 Neutron Optics

The first experiments for guiding neutrons or neutron beams with tubes out of the reactor environment were done in 1963 by Maier-Leibnitz and Springer. Since this pioneering days in using neutron guides the transport efficiency benefited by different innovations like rectangular glass guides for thermal or cold neutrons covered with super mirror coatings, consisting of different materials like nickel and titanium or iron and silicon depending on its application.
The theoretical background is given in the following, but more detailed elaboration on this topic can be found in [21] and [22]. For the next generation nEDM measurement a transport system with a high UCN transmission will be essential.
Neutron optic can be described in the first place with well known relations of light optic physics. The neutron refraction index n for the change of the wave vector in different materials can be compared with the index of refraction for light propagation from one medium into another and is defined as:

$$n = \frac{k_{material}}{k_{vacuum}} \tag{1.31}$$

and is linked to the neutron optical potential and the energy of the neutron in the following way:

$$n = \sqrt{1 - \frac{V_F}{E_n}} \tag{1.32}$$

For most materials $V_F > 0$ and according to this $n < 1$. If $E_n < V_F$ n becomes imaginary the neutron will be totally reflected from the surface. Since the neutron is a quantum mechanical particle this part is closely linked to the strong interaction background given in section 1.2.1.

Transmission and Reflection of UCN in a Cylindrical Guide System

In the last decades different theories for describing the transmission through a neutron guide system were developed. [21] and especially [22] give a well insight to these theories.
In the latter the transmission of an UCN guide is defined as the ratio between the neutron flux measured in front of a guide and the flux behind this guide [22]:

$$T = \frac{N_{sample}}{N_{ref}} \tag{1.33}$$

with N_{sample} being the count rate after the guide segment that had to be investigated and N_{ref} the reference before.

The transmission of a guide is predominated by different effects. It is obvious that the transmission decreases with the length of the guide system (Fig. 1.8) and is defined as follows:

$$T = (T_{norm})^{L/1[m]} \tag{1.34}$$

here T_{norm} is the total guide transmission per meter and L is the length of the neutron guide system. Fig. 1.8 shows the theoretical transmission for different T_{norm} values and shows quite plainly the necessity of a high UCN transmission $> 98\,\%$ through a guide system.

Additional to the losses due to up scattering and absorption in a neutron guide

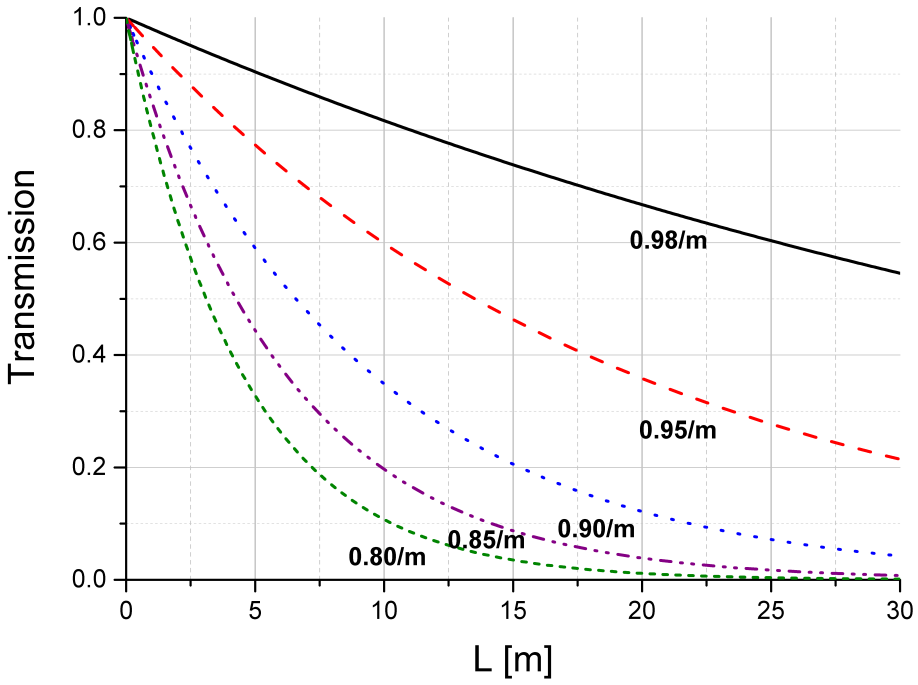

Figure 1.8: With equation 1.34 calculated transmission through a 30 m long guide system for different transmission values per meter.

system, described in section 1.2.1, more loss channels for UCN are possible. Most of them can be ruled out or minimized by optimizing the guide production process. These loss channels and also parameters with an influence on the transmission are listed below:

- **Neutron optical potential**: To reach a high neutron flux at the entrance of the experiment behind the feeding guide system from the UCN source the neutron optical potential V_F of the guide should be as high as possible. It ensures the transport of a maximum energy spectrum and offers the possibility

to manipulate the UCN for any experiment.

- **Surface roughness**: The fraction of specular reflection at the surface of a neutron guide is directly influenced by the surface roughness. The higher the roughness the less the specular reflection. A non specular reflected neutron is lost with a high probability and decreases the UCN transmission through a system.
  To minimize this part of UCNs the surface roughness has to be kept as low as possible. This parameter can be primary regulated by the choice of the guide material and the substrate for the thin layer, coated with a material of a high optical potential. Also substrate cleaning and coating process influence the surface roughness (see section 1.3.3 and section 3.1.2).
- **Gaps**: As detailed in [22] the propagation of UCN can be described like an ideal gas. Gaps can occur in between guides due to misalignment of the guide segments and cause a huge transmission loss channel. But in the guide system are also some volitional gaps or holes for vacuum pumping the guide system. These cause direct losses proportional to their surface area.
  Also non coated parts of the neutron guides (e.g. dust and other pollutions on the substrate). Also the guides should be free from covering dust or pollution because UCNs interacting with these are lost with a high probability.

1.3.2 Ultra-Cold Neutron Storage

UCNs are totally reflected under each angle of incidence (section 1.2.1, which is useful for experiments where neutrons are stored. The storage time τ_{eff} is limited by the lifetime of the neutron itself with $\tau_n = (880.3 \pm 1.1)$s [23].
Additional to this, τ_l decreases the storage time, where τ_l stands for the losses during collisions with the material walls and is determined by the total loss cross section σ as defined in Equation 1.15.
τ_l can also be defined by the geometry of the storage vessel. In a small vessel the UCN will have a stronger wall interaction than in a large vessel, because it is proportional to the loss probability. Slits in the storage chamber build another loss channel. Altogether the effective storage time can be defined as:

$$\frac{1}{\tau_{eff}} = \frac{1}{\tau_n} + \frac{1}{\tau_l} + \frac{1}{\tau_{sl}} \tag{1.35}$$

here τ_{sl} represents the losses caused by slits in the storage vessel. If τ_l and τ_{sl} are much greater than τ_n the effective storage time is dominated by the neutron lifetime

itself. However so far for room temperature experiments the effective storage time is much lower than expected for weakly absorbing wall materials in a trap without slits with theoretical high τ_l and τ_{sl} values. Discrepancies from the theoretical values of up to two orders of magnitude were found [21].
Investigation showed, that these discrepancies are due to up scattered UCNs by contamination on the coated surface. Due to large differences between theory and measurements a neutron absorber contamination on the surface can be neglected because the amount has to be quite large. But most surfaces in principal have a hard to eliminate hydrogen contamination. Since hydrogen is an UCN up scatterer and the amount of compound hydrogen is large enough to maintain the UCN losses this could be the reason for the losses.
This losses can be determined by evaluating a storage curve. More precisely it is the median loss coefficient per wall bounce $\bar{\mu}$ of the storage vessel material and the depolarization probability due to a spin flip in a wall collision (see section 1.3.4).
For measuring a storage curve a couple of storage measurements with different storage times have to be performed. The neutrons are filled into a vessel and stored for a variable time. The remaining neutrons in the trap are guided to a detector, where they are counted after the shutter of the trap is opened again. By plotting this data a dependence of exponential decay is distinguishable:

$$N(t) = N_0 e^{-t/\tau_{eff}} \tag{1.36}$$

with N_0 is the number of accumulated UCNs at t= 0 s in the setup and τ_{eff} is the effective storage time of the neutrons in the storage vessel.
Since the UCN reach the detector in a time period an emptying curve has to be measured for obtaining the number of neutrons in the storage vessel for a single measurement, which also has an radioactive decay dependence. After opening the shutter the neutrons will reach the detector in a characteristic time period τ_{emp}. The total detector count is therefore given by the integral extended to infinity of the emptying curve, which is needed for the storage curve:

$$N_d = N_0 \left(\frac{\tau_{eff}}{(\tau_{eff} + \tau_{emp})} \right) e^{-t/\tau_{eff}} \tag{1.37}$$

Since the loss constant τ_l depends on the neutron angular distribution and the neutron velocity v, the theoretical and the measured storage curve differ from each other. The result is, that the experimental data can not be described by only one exponential decay. In most cases a double exponential decay has to be used.
After a typical short storage time in the vessel the angular distribution can be assumed to be isotropic and τ_l only depends on the neutron velocity v:

$$\tau_l = \bar{l}/\bar{\mu}v \tag{1.38}$$

here $\bar{\mu}$ is the loss coefficient averaged over all angles of incidence and $\bar{l}$ is the mean free path between two wall collisions and is given by the volume of the storage vessel V is and the surface S of its walls:

$$\bar{l} = \frac{4V}{S} \tag{1.39}$$

This relation illustrates that τ_l increases with the dimensions of the storage vessel, but there is an optimum size since the neutrons mass and gravity have to be considered. The limit for τ_l is given by $2v/g$ where g is the acceleration of free fall. Thus gravity decreases the effective storage time with the consequence of a deduced loss coefficient without respecting the gravity.

1.3.3 Surface Coating with Magnetron Sputtering

For most experiments with UCNs a well defined demand on the surface is required. One technique marked out to fulfill all the different claims are, for example the surface roughness, coating quality and material properties. It is the Physical Vapor Deposition (PVD), which is used in this work especially by magnetron sputtering. In this thesis only a short introduction to the wide field of surface coating with PVD can be given. For more details see [48], [49], [50] and [51].
The first metallic thin films were deposed in 1852 by W.R. Grove. Till 1940 this coating technique was inferior to thermal evaporation because of a low deposition rate. In 1940 M.F. Penning refined the PVD method by using magnetic fields resulting in a large deposition rate gain and making the magnetron sputtering to a competitive coating technique.
In general PVD describes all processes working by vaporizing atoms from a target surface by bombarding it with high- energy ions. The ions are created by an electric field applied between the target and a shield. The to the target accelerated ions transfer their energy in an series of elastic and inelastic collisions to the target material. At the target surface some atoms gain enough energy to transfer to overcome the surface binding energy and leave the material (see Fig. 1.9). These ejected atoms build a thin film on a substrate surface. The energy is transferred by momentum transfer and not like in evaporation by thermal excitation. The glow discharge for creating the plasma (ionized gas) is supported by a magnetic field. The ions are accelerated by an electric field to the target and break out material. For creating a plasma the substrate and the magnetron are in a vacuum chamber under a Noble gas atmosphere of 10^{-2} - 10^{-3} mbar (Fig. 1.9).

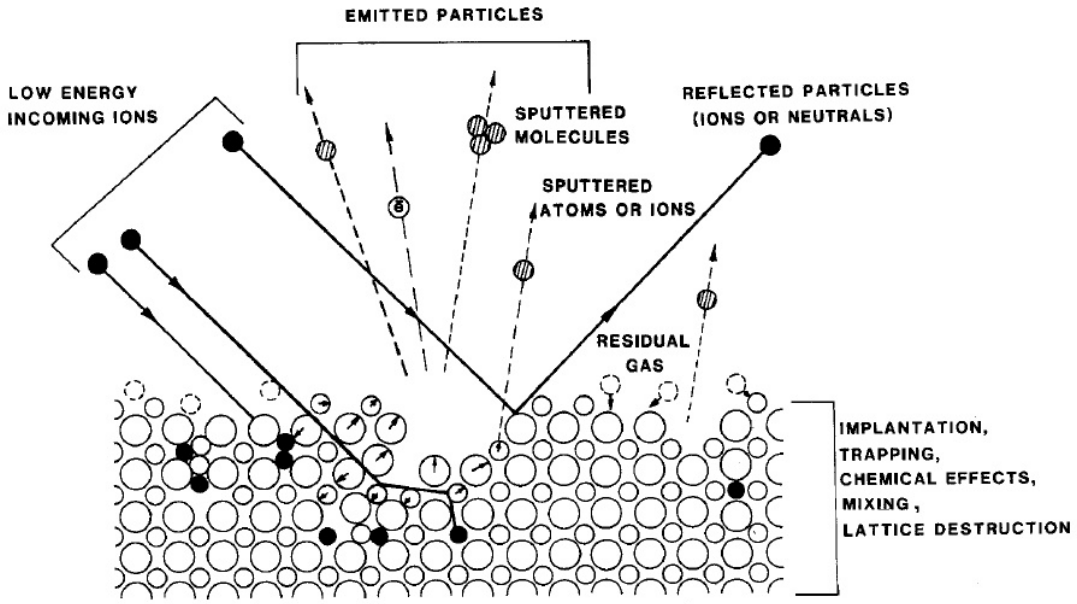

Figure 1.9: Interaction principle between incoming ions and target surface. Taken from [50] Fig. 1

Magnetron Sputtering

The functional principle of magnetron sputtering is dominated by the additional magnetic field. Due to the fact that electric and magnetic field are interfering with each other the plasma is confined directly above the target. This leads to an increment of electrons in front of the cathode (substrate) and increases the ionization rate. With this advantage the process gas pressure can be reduced and therefore the ejected target atoms undergo less collisions on their way to the substrate.
Commonly the processes in a plasma are described by the magnetohydrodynamics but for understanding the functional principle of a magnetron a classical one particle theory can be used instead.
In most cases the magnetic field is produced by an arrangement of several permanent magnets. For non relativistic particles the movement in an electromagnetic field can be described by the Lorentz force:

$$\vec{F} = q\left(\vec{E} + \vec{v}\vec{B}\right) = m\dot{\vec{v}} \tag{1.40}$$

For a homogenous magnetic field a charged particle undergoes a gyration movement around a magnetic field lines because of the $q\vec{v}\vec{B}$ in equation 1.40. Looking on equation 1.40 it is obvious that only the rectangular component of the particle velocity $\vec{v}$ is influenced by the magnetic field where the gyration or Larmor frequency for this

movement is defined by:

$$\omega_L = \frac{|q|B}{m} \tag{1.41}$$

and the Larmor radius is given by:

$$r_L = \frac{|\vec{v}_\perp|}{\omega_L} = \frac{|\vec{v}_\perp|m}{|q|B} \tag{1.42}$$

Here $\vec{v}_\perp$ is the vertical component of the velocity to the magnetic field (Fig. 1.10). Comparing the masses of an electron ($m_e = 0.511\,\mathrm{MeV/c^2}$) and an Ar^+-ion ($m_{Ar^+} =$

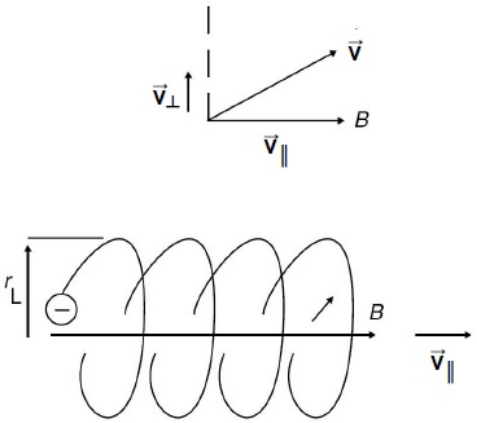

Figure 1.10: Larmor precession of an electron with a velocity $\vec{v}$ in a homogenous magnetic field. Taken from [51] p. 200 Fig. 3.34

$16.8\,\mathrm{GeV/c^2}$) they show a difference of more than four orders of magnitude but the Larmor radius is linked to the particle mass equation 1.42. [1] Therefore an electron fulfills on its way to the anode several gyration movements due to the additional magnetic field and the probability for collision ionization increases. In contrast the Argon ion is not influenced by the magnetic field because of its large mass and can be accelerated unhindered to the cathode.
If a homogenous electric field and a magnetic field is applied at the same time the equation of movements can be split into a term parallel to the magnetic field and orthogonal to it:

$$m\dot{\vec{v}}_\parallel = q\vec{E}_\parallel \tag{1.43}$$

$$m\dot{\vec{v}}_\perp = q\left(\vec{E}_\perp + \vec{v}_\perp\vec{B}\right) \tag{1.44}$$

[1] Typical results for equation 1.42 $r_L = 0.3\,\mathrm{mm}$ where a magnetic field of a magnetron with $0.1\,\mathrm{mT}$ and a kinetic energy of $100\,\mathrm{eV}$ were considered. For argon it is $r_L = 90\,\mathrm{mm}$.

It follows from equation 1.44, that the effective $\vec{E} \times \vec{B}$- drift velocity of charged particles (Fig. 1.11) can be described by

$$\vec{v}_{\vec{E}\times\vec{B}} = \frac{\vec{E} \times \vec{B}}{B^2} \tag{1.45}$$

With this result the direction and value of $\vec{v}_{\vec{E}\times\vec{B}}$ is independent of the charge and mass of the particle. For the case of $\vec{E}$ being perpendicular to $\vec{B}$ Fig. 1.11 shows the

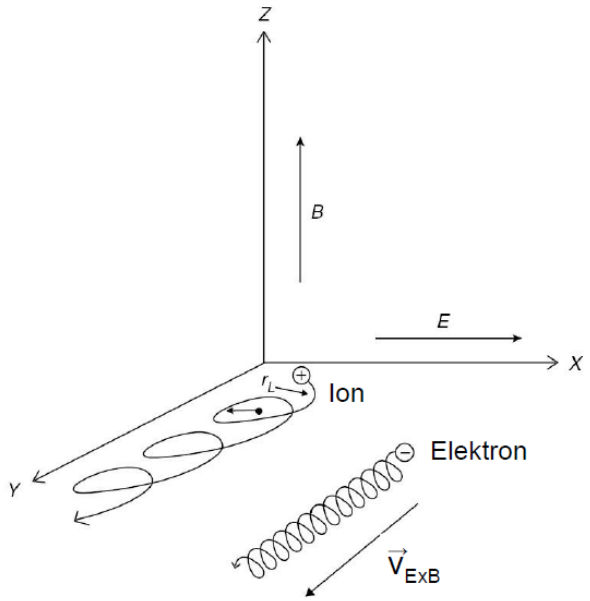

Figure 1.11: $\vec{E} \times \vec{B}$ - drift for rectangular fields. For a movement in electrical field direction positive ions are accelerated. For a movement in opposite direction the particles are decelerated leading to smaller cyclotron radius than for a movement in $\vec{E}$ field direction. The same is valid for electrons but with changed signs. Taken from [51] p. 206 Fig. 3.37

movement of an electron and a positive charged ion. The magnetic field configuration therefore should enable the electrons to move on a circular path because of the $\vec{v}_{\vec{E}\times\vec{B}}$ drift. Otherwise the electrons could leave this zone and get lost for the sputtering process.
Another contribution to the plasma inclusion is the magnetic mirror effect. This effect is based on the adiabatic invariance. A drifting particle in magnetic field direction will be reflected in an inhomogeneous magnetic field at the point of the highest field strength.

Sputtering Yield

Comparing the energy of a particle coated with magnetron sputtering with thermal coating techniques a discrepancy of up to two orders of magnitude is recognizable. In a sputtering process the transferred energy is in the range of 1 till 10 eV. Essentially the evaporation process induced by the argon ions occurs in three channels:

- In the collision between an argon ion and an atom at the target surface the argon ion is reflected and transfers a part of its kinetic energy.
- The ion penetrates the surface and looses all energy by inelastic Coulomb scattering. In this case emission electrons occur.
- The energy transfer occurs in a series of quasi elastic collisions with the target atoms. By collisions of targets atoms among each other the energy for a surface atom can be sufficient that it can leave the material.

The vaporizing process strongly depends on the used process gas in combination with the target material and the energy of the ions colliding with the target surface. To have a measure for each combination of gas and target material the sputter yield is a good instrument and is defined by:

$$S = \frac{N_{vaporized\ atoms}}{N_{ions}} \tag{1.46}$$

For an energy region below 1 keV the sputter yield can be described with the following relation [49]:

$$S(E) = \frac{3}{4\pi^2} \cdot \alpha \left(\frac{M_2}{M_1}\right) \cdot \frac{4M_1M_2}{(M_1+M_2)^2} \frac{E}{\Delta H} \tag{1.47}$$

Here E is the energy, M_1 is the mass of the incoming ion, M_2 the mass of a target atom, ΔH is the heat of sublimation needed to evaporate a target atom. The parameter α is shown in Fig. 1.12.

Layer Growth in Sputtering Processes

For the application of coated surfaces in neutron physics the surface properties are essential. To influence these properties the knowledge of the theory of the layer growth is important.
The evaporated target atoms diffuse trough the argon atmosphere to the substrate and deposes there. In the ideal case the atoms are building successive layers and build a homogenous surface. But the real layer growth occurs in several steps.

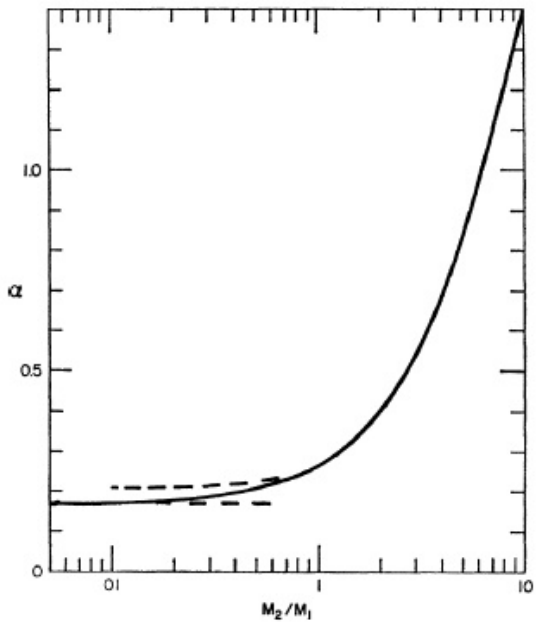

Figure 1.12: Characteristic curve of factor $\alpha\left(\frac{M_2}{M_1}\right)$. Taken from [52] Fig. 13

1. The atoms adsorbed on the substrate are not in a thermodynamical equilibrium with it and move on the substrate surface. In this stage atom clusters or condensation nucleus are formed.
2. These condensation nucleus are unstable its vapor pressure unstable and can evaporate. If the nucleation rate is high enough these clusters reach a critical size and become thermodynamical stable and form so called islands.
3. Till a saturation is reached the amount and size of the condensation nuclei increases. These nuclei can grow in parallel as well as in vertical direction to the substrate surface. In most cases the parallel direction is preferred. The density and mean size of them is strongly influenced by the sputtering parameters and are critical for the structure and properties of the layers.
4. The next step is the merging of some of the islands induced by the process of the minimization of the surface energy. It is also called agglomeration.
5. Last, the island are creating a film, the residual channels and holes are filled with diffusing atoms. By the randomly oriented crystals of the clusters tensions and defects may occur.

Depending on the thermodynamic properties of the substrate and the target material the growing process can be divided in three categories: island growth, layer growth and the Stranski-Krastanov growth which is a mixture of both types. The activation energy for self diffusion correlates quite well with the melting temperature T_m of

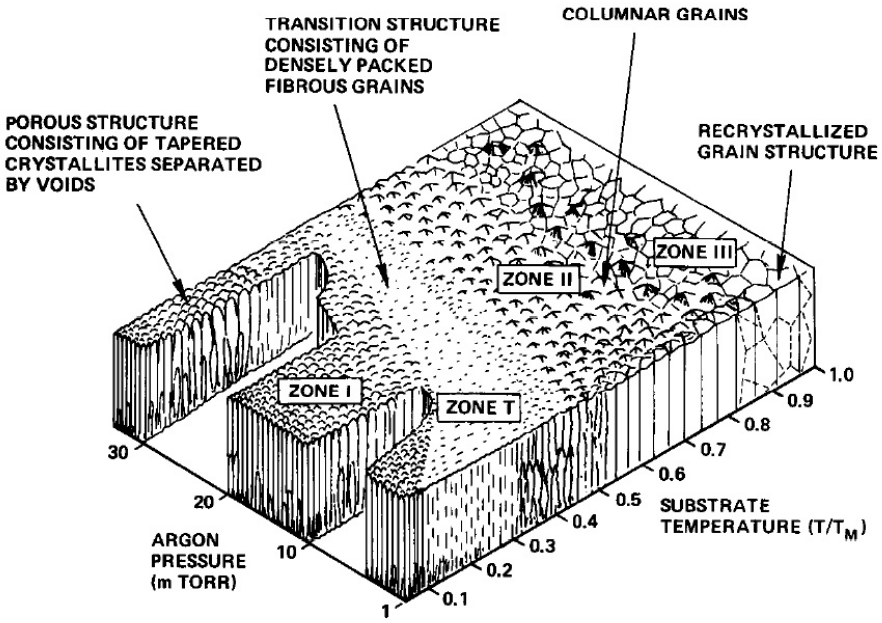

Figure 1.13: Influence of substrate temperature and argon pressure on the structure of a coating. Taken from [53] Fig.1

the coated material. Its influence on the layer growth depends on the substrate temperature T. By virtue of this B.A. Movchan and A.V. Demchishin introduced a model describing the structure of an evaporated film in dependence of T/T_m [53].
For the sputtering process J.A. Thornton adapted this model and added the process pressure [53] and the T zone (Fig. 1.13). With this model the layer growth on amorphous substrates like glass can be described. For a surface coated under the conditions shown in Zone I in Fig. 1.13 a lot of defects will occur because of deficient surface diffusion. Hence the structure of the coating is porous.
In the T zone (Fig. 1.13) the micro structure consists of densely packed fibrous grains. Coatings made with this parameters are characterized by a high density and a low surface roughness, where as for zone II columnar grains are dominating. They occur due to surface diffusion and defects are located at the grain boundaries. In zone III (Fig.1.13) the layer growth is dominated by volume diffusion. Here the grain size grows with higher temperatures.
This model shows that it is recommendable to use the parameters mentioned for zone T to obtain surface coatings with the appropriate properties for UCN guide and storage vessel coatings. It is also helpful to use substrates with a low initial surface roughness.

1.3.4 Spin Manipulation of UCN

The neutron participates at the magnetic interaction (section 1.2.1), which is utilized in experiments like nEDMs or lifetime experiments. Therefore neutrons can be polarized, which in turn can be analyzed with different methods (see section 1.3.4 Polarizing Ultra cold neutrons). Another possibility is to flip the spin of a neutron using a radio frequency (see section 1.3.4 Spin Manipulation with Spin Flippers). A comprehensive description on this topic is also given in [22] or in [54].

Polarizing Ultra-Cold Neutrons

The spin orientation of a neutron in the free space is randomly oriented. The spin direction is always defined pertaining to the external magnetic field. Since the neutron is a fermion with spin 1/2 it has two possible spin orientations, $N_\uparrow$ and $N_\downarrow$. Hence, it follows that an non polarized neutron beam consists of half neutrons with a spin up and the other half with spin down. The polarization is given by:

$$P = \frac{N_\uparrow - N_\downarrow}{N_\uparrow + N_\downarrow} \tag{1.48}$$

where for $P = 0$ follows for an unpolarized neutron beam and for a 100% polarized beam $P = 1$. To reach high polarization a magnet with a high magnetic field can be used where one spin component is reflected as already described in section 1.2.1. This method is comparatively easy to apply for UCN because the kinetic energy of the neutrons is of the same order of magnitude as the magnetic energy. But in most cases the polarizing magnet has to be superconducting to cover the complete required spectrum for an experiment. However, this option has also non negligible disadvantages like the investment and operation costs, required space and most important stray fields disturbing neighboring neutron instrumentation.
Another option is to benefit from the spin dependence of reflection or scattering from a surface. A thin iron foil can be installed into the beam line and is magnetized to saturation by some permanent magnets. Because of the spin dependence of the scattering on a nucleus in a magnetized foil the potential for an UCN is a combination of the optical potential V_{Fe} of the iron foil and the magnetic potential V_{mag}.
The magnetic potential V_{mag} is given by the magnetic scattering length a_{mag} and the resulting potential is defined as:

$$V_F = V_{Fe} + V_{mag} = \frac{2\pi\hbar}{m} N \left(a \pm a_{mag}\right). \tag{1.49}$$

Thus a neutron with an anti-parallel spin orientation compared to the magnetic field of the ion foil ($N_{\uparrow\downarrow}$) sees a lower potential than a neutron with a parallel spin orientation ($N_{\uparrow\uparrow}$). In principle such a polarizing foil can be used in transmission or reflection mode. Using it in transmission mode, UCNs with velocities less than 3.7 m/s are reflected regardless of the polarization, which is also illustrated in Fig. 1.14. Up to a velocity of 8.2 m/s the $N_{\uparrow\downarrow}$ component is transmitted and the $N_{\uparrow\uparrow}$ component is reflected. Faster neutrons are penetrating the foil unobstructed.

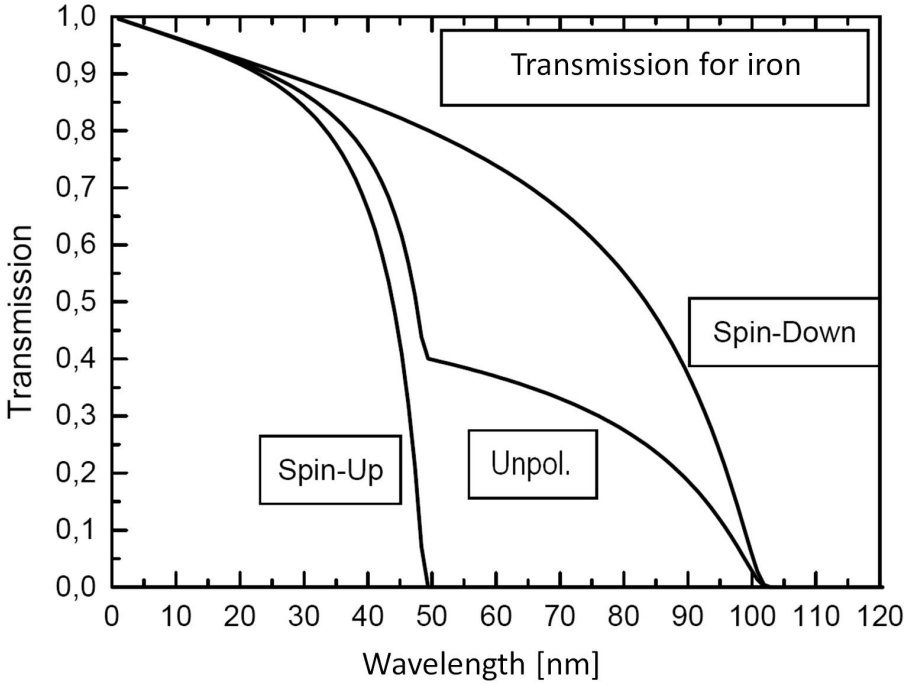

Figure 1.14: Theoretical transmission through a 1 μm thick iron foil. Taken from [55] p.31 Fig. 2.12

The theory of polarization and analysis of polarization can be described with the formalism of the two-dimensional vector [54]. This formalism describes the effect of the polarization, polarizing foils and spin flippers on a neutron beam. Starting with a two dimensional vector:

$$\Psi = \begin{pmatrix} a \\ b \end{pmatrix} \qquad \Psi_0 = \begin{pmatrix} 1 \\ 1 \end{pmatrix} \tag{1.50}$$

where a stands for the number of neutrons polarized along a chosen axis and b represents the number of neutrons polarized in the opposite direction. For an unpolarized

neutron beam Ψ_0 the parameters are $a = 1$ and $b = 1$.
A polarized beam of polarization P (in general $|P| < 1$) can be written as

$$\Psi = \frac{I}{2}\left(1 + P\sigma_z\right)\Psi_0 \tag{1.51}$$

here σ_z is the Pauli matrix in z direction and I is the total intensity of a polarized beam and is defined in dependence of Ψ_0:

$$I = \frac{\Psi_0\left(1 + P\sigma_z\right)\Psi_0}{2} \tag{1.52}$$

With both relations it follows that the beam is totally polarized along the chosen axis if $P = 1$ or $b = 0$ and for a total polarization along the axis in the opposite direction $P = -1$ or $a = 0$. In general $|P| < 1$.
Through the transmission matrix

$$T_P = t\left(1 + P\sigma_z\right) \tag{1.53}$$

the polarization of a non polarized neutron beam with an intensity of $2I$ can be characterized. Here, t is a constant factor determining the attenuation of the beam. This means for a perfect polarizer ($P = 1$) and without absorption while the neutrons pass the foil, only half of the intensity of the beam is left because only one spin component is transmitted. The transmission can be done in the same way through an analyzer foil.
If an spin flipper is installed into the beam line the formal treatment can be described with the following operator:

$$Q = 1 - f + f\sigma_x \tag{1.54}$$

where f is a parameter describing the efficiency of the spin flipper and σ_x is the Pauli matrix in x direction. More details on the functionality of spin flippers will be provided in the next part. If a neutron beam is polarized with a polarization P a spin flipper changes it in the following way by combining equation 1.53 and 1.54:

$$\Psi = \left(1 - f + f\sigma_x\right)\left(1 + P\sigma_z\right)\Psi_0 = \left[1 + P\left(1 - 2f\right)\sigma_z\right]\Psi_0 \tag{1.55}$$

here $\sigma_x\sigma_z = -\sigma_z\sigma_x$ is used. A spin flipper with $f = 1$ rotates the spin in dependence to the spin orientation by 180°. In this formalism a value $f = 1/2$ does not lead to a 90° rotation but to a total depolarization of the beam.
For a complete polarization setup two polarizers are necessary, one for polarizing the beam and one to analyze it after a certain time. The transmission through it can be described by the following relation by combining equation 1.53 and 1.54:

$$\begin{aligned}\Psi &= t_A t_P I\,(1+P_A\sigma_z)\,(1-f+f\sigma_x)\,(1+P_P\sigma_z)\,\Psi_0 \\ &= t_A t_P I\,(1+P_A\sigma_z)\,[1+P_P\sigma_z\,(1-2f)]\,\Psi_0 \\ &= t_A t_P I\,\{1+P_A P_P\,(1-2f)+[P_A+P_P\,(1-2f)\,\sigma_z]\}\,\Psi_0\end{aligned} \tag{1.56}$$

where P_P is the polarizing power of the polarizer with an attenuation of t_P, f is the spin flip probability and P_A is the analyzing power with its attenuation t_A of the neutron beam. Hence the intensity measured with the detector is

$$I_D = t_A t_P I\,[1+P_A P_P\,(1-2f)] \tag{1.57}$$

With two measurements with spin flipper on and off, the product $P_P P_A$ can be diagnosed in dependence of the spin flip efficiency. So it is essential to know it quite well.
To determine the spin flip efficiency a second spin flipper has to be used in the beam line. Where the intensity measured by a detector after passing a polarizer, two spin flippers and an analyzer is given by

$$I_D = t_A t_P I\,[1+P_A P_P\,(1-2f_1)\,(1-2f_2)]\,. \tag{1.58}$$

To characterize the spin flippers and the polarizers a measurement need to be made, where one spin flipper is on and the other one is off and a measurement with both on and both off, respectively.

Spin Manipulation with Spin Flippers

To investigate the polarization of an arrangement of polarizers, spin flippers can be used. The inversion of the spin by a spin flipper depends on an external magnetic field, which is achieved by adiabatic or resonant spin flippers.
In the case of a resonant spin flipper a static and homogenous magnetic field is superposed with a high frequency magnetic field. The spin flip efficiency depends on the interaction time of the neutrons with a high frequency field, meaning it depends on the neutron velocity. This type is flipping only a small wavelength range and therefore it is mainly suitable for monochromatic neutron beams. Since UCNs extend over a wide wavelength range this method is not adequate.
For an application in the UCN energy region adiabatic spin flippers are more appropriate. Here also a static magnetic field B_0 is superposed with a high frequency magnetic field $B_1(t)$ but different to the resonant spin flipper the static magnetic field has a gradient. Therefore adiabatic spin flippers cover a broad wavelength band

and can flip, if they are well tuned a wide spectrum of UCNs.
The static magnetic field with a gradient B_0 is vertically oriented to the neutron beam, while $B_1(t)$ is parallel to the propagation direction of the neutrons. In presence of an external magnetic field B_0 the neutron magnetic moment torques around B_0 with the Larmor frequency $\omega_L = \gamma B_0$. γ is the gyromagnetic ratio and is defined by $\frac{\gamma}{2\pi} = 29.17\,\mathrm{kHz/mT}$.
For the following contemplation the frame of reference is rotating with the high-frequency ω. The effective field seen by a neutron is given by [56]:

$$B_{eff} = \sqrt{(B_0 - B_\omega)^2 + B_1^2} \tag{1.59}$$

where $B_\omega = \frac{\omega}{\gamma}$. For a neutron passing an adiabatic spin flipper the magnetic field $(B_0 - B_\omega)$ is stronger than $B_1(t)$ and the effective field is perpendicular to the neutron direction of movement. However, the magnetic field changes on the way through the spin flipper until the point where $B_0 = B_\omega$ and the field is given by $B_1(t)$. On its further way the B_0 field decreases and $(B_0 - B_\omega)$ becomes negative. Following this the effective field B_{eff} is rotated by 180°. If a neutron follows this field modifications, it it has to be adiabatic. The velocity range and the field gradient of B_0 have to be adapted to each other, that the neutron magnetic moment can follow the change. This is the case, if the time dependence of the field is much smaller than the Larmor frequency ω_L:

$$\frac{1}{\left|\vec{B_0}\right|} \cdot \left|\frac{d\vec{B_0}}{dt}\right| \ll \frac{\vec{\mu} \cdot \vec{B_0}}{\hbar} = \omega_L \tag{1.60}$$

For the case of UCNs, this adiabatic condition is easy to achieve because of their comparatively low velocity. More details on the theory of spin flippers see [57], [58] and [59]. Technical details on constructing different spin flippers are described in [22], [56], [60] or [61].

Depolarization

Like losses due to absorption and up scattering by wall collision in section 1.3.2 UCN losses by depolarization at the vessel surface in presence of a magnetic field are also of prime interest for nEDM measurements. The depolarization would decrease the visibility between the two spin components. To minimize these losses non magnetic materials with a low depolarization are necessary. Magnetic domains in the wall material with dimensions of the neutrons wavelength or larger lead to a dominating effect by wall neutron interaction by the magnetic moment and remain inevitable with depolarization [62].

The magnitude of this depolarization process is described in [62] as a collision of an UCN with the storage vessel wall, where the two spin orientations of the neutron experience different neutron optical potentials resulting in ΔV_F. Here the interaction term with a magnetic field 1.8 has to be supplemented to the neutron optical potential. For an interaction time τ the spin of the neutron will be rotated by an angle of:

$$\delta\phi \approx \frac{\tau \Delta V_F}{\hbar} \tag{1.61}$$

For a neutron penetrating a distance of $\lambda/2\pi$ the interaction time τ is given as:

$$\tau = \frac{\lambda}{1\pi\nu} \approx 2 \times 10^{-9}\text{s}. \tag{1.62}$$

For a certain storage time the UCN makes $M = T_s\nu/l$ collisions. For each collision the UCN does a random phase shift and will end in:

$$\Delta\phi \approx \overline{\delta\phi}\sqrt{M} = \frac{\overline{\Delta V_F}\lambda}{h}\sqrt{\frac{T_s}{l\nu}} \tag{1.63}$$

For a material with a randomly orientated nuclei interacting with the neutrons the averaged potential difference is $\overline{\Delta V_F} = \Delta V_F/\sqrt{N}$.
To find out which materials are suitable different experiments were performed in [63] or [64] to determine their depolarization. Here, UCNs are stored horizontally in a cylindrical material bottle. At the bottom the UCNs were reflected by a dipole magnet and on top by gravity. Hence, UCNs with a wrong spin orientation and with a too high kinetic energy are cleaned out over a certain time. After this cleaning process the stored neutrons are polarized. Now the neutrons can be stored for different time periods and a decay curve can be plotted as already described in section 1.3.2.
Considering also the different causes of losses due to wall collisions τ_l for the effective storage time τ_{eff}, as it is defined in equation (1.35), the effective storage time can be written as follows:

$$\frac{1}{\tau_{eff}} = \frac{1}{\tau_n} + \frac{1}{\tau_\beta} + \frac{1}{\tau_\mu} + \frac{1}{\tau_{sl}} \tag{1.64}$$

The losses due to absorption represented by τ_μ can be written as $\tau_\mu = \frac{1}{\mu \cot \nu}$, where ν is the wall collision frequency, and the losses due to depolarization $\tau_\beta = \frac{1}{\beta \cdot \nu}$, where β is the depolarization probability. With the number of spin flipped neutrons N_{sp} and the total number of stored UCNs at the beginning of the measurement $N_1(t_0)$ the depolarization probability can be calculated assuming, that a single neutron energy and the gravity is neglected for the reflection process. Therefore the number of spin flipped neutrons is given by:

$$\frac{dN_sp}{dt} = N(t) \cdot \nu \cdot \beta \tag{1.65}$$

by integrating equation 1.65, β can be calculated:

$$\beta = \frac{N_{sp}}{\tau_{eff} \cdot \nu \cdot N_1(t_0)} \tag{1.66}$$

With this method it is possible to determine the depolarization β of the used wall material in a nEDM storage chamber.

Visibility and Longitudinal Spin Polarization Lifetime

The visibility α for a nEDM measurement run is directly influenced by the polarization of the neutrons filled in the storage chamber. To reach a high visibility in a nEDM measurement it is important to conserve the polarization all the way through the setup from the polarizer to the analyzer. Meaning, the visibility is a direct measure for depolarization in the setup and influences the statistical sensitivity of the nEDM. The visibility is defined by:

$$\alpha = \frac{N_A - N_B}{N_A + N_B} \tag{1.67}$$

where N_A and N_B are the count rate for the different spin components in the detector. Also the longitudinal spin polarization lifetime T_1 in the precession chamber influences the statistical sensitivity of a nEDM measurement. A high depolarization during storage leads to a low T_1 time and decreases the visibility. And also limits the free precession time T in the chamber for a nEDM measurement. T_1 decreases exponentially for large storage times and is linked to the visibility by the following relation [65]:

$$\alpha(T) = \frac{P_0 e^{-T/T_1}}{1 + \frac{p_{fast}}{1-p_{fast}} e^{T(1/\tau_{fast} - 1/\tau_{slow})}} \tag{1.68}$$

With P_0 is the initial polarization of the UCNs, p_{fast} is the ratio of fast UCNs and τ_{fast} and τ_{slow} are the effective lifetimes for the different UCN velocities.

Chapter 2

The Munich nEDM Project

The predominant part of this work is allocated in the next generation Munich nEDM project.Therefore this chapter will pay attention to the complete apparatus which is under construction at the FRMII, located at the Technische Universität München in Garching. The first section 1.1.2 will give a brief overview of the recent nEDM measurements followed by the description of the Munich nEDM apparatus with its magnetometer systems, the high voltage system and the data acquisition and analysis. Additionally neutron guiding, storing and spin manipulation system will be treated in detail in sections 3 to 6.

2.1 Concept and Experimental Technique

In the current experiments of nEDMs a static magnetic and an electric field is applied to stored UCNs. The Hamiltonian for this interaction of a neutron spin $\vec{s}$ with this magnetic $\vec{B}$ and electric fields $\vec{E}$ is given by [12]:

$$H = -\vec{\mu_n}\vec{B} - \vec{d_n}\vec{E} \tag{2.1}$$

where d_n is the EDM and is aligned to the spin of the neutron, μ_n is the magnetic moment and $s = 1/2$ is the net angular momentum of the neutron.

For measuring the nEDM the Larmor frequencies ν in a static magnetic field of two measurements are compared with each other. One Larmor frequency measurement is performed with parallel B and E field (B_p,E_p and ν_p) and one with both fields anti-parallel (B_a,E_a and ν_a). If an EDM exists a difference between the Larmor frequency can be diagnosed and is defined by:

$$d_n = \frac{-h\left(\nu_p - \nu_a\right) - 2\mu_n\left(B_p - B_a\right)}{2\left(E_p + E_a\right)} \tag{2.2}$$

By nature of the strength of the magnetic interaction in a nEDM measurement a low magnetic field is applied to the stored neutrons. And due to the small value of

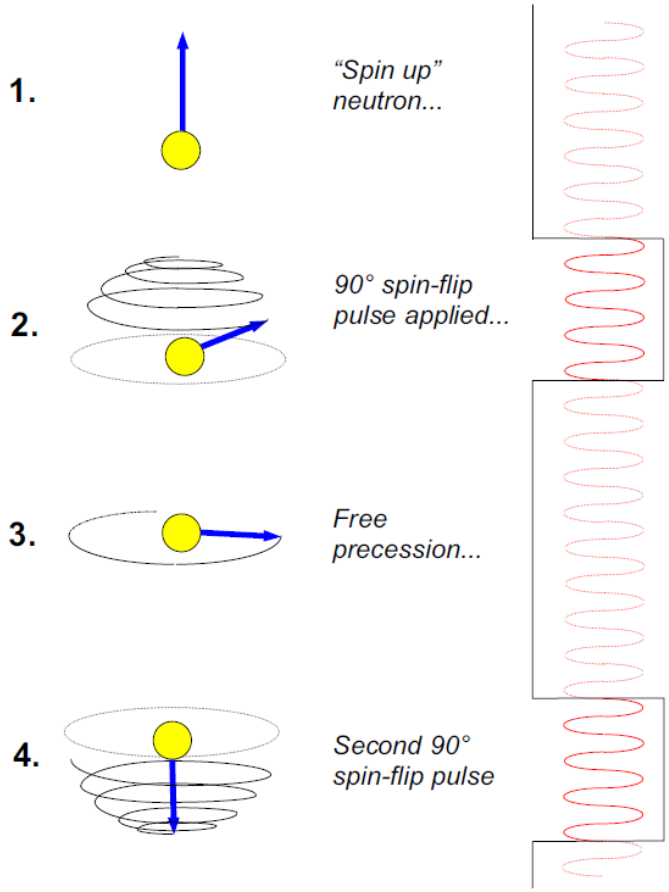

Figure 2.1: Schematic illustrating of the Ramsey method of separated oscillatory fields. Taken from [62] Fig. 2

the expected EDM d_n a high electric field is utilized. For an optimal measurement the B field well known and is the same for both performed measurements, only the E field is changing its sign, hence d_n is defined by:

$$d_n = \frac{-h\,(\nu_p - \nu_a)}{4E} \tag{2.3}$$

The current limit for nEDMs is so small that the requirements on the measurement techniques of all required parameters gets continuously challenging. First measurements where performed with neutron beams like in [66] but this method is only suitable down to regions of 10^{-24}e·cm (see Fig.1.1).

The main issue in nEDM measurements with stored UCNs is to determine the neutron Larmor frequency as exact as possible. Therefore polarized UCN are stored for a certain time period in a precession chamber in a preferably well defined magnetic and electric field environment. During this storage Ramsey's method of separated oscillating fields [67] is applied to the neutrons as done by [68], [69] shown in detail

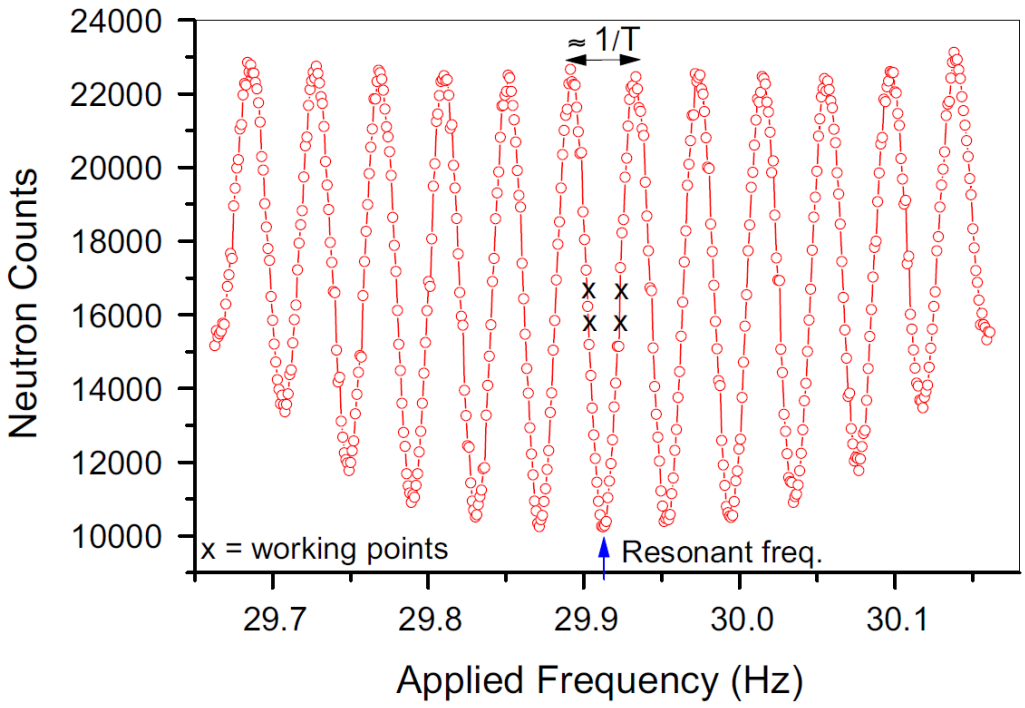

Figure 2.2: Typical Ramsey resonance pattern. Black crosses mark the working points during a normal data taking run. Taken from [62] Fig. 3

in Fig. 2.1. At the beginning of each measurement cycle the polarized UCNs are initially aligned along the B_0 field (Fig. 2.1 1.). With the first radio frequency (RF) pulse (Fig. 2.1 2.) of a certain time t_{RF} with a frequency equal to the Larmor frequency of the neutrons in the magnetic field $\omega_n = \gamma_n B_0$ the neutron spin is flipped by 90° into the plane orthogonal to the static magnetic field. Now the neutrons are precessing free in the storage chamber for a time $T \gg t_{RF}$ (Fig. 2.1 3.) with their Larmor frequency. After the free precession time T a second RF pulse is applied with the same frequency (Fig. 2.1 4.). By comparing the frequencies of the neutrons and the clock running with the exact applied frequency in the background during the free precession time, a frequency phase shift caused by a non zero EDM $d_n \neq 0$ becomes visible. The neutron Larmor frequency for an experimental configuration is determined by a slightly detuned RF pulse and counting the spin up and spin down UCNs for each measurement . The result of such measurements are the Ramsey fringes, as shown in Fig. 2.2. For a data recording run in a nEDM measurement, only the Ramsey central fringe is measured at four working points, marked in Fig. 2.2. These points are chosen because the slope is the steepest here and because of this the sensitivity on Larmor frequency changes is high.

The biggest challenge during this measurement method is to know the exactly magnetic field and its gradient over the storage time and the storage chamber. To tackle this problem and to achieve more precise results than in former nEDM measurements ^{199}Hg Co magnetometer where successfully implemented [70], [71]. Another significant improvement was the concept of a double chamber, introduced by the Gatchina EDM group [72], [73] and [74]. Here, the experiment is performed in two UCN precession chambers in the same B_0 field and simultaneously, in one chamber the electric field is parallel and in the second it is anti parallel. With this arrangement first order magnetic effects could be excluded. Another improvement also introduced by the Gatchina group is the simultaneous spin detection. In the RAL-Sussex-ILL experiment both spin components are detected after another, here the emptying arm is split into a detection part for parallel spin neutrons and one for anti parallel. This technique was used in this thesis and is further discussed in detail in section 5.6.
All of these former experiments are mainly limited by statistical sensitivity, because the current available UCN densities on Earth are in the order of a few UCN/cm^3 (see section 1.2.2). The statistical sensitivity of the EDM experiment σ_d is given by [12]:

$$\sigma_d = \frac{\hbar}{2\alpha ET\sqrt{N}\sqrt{M}} \tag{2.4}$$

where N is the number of neutrons counted at the end of a Ramsey cycle, M is the number of repetitions of the measurement, T the spin precession time of each Ramsey experiment, E the electric field and α is a quality parameter. T can be maximized by using materials with a high effective neutron lifetime in the precession chamber τ_{eff} and a high polarization lifetime T_1. This is corresponding to a low depolarization per wall collision for the UCNs in the precession chamber and through the guide system from the chamber to the spin analyzer.
Also systematic effects occur in nEDM measurements. These are mainly generated by magnetic field changes, electric field effects and the velocity distribution of the UCN during the measurement. The leakage currents [13] appearing by applying high voltage in combination with a magnetic field aligned in the same direction, is one of these effects to be controlled [12]. This currents were measured with a resolution of $> 10\,\mathrm{pA}$ in former experiments [62] and therefore this effect can be monitored and is no obstacle for further experiments.
Another systematic effect, which is becoming more important the lower the upper limit of nEDM measurements is pushed, is the so called geometric phase effect, described in detail in [75]. It is a false-effect. The origin is in the simultaneous presence of magnetic field gradients and the magnetic field of a particle moving with a velocity v in an electric field E. This effect is similar to the Bloch-Siegert shift

and a shift of the Larmor-frequency $\Delta\nu$ appears proportional to the square of a transverse magnetic field. This results in interference terms, if the transverse field has two or more sources. For an EDM measurement the interference term is linear in E and results a false-effect that has to be considered during the measurement. In first order approach for a linear gradient the dominating not canceling term for the frequency shift is given by:

$$\Delta\nu \sim \frac{\delta B_z}{\delta z}\frac{r}{2}\left(E \times v\right) \tag{2.5}$$

Probing this effect is challenging and for a next generation measurement indispensable.

2.2 The Munich nEDM Apparatus

The nEDM experiment is still under construction in the neutron guide hall east (see Fig. 2.5) and will be supplied with UCN produced $\approx 27\,\mathrm{m}$ away with a D_2 based UCN source (see section 1.2.2) located beside the reactor core at the FRM II. Detailed investigations concerning the transport of the UCN over long distances like the $\approx 27\,\mathrm{m}$ will be carried out in section 3. In [76] a polarized UCN density of $> 3000\,1/cm^3$ in the storage chamber is projected.
Fig. 2.3 shows the arrangement within the centerpiece of the nEDM experiment. All the components inside the vessel (Fig. 2.3(5)) are in high vacuum and all installed components have to be non magnetic. The UCNs will enter the two neutron storage (Fig. 2.3(1)) chambers from the left side through separated UCN guides (Fig. 2.3(6)). Each of the two UCN chambers (Fig. 2.3(1)) are made of a 12 cm high Quartz cylinder with an inner diameter of 48 cm and an wall thickness of 1 cm. The high voltage (HV) electrode (Fig. 2.3(3)) proceeds as the bottom cap for the upper chamber and the top of the lower chamber. The ground electrodes (Fig. 2.3(4)) are limiting the chambers at the top and bottom. Between the HV electrode and the ground electrode an electric field of $200\,kV$ can be applied on the UCN. In between two measurements the polarity of the electric field can be reversed with the used high voltage supply. The double chamber arrangement has the advantage of a simultaneous measurement of ν_a and ν_p if the homogenous magnetic field B_0 is also applied.

In the two ground electrodes is also the access points for the neutrons to the storage chamber. The filling is realized with a plug shutter system. A detailed description of this shutter system can be found in section 6. The vacuum chamber provides also the possibility of online access (Fig. 2.3(7)) for different kinds of magnetometers, like

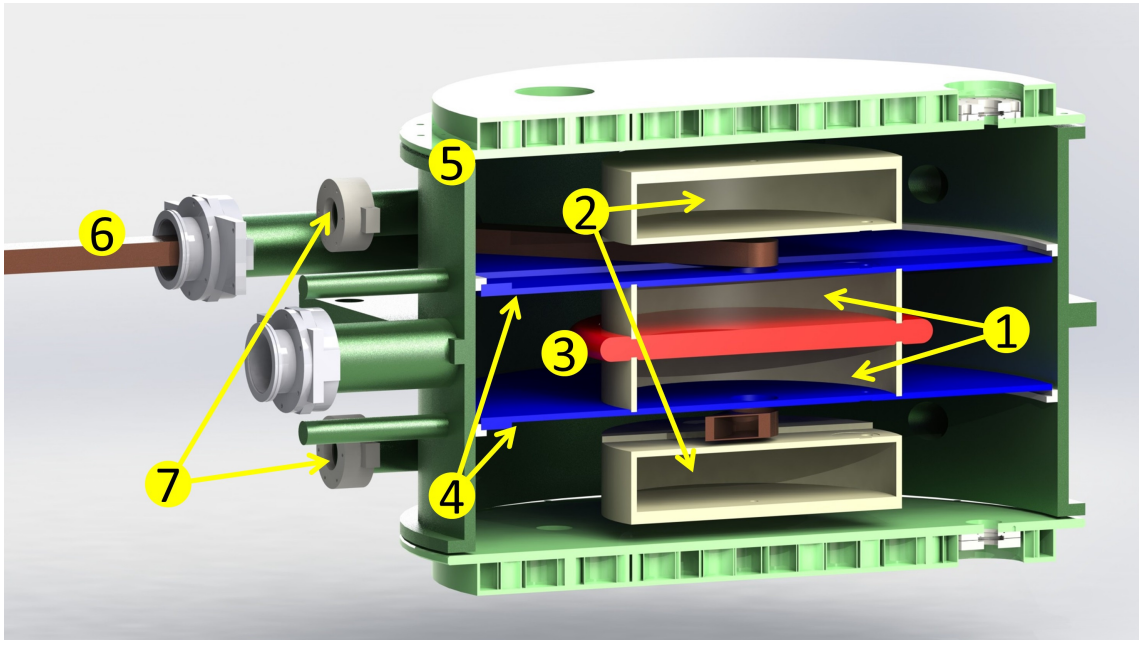

Figure 2.3: Inner arrangement of the centerpiece of the Munich nEDM apparatus. Between the two UCN storage chambers (1) is the high voltage (HV) electrode (3). In the space between the HV electrode and the two ground electrodes (4) an electric fields up to 200 kV can be applied in the UCN storage chamber. On the top and bottom of the storage chamber are two spectrometer chambers for a ^{199}Hg co- magnetometer (2) to measure the magnetic field gradient. All these components are installed in a non magnetic vacuum chamber (5). From the left side various access channels are attached. Some are for the UCN feading guides (6) to access the storage chamber, others are for possible additional magnetometers to map the fields online (7). Taken from [77] Fig. 1.1

Superconducting quantum interference devices (SQUID), for mapping the magnetic field during a measurement cycle. Above and below the two storage chambers are two additional cells filled with ^{199}Hg acting as an atomic magnetometer (Fig. 2.3(2)). There is also the possibility to add ^{199}Hg as a co-magnetometer in the UCN chamber through a valve system between the two chambers.

2.3 Electric Field

For a next generation nEDM also the electric field stability and the controlling of it has high importance. An instable electric field would cause systematic effects like

geometric phase effect, described in section 2.1. Fig. 2.3 shows also arrangement of the electric field concept, where the HV electrode (Fig. 2.3 (3)) in the middle of the vacuum chamber is separated by an insulator ring from the ground electrodes (Fig. 2.3 (4)). In between these two electrodes an electric field up to 200 kV should be applied.
In [78] different solution ways to meet all requirements are investigated. Different materials were tested on its capability as HV electrode. A requirement on the material is that effects, like Johnson's noise, thermal currents and radio frequency noise are suppressed. According to this the electrode material has to be chosen and well tested before implementing it in the final nEDM setup. The author in [78] described tests and the HV parts especially for the Munich nEDM project.

2.4 Magnetic Shielding and Magnetic Field Measurements

To achieve the planned upper limit for the nEDM of 10^{-28}e·cm one of the key issues is to control magnetic fields during the measurements. Therefore, the precise knowledge of the magnetic fields is indispensable, but also the shielding of external fields is crucial. In order to do this a complex system consisting of various sensors and shielding materials has been created. Here only a short summary on this important part of the nEDM project is given. A more detailed elaboration is given in the studies presented in [77], [79], [80] and [81].

2.4.1 Magnetic Shielding

To create a stable and clean magnetic environment a sophisticated combination of different compensation and shielding systems, shown in Fig. 2.4, is arranged.
The first step to reach this magnetically stable and clean area for the nEDM measurement is to suppress the influence of metallic and magnetizable components in the concrete surrounding the experimental place. The experiment position is 9 m long, 6 m wide and 1 m deep. To satisfy this claims the hall floor at the experimental position was removed and replaced with non- metallic and non- magnetizable concrete (Fig. 2.4(1)). By doing this step also an electrical and vibrational decoupling from the experimental hall was achieved.
To compensate variable magnetic fields an active compensation system (ACS) was build up around the experiment (Fig. 2.4(1)). The systems is mounted on an alu-

minum support structure with the dimensions: 9 m long, 6 m wide and 6 m high. On this structure 24 remotely controllable coils (Fig. 2.4 shown in red) and 60 3-axis fluxgates of the type Mag-690 [82] are fixed.

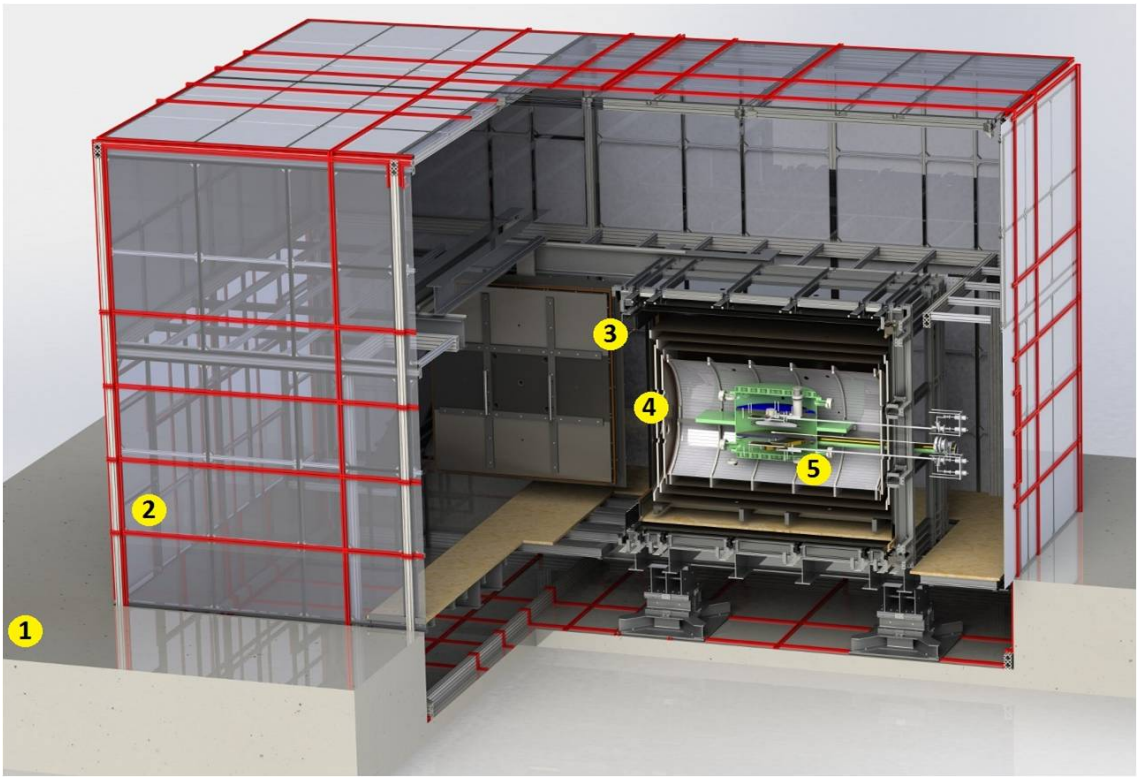

Figure 2.4: Technical illustration of the magnetic shield at the beam position in the neutron guide hall east. The complete nEDM setup is placed in a hole made from nonmagnetic concrete (1). The active compensation system (2) made of a dedicated coil system, which is mounted on a non magnetic aluminum support structure and the outer passive shielding (3) is arranged around the inner (4) shielding. Inside the passive magnetic shields is the nEDM spectrometer chamber (5) with all the other supporting systems (see. Fig. 2.3). Taken from [77] Fig. 1.2

With the fluxgate signals it is possible to calculate the optimal coil current and to compensate the external magnetic perturbations [77]. The aluminum structure is covered with transparent and opaque PVC panels to build a closed room for the experimental side. The opaque pannels are situated in the way that sunlight can not heat up parts of the setup and in this way causes temperature gradient-induced currents, generating magnetic fields. Another advantage is a preferably clean environment and the possibility to stabilize the temperature and humidity inside with an air conditioning system in the mK region. An illustration of the experiment

place in the neutron guide hall east is shown in Fig. 2.5. There the aluminum structure covered with PVC panels with the ACS system on the outside is shown.

Figure 2.5: Picture of the magnetic shield with the active compensation system around. According to Fig. 2.4

The passive shield for the nEDM setup is divided into two parts: an outer and an inner shield. This makes the shield very flexible and modular. The magnetically shielded room (MSR),which is the outer passive shielding (Fig. 2.4(3)) is made of one layer aluminum and two layers of Magnifer®. This is a very high permeability-alloy. The shield covers a cube with the dimension of (2.78 x 2.50 x 2.30) m^3 and the front door has a surface of 1.92 x 2.00 m^2. Through this door the inner shielding and the nEDM setup can be installed inside or other measurement equipment can be sheltered. Inside this room external field changes are shielded with a factor greater than 300 at frequencies less 0.01 Hz [83]. The shielding factor (SF) is defined in [83] by:

$$SF = \frac{B_{woMSR}}{B_{wMSR}} \tag{2.6}$$

where B_{woMSR} stands for the magnetic field measured without the MSR and B_{wMSR}

is the magnetic field with the MSR. In the central cubic meter of the shielded room a field of $700 \pm 200\,\mathrm{pT}$ and a field gradient of less than $300\,\mathrm{pT/m}$ was measured [83]. More details on the characterization of the Munich MSR can be found in [83].
The inner passive shield (Fig. 2.4(4)) is, similar to the outer shield, made of Magnifer®. Here three cubic layers cover an inner cylindrical layer. This inner shield has a SF of more than 4700 at a frequency of 0.01 Hz for an external magentic field of $B_{ext} = 2\,\mu\mathrm{T}$ [84].The inner cylindrical layer is also used for the cosine- theta coil for providing the B_0 and B_1 fields for the nEDM measurement [81]. In combination with the outer shield a SF of $2 \cdot 10^6$ is measured for a frequency of 0.01 Hz [84].

2.4.2 Magnetometers

The neutron storage chambers are surrounded by many different magnetometers. Here only a brief overview on the different systems will be given. The different magnetometer systems are chosen and arranged in the way that all magnetic flied changes can be documented. B_0 drifts can be observed with the ^{199}Hg (co-) magnetometers. Geometric phases with ^{199}Hg (co-) magnetometers and the Cs system. Slowly changing disturbances, e.g. occurring from leakage currents, can be measured with the Cs magnetometers and the Hg magnetometers. The SQUID system is sensitive on fast changing fields, e.g. in a HV discharge, and on higher order disturbances. Here also the Cs system can be used. A detailed discussion of the individual magnetometers can be found in the cited studies in the next sections.

Hg Magnetometers and co- Magnetometer

The usage of a ^{199}Hg co- magnetometer was already done by the RAL-Sussex-ILL collaboration and now used at the PSI and is described in [62] and [85]. For the next generation nEDM in Munich two extra Hg precession cells are installed above and situated under the UCN storage chambers. The precession signal is read out with a laser based system (see Fig. 2.6) instead of discharge lamps in the RAL-Sussex-ILL experiment. The main advantages of using a laser is a power of several mW instead of lower 1 mW with a discharge lamp. With this arrangement a stable, better pumping and multiple readout beams are possible. The common noise is reduced because the read out beam is supplied by one source. Another benefit is that for studying systematic effects the wavelength of the laser can be tuned. However, by using a Hg based magnetometer also the light- shift effect has to be considered because it might be interpreted as a false EDM. More details of the Munich Hg magnetometer

system is described in [79].

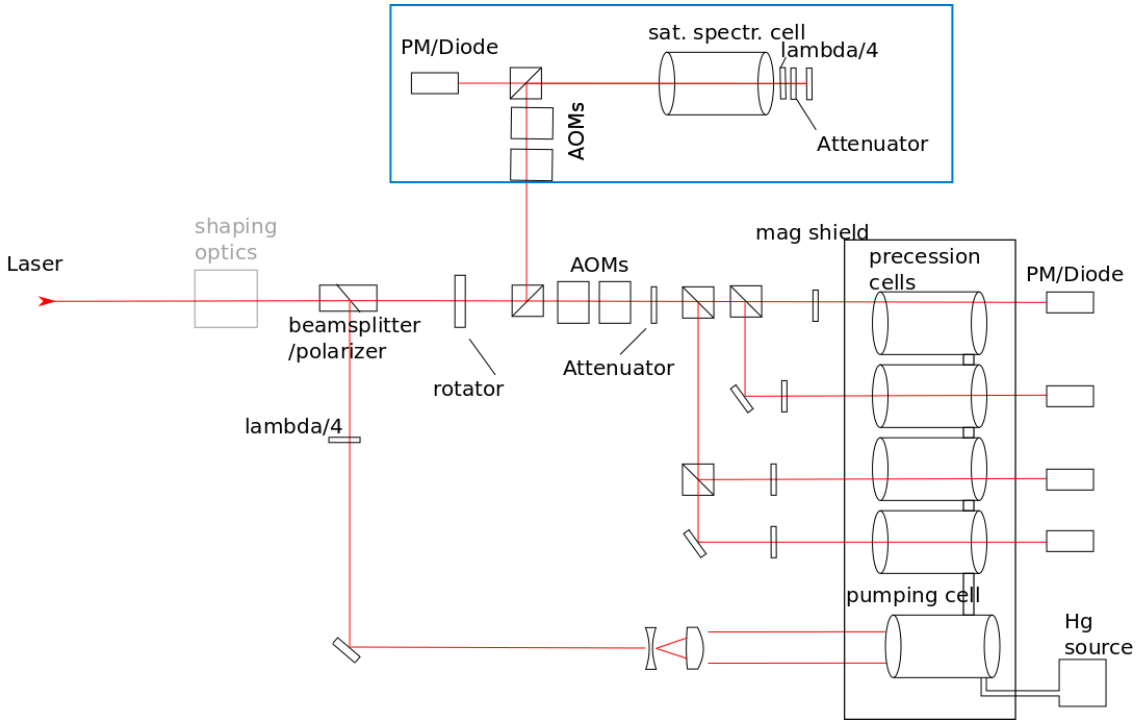

Figure 2.6: Functional diagramm of the optical setup for the Hg magnetometers. The optical path of the laser beam and its preparation is shown in red in the drawing. Taken from [86]

Cs magnetometers

In the Munich nEDM up to 32 scalar Cs magnetometers will be implemented into the online access tubes of the vacuum chamber (see Fig. 2.3 (7)) and in the periphery to track the magnetic field gradients and its glitches during a measurement cycle. The Cs magnetometers work fully optical and are non-magnetic (Fig. 2.7). The functional principal is based on the Faraday effect: The Cs atoms are pumped with a laser into an aligned state, the Cs D2 line. Then a free precession in an external field is following and the optical rotation is measured with a linear polarized probe beam. In [80] the author describes the Cs magnetometer developments in more detail.

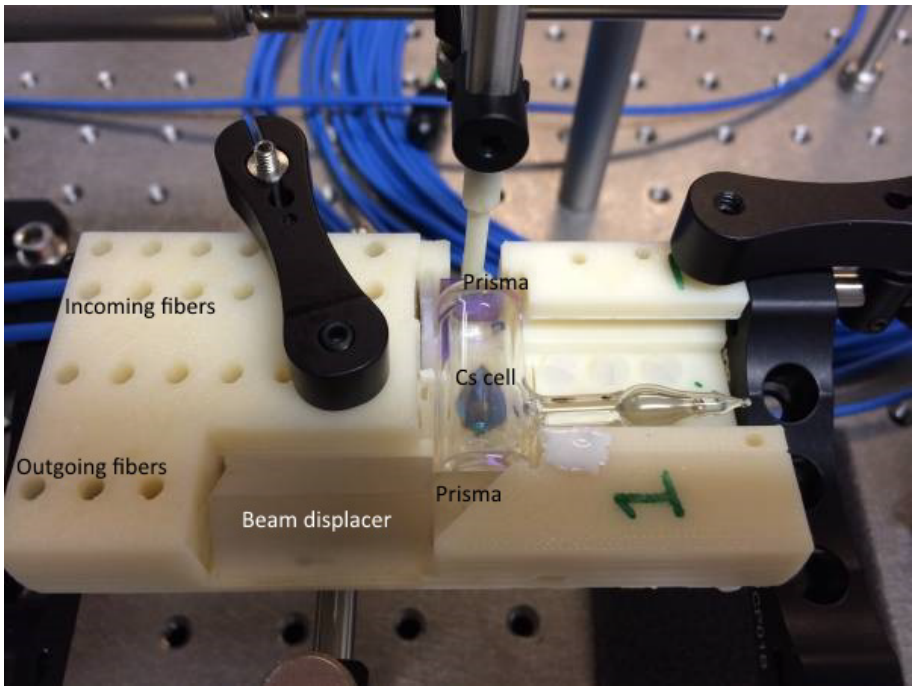

Figure 2.7: Picture of the Cs magnetometer. On the right side Cs magnetometer cell is shown. The incoming fibers are two, one for the probe laser and one for the pump laser. The outgoing fiber is also for the probe laser beam after it was send through a prism the Cs cell one more prism and a beam displacer. Taken from [87]

Superconducting Quantum Interference Devices Magnetometers

SQUIDs are the most sensitive magnetometers available and have a large dynamic range. By positioning several SQUIDs sensors into a sensor head additionally information about the field direction can be collected. For the nEDM setup a special

SQUID type will be used, a so called finger SQUID. Here, the cold head is cooling via a 3 m long copper tube the sensor section which can be inserted in the online access tubes of the vacuum chamber (see Fig. 2.3(7)) down to a temperature of 4.2 K. With this devise the magnetic field fluctuations can be tracked in situ during the EDM measurement. In the sensor head 3 SQUIDs are placed for collecting magnetic field information and additional sensors are mounted for monitoring the field fluctuations of the gradient. More details on SQUID systems in general can be found in [88] and on the here described finger SQUID in [89].

Chapter 3

Neutron Guide System for the UCN Source at the FRM II

Since several years an UCN source is under construction at the FRM II in Munich. To fill the nEDM setup in the neutron guide hall east with neutrons from the UCN source $\sim 60\,\mathrm{cm}$ away from the reactor fuel element, the neutrons have to be transported over a distance of 28 m. Transporting UCNs over such a long distance has never been done before. For common UCN guides made from polished stainless steel tubes the transport of UCNs over such long distances is associated with significant transport losses in the order of a factor of 20.

In order get rid of transport loss issues and to obtain the best performance for the Munich UCN source, two different guide concepts are of interest, both dealing with a decrease in surface roughness. First guide prototypes successfully passed tests at the ILL. The first guide concept, which is commercially available, uses the so called replication technique [90]. Float glass with a minimal roughness of a few angstrom is coated from one side with a material of high neutron optical wall potential e.g. Nickel or its nonmagnetic compounds. After galvanic reinforcement of this layer a self-sustaining sheet can be peeled off from the substrate, resulting in a perfect copy of the glass surface. Starting with optimal parameters of 99 %/m [91] in transmission for guides produced from these sheets, further tests showed some degradation in performance and finally resulted in a transmission of 97 %/m [92]. At the same time, UCN guides produced from glass tubes coated inside with various nonmagnetic Ni compounds were explored. The properties of both guide systems were investigated by [93], [94] for glass guides and by [95] for replica guides. The glass guide technique proofed similar performance and considering also the lower costs, glass guides can be an eligible option for all guide parts, which are not exposed to radiation, as it is the case for the in-pile extraction of the UCN. The following chapters deal with the production and the characterization of a full size guide system of 17 m made of glass tubes. At the beginning the glass has to be prepared (see section 3.1.2). The coatings were performed with a new constructed coating facility at the Maier

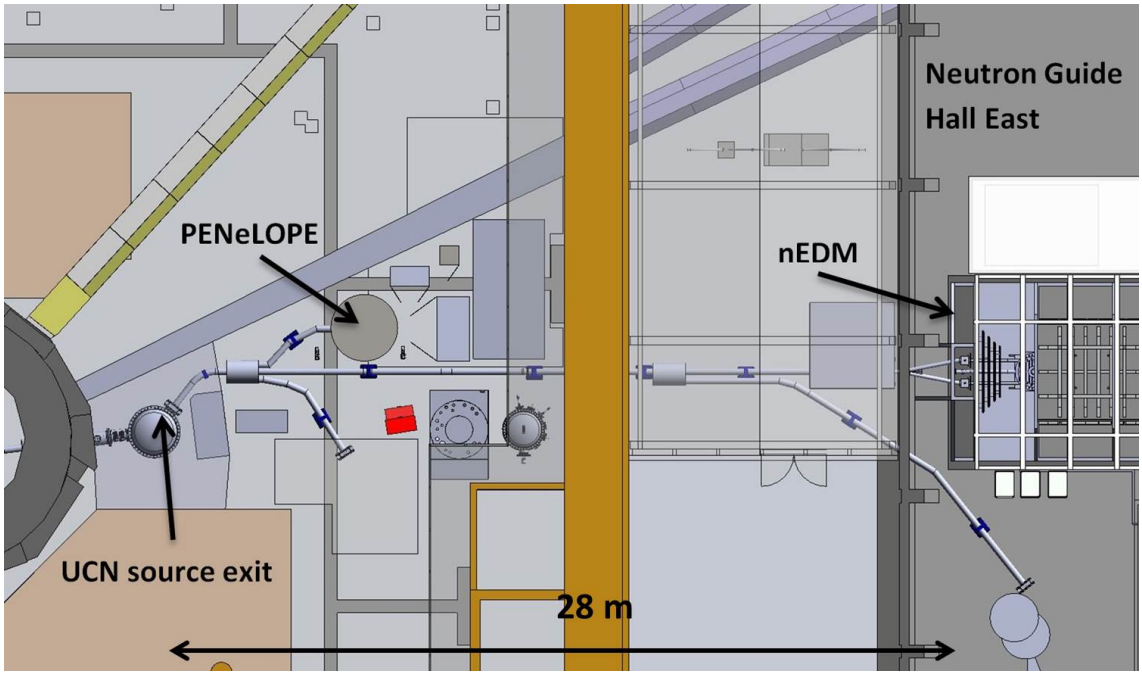

Figure 3.1: Floor plan of the planned UCN source with the UCN guide system to the different experiments. On the right side is the neutron guide hall east with the nEDM experiment. On the left side the reactor side with UCN source and the neutron lifetime measurement setup PENeLOPE is situated. The distance between the source exit and the nEDM setup adds up to 28 m. [27]

Leibnitz Zentrum (MLZ) (see 3.1.1). For the characterization a beam time at the Institut Laue-Langevin (ILL) at the PF2/TEST position was carried out with time of flight (TOF) (see section 3.2.1) and storage measurements (see section 3.2.2). For a complete analysis the whole guide system is simulated with Monte Carlo N-Particle (MCNP) (see Appendix G.4).

3.1 Production of the UCN Guides

3.1.1 Sputter Deposition Facility for Cylindrical Guides

As already discussed previously the guides are produced with a new build coating facility. The 3.6 m long vacuum chamber is divided in three parts with a length of 1.2 m. Each part is accessible through a lid on the top. The sputtering head is mounted from the side as it is shown in Fig. 3.2. Optional an additional head can be mounted from the other side to perform multilayer coatings. In this application

a 500 nm thick NiMo (85/15 wt%) layer is deposed on the inside of a glass tube by the magnetron sputtering technique. The glass tube is placed on a holding system in the way that the sputtering head is in the center of the tube and is moved with a transport system over the sputtering head to create a homogenous NiMo (85/15 wt%) layer. The maximum length for the substrate is 1.6 m with a maximum diameter of 180 mm and a minimum diameter of 50 mm. The cooling lines, the power lines and the sputtering gas line (here Argon) is guided through a hollow stainless steel tube to the sputtering head (see Fig. 3.2).

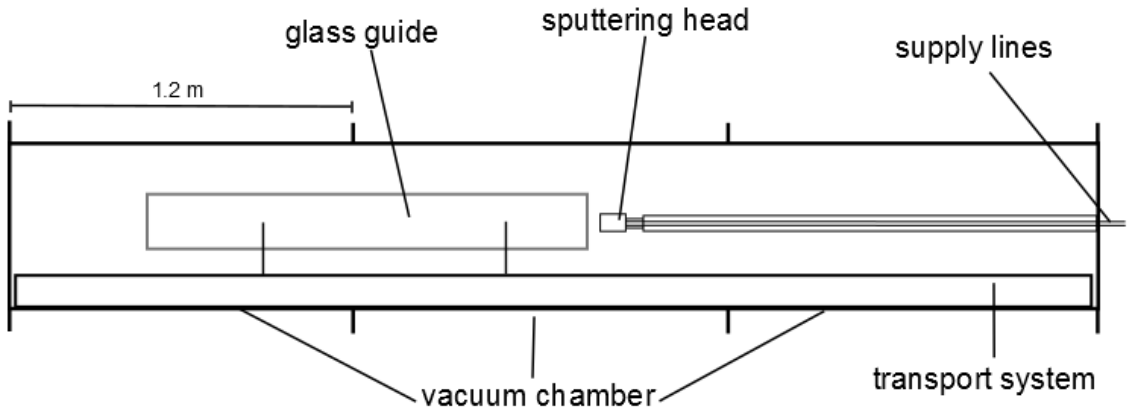

Figure 3.2: Illustration of the sputtering facility. On the right side the sputtering head is mounted on an lance into the chamber and from the left side the glass guide is moved with a transport system over the sputtering head. The vacuum vessel consists of three segments.

3.1.2 Preparation of the Substrate

As substrate served a Schott Duran® glass tube [96] with an inner diameter of 115 mm, a length of 1.5 m and a wall thickness of 5 mm. Curved guides were realized by polygon sections each with an angle between 11° and 12°. It depended on total angle which angle parts were selected for the required bend section. They were fixed together with an ultraviolet glue. The bends were vacuum tight and self supporting. For an optimal alignment of the guide system a support structure, made of aluminum scaffold is used.
For the application as an UCN guide, the edges of the glass tubes have to be parallel plane for a later perfect assembling. The pretreated tubes are polluted with dust

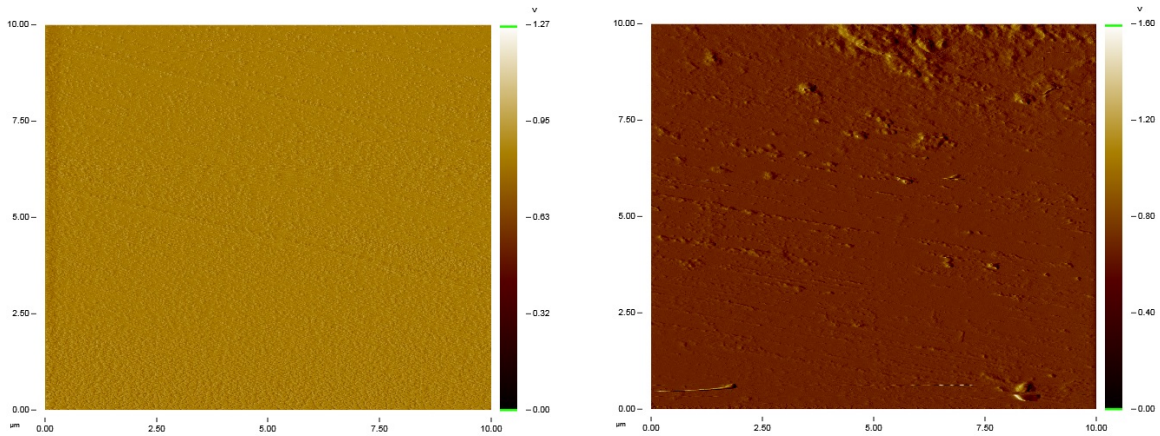

(a) Neutron guide with a well substrate preparation shows a roughness of 1 nm

(b) Neutron guide with a poor substrate preparation shows a roughness of 30 nm

Figure 3.3: AFM picture of a 10 x 10 μm examined piece of the inner wall of an UCN guide coated with 500 nm NiMo (85/15 wt%).

and other debris from the previous treatment, which causes large influences on the later properties of the neutron guide, as it is examined in Atomic Force Microscope (AFM) studies (see Fig. 3.3). For a perfect prepared and cleaned substrate with a 500 nm thick NiMo (85/15 wt%) layer a surface roughness of 1 nm is measured (see Fig. 3.3(a)). Compared to the measurement shown in Fig. 3.3(b) of an incorrectly performed cleaning process a 26 nm roughness was obtained and shows how important this process is.
First the glass tubes where cleaned in an ultrasonic baths (at 50 °C); five minutes in a Tickopur R 27 solution and after that in distilled water. After this preparation the inner side of the glass guides was further prepared with acetone and ethanol. In the next step they were heated for 12 hours at a temperature of 200 °C in a vacuum oven.The still hot tubes were placed in the sputtering facility and pumped down to a pressure of 10^{-7} mbar.

3.1.3 Measurement of the Neutron Optical Potential of the Coating

For a full characterization of the guide system the neutron optical potential of the used material has to be measured. All used glass neutron guides are coated with a layer of 500 nm NiMo (85/15 wt%). For getting this information the critical angle of the coated material was measured. Therefore two reflectometer measurements with cold neutrons are performed. One with a planar sample at the TREFF [97] with a

wavelength of 4.8 $\AA$ and one in situ in a coated UCN guide with MIRA [98] with a wavelength of 4 $\AA$. Both instruments are located at the FRM II in Garching. For the

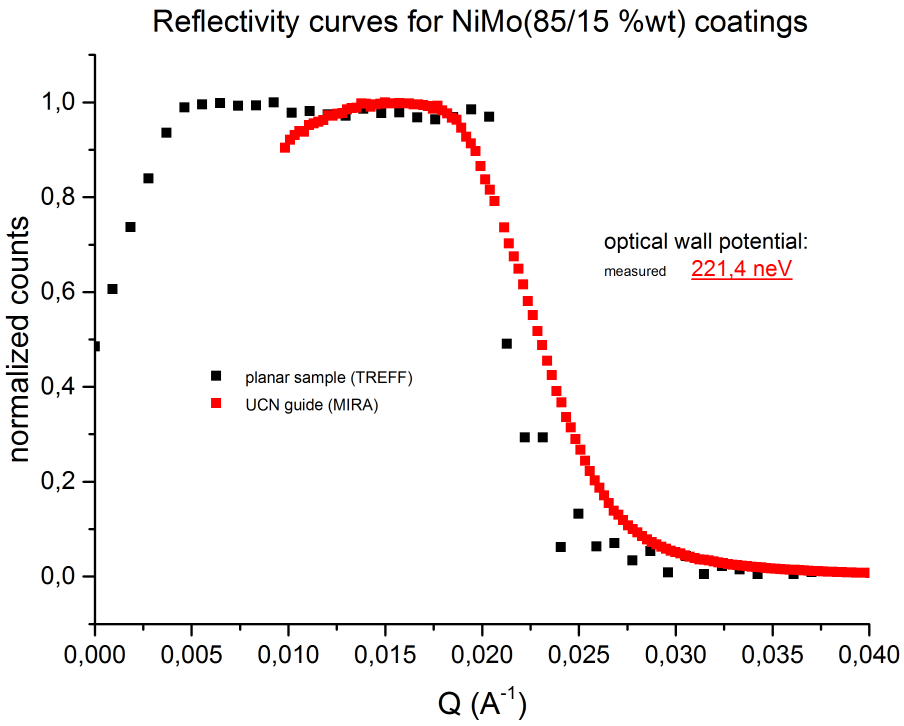

Figure 3.4: Reflectivity curves for NiMo (85/15 wt%) coatings. The measured curve indicated by the black squares shows the data for a planar sample, measured at TREFF [97] and the curve indicated by the red squares shows the data for a measurement at MIRA [98] direct in a coated guide section. The result for the neutron optical potential is $V_F = 221$ neV. The error bars are to small and are not visible.

measurement at MIRA the cold neutron beam was collimated to an area of 1 x 1 mm^2 to minimize systematic effects caused by the curved surface of the guide. But an effect is visible in the results, as it is shown in Fig. 3.4. The drop of the counts for this measurement is much softer than for the measurement with the planar sample at TREFF. Nevertheless, both results of both measurements are compatible. In Fig. 3.4 the momentum transfer is shown on the x axis and is linked to the critical angle θ and the critical wavelength by the following relation:

$$Q_c = \frac{4\pi}{\lambda_c} \sin(\theta_c) \tag{3.1}$$

With this relation for a Q of 0.02038 a $\theta = 0.446°$ was calculated. Using the following relation between the critical angle of the material with the coherent scattering length

on the bound nucleus b and the density of atoms N

$$\theta_c = \lambda \sqrt{\frac{N b_{NiMo}}{\pi}} \tag{3.2}$$

b_{NiMo} is $8.26 \cdot 10^{14}\, 1/m^2$ and is connected to a optical potential of 221.4 neV.

3.2 Characterization of the Guide System

The purpose of the measurement was to characterize a guide system comparable to the future FRM II UCN neutron distribution system. In various experimental arrangements, including time of flight and storage measurements with the complete guide system and single guide segments, the preferred glass guides could be characterized in detail.

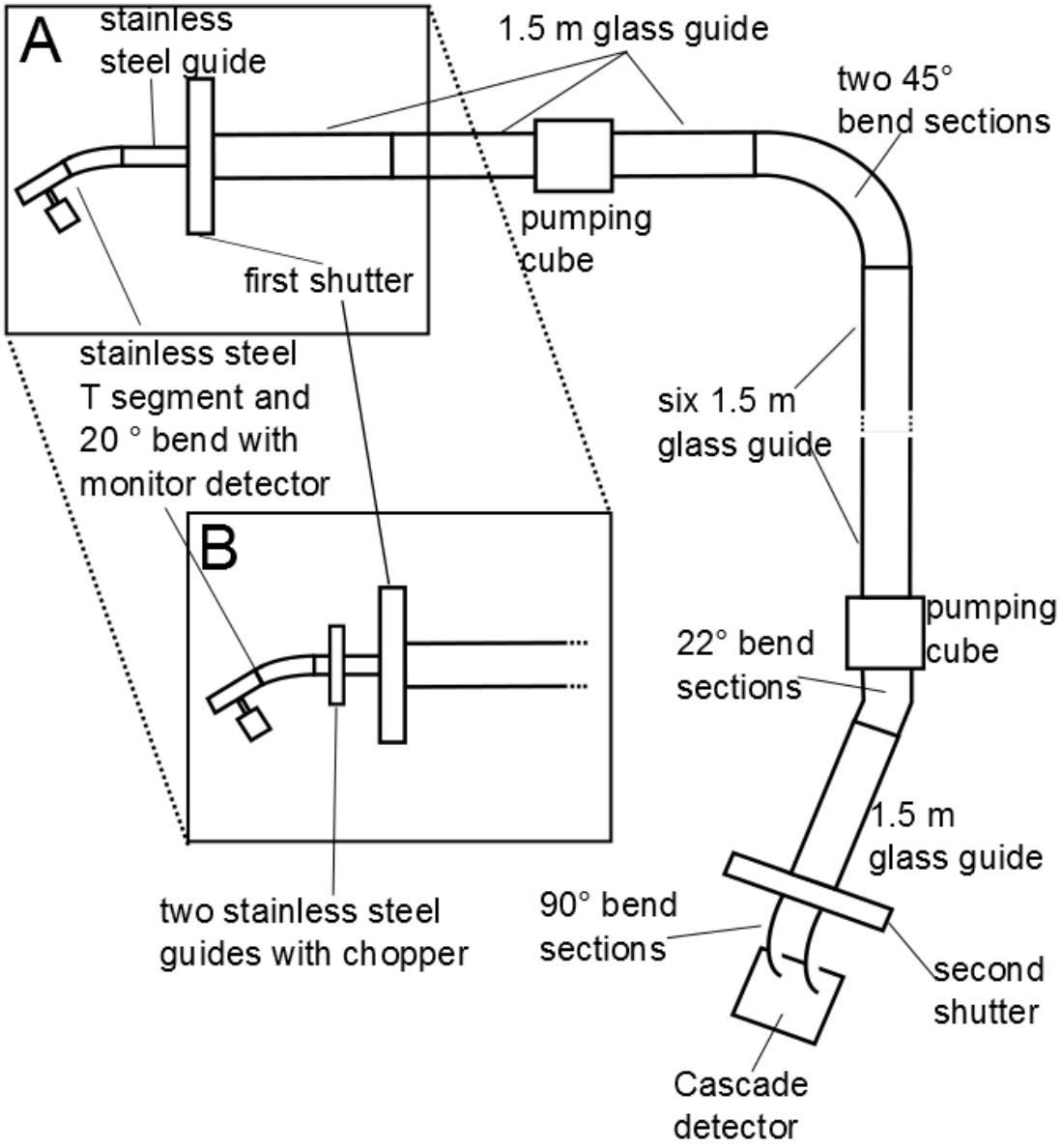

Figure 3.5: Experimental setup for the measurement. Version (A) was used for the storage measurement and version (B) for the transmission measurement.

Fig. 3.5 (A) and (B) show a sketch of the longest version of the installed experimental setup; (A) for the storage measurements, (B) for the TOF measurements. The neutrons were guided from the source on the left side through a 0.2 m long guide with a 0.01 m diameter hole to split the beam for a monitor cascade detector [99] (Fig. 3.5). Behind the T- segment the main beam is entering the setup from the left side through a 20° stainless steel bend section (Fig. 3.5) and a 40 cm long stainless steel guide for the storage measurements (Fig. 3.5 (A)). All used stainless steel components had an inner diameter of 66 mm and an outer diameter of 70 mm for the storage measurements. Stainless steel guides were used because for the beam line exit at ILL these guides are used and the transition to glass guides was done at a suitable position. In the case of the TOF measurements (Fig.3.5 (B)) the 40 cm long guide was replaced by a linear chopper with two guide segments one 0.30 m and the other being 0.09 m compatible to the 40 cm stainless steel guide (Fig.3.5 (B)). The complete setup described in the following is similar for the TOF and storage measurements. The next component was the first shutter (Fig.3.5), also acting as a transition flange between the 70 mm stainless steel guides and the 125 mm glass guides coated with NiMo (85/15 wt%). The first 4.5 m glass guides, consisting of three 1.5 m long guides (Fig. 3.5) are guiding the UCNs through two 45° bend section (Fig.3.5). Then the next six 1.5 m long guide segments (Fig.3.5) are assembled horizontally on an aluminum support structure. After a 22° bend (Fig.3.5) another 1.5 m guide section (Fig.3.5) is mounted, followed by the second shutter (Fig.3.5). Behind the shutter a 90° bend (Fig.3.5) is used in front of the cascade detector [99] (Fig.3.5) to accelerate the UCNs for passing the aluminum entrance window of the detector.

The experimental procedure was the following: In each configuration of the setup a storage measurement and a transmission measurement is performed. Therefore, the guide system is ventilated and a linear chopper is mounted in the beam line as shown in Fig. 3.5 (B). For the nominal reactor power of 30 MW a standard deviation of 0.15 MW is diagnosed with the logged reactor power. In the past, observed count rate fluctuations were much higher than expected, resulting from reactor power fluctuations. Also other groups [93], [100], [101] reported much higher variances in the count rate than expected from reactor power fluctuations and by changing the setup. As it is discussed by Daum et al. in [93], therefore, a T-segment with a monitor counter right behind the exit of the UCN Turbine (Fig.3.5) is used to circumvent the observed fluctuations.

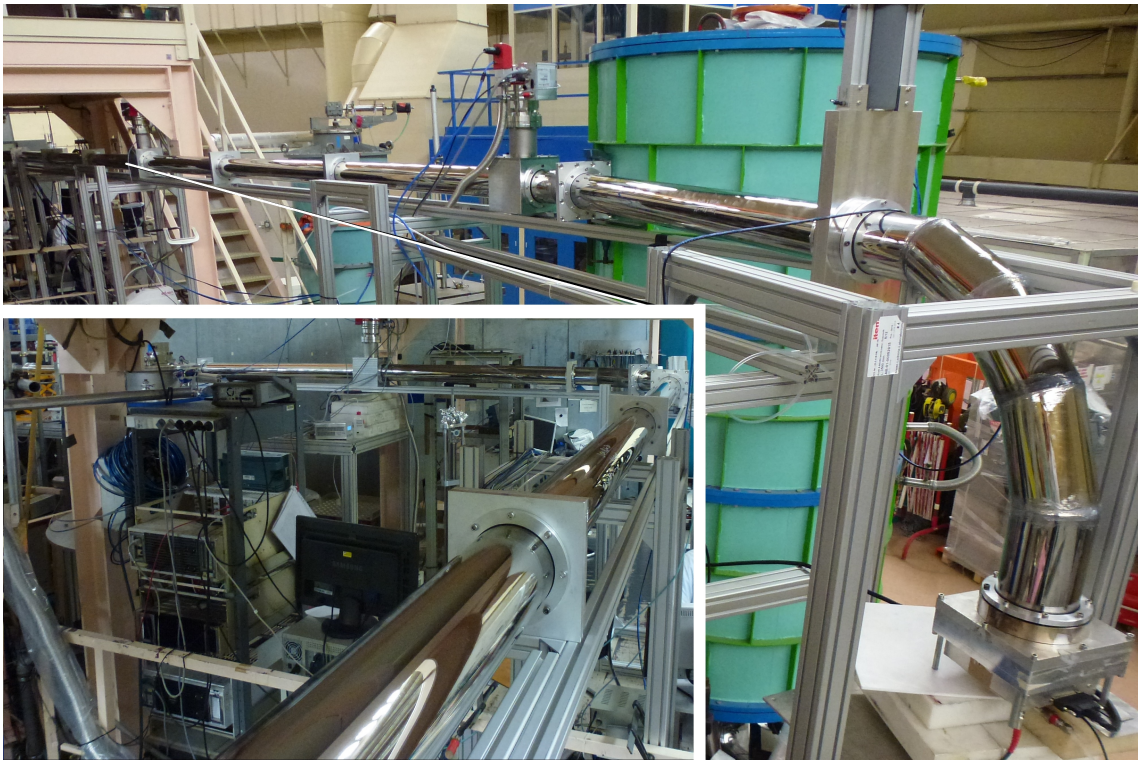

Figure 3.6: Picture of the experimental setup at the ILL. In the lower left corner the first meters of glass guides from the UCN turbine to the two 45° bend section and further to the detector is shown. The big picture shows the 22° and the Cascade detector with the 90° bend. The whole setup was mounted on an aluminum support structure.

3.2.1 Time of Flight Measurement

To characterize the complete system time of flight measurement (TOF measurements) are performed to examine the UCN transmission. Therefore, measurements with and without the UCN guide section are performed and with both results, corrected from the background rate, the ratio is calculated [22] with

$$T_{guide} = \frac{N_{withguide}}{N_{ref}}. \tag{3.3}$$

The measurement time was varying between 12 and 24 hours depending on the count rate at the detector to collect sufficient statistics to reach a statistical uncertainty of less than 0.1 %. Also the measured data are scaled with the monitor detector data. The background rate with closed beam line shutter is varying between the measurements, because of the different distances of the detector from the beam exit PF2/Test. For the setup with the longest distance to the PF2/Test beam line exit

a background count rate of 0.02 counts/s is determined. And for the closest, the reference measurement, 0.25 counts/s as background is measured.
For taking the TOF data a well characterized chopper system [102] is reverted. This chopper system bases on two linear driving stages. Each is connected with a grid made of Titanium in the UCN beam line. With this system the neutron beam can be blocked in the closed position and a well defined UCN bunch can pass it, when the grids are in the open position. Comparing this system with a classic disc chopper system, the advantage of a linear chopper system is the high flexibility in adjusting the open to close ratio to the length of the neutron guide system. For the different lengths of the setup the different opening functions with the same open to close ratio is adjusted in order to get the best resolution:

- For the full length system the chopper was opened for 200 ms every 20 seconds with an offset of $t_{off} = 116$ ms between the trigger signal for the detector and the opening of the chopper.
- For the reference measurement the chopper was opened for 20 ms every 2 seconds with an offset of $t_{off} = 27$ ms between the trigger signal for the detector and the opening of the chopper.
- For the 6.6 m guide length and all the other intermediate guide length the chopper grid was opened for 10 ms every 10 s with an offset of $t_{off} = 66$ ms between the trigger signal for the detector and the opening of the chopper.

For a flightpath of 15 m the results are shown in Fig. 3.7. For all measurements the 90° bend section (Fig.3.5) and the detector (Fig.3.5) is relocated at the respective positions. Both were situated after the first 1.5 m glass guide (Fig.3.5) for the reference measurement and for the characterization of the 2 x 45° bend section (Fig.3.5) a measurement before and behind the bend is performed. The same procedure is applied for the 22° bend section (Fig.3.5).
An example of these spectra is given in Fig. 3.7 for the 15 m distance, where the transmission T for the different optical components is calculated with equation 1.33 for the three velocity regions (4.5 - 6 m/s), (6 - 8 m/s) and (8 - 10 m/s). In the analysis only the part of the UCN spectrum with a minimum velocity of 4.5 m/s is considered, corresponding to the optical potential $V_F = 107$ neV [103] of the Aluminum separation foil, which was contaminated with a thin layer of Fomblin oil.

For future experiments the velocity region between 4.5 - 6 m/s is the most interesting part of the spectrum i.e. a nEDM or a neutron lifetime measurement because these are the storeable UCNs.

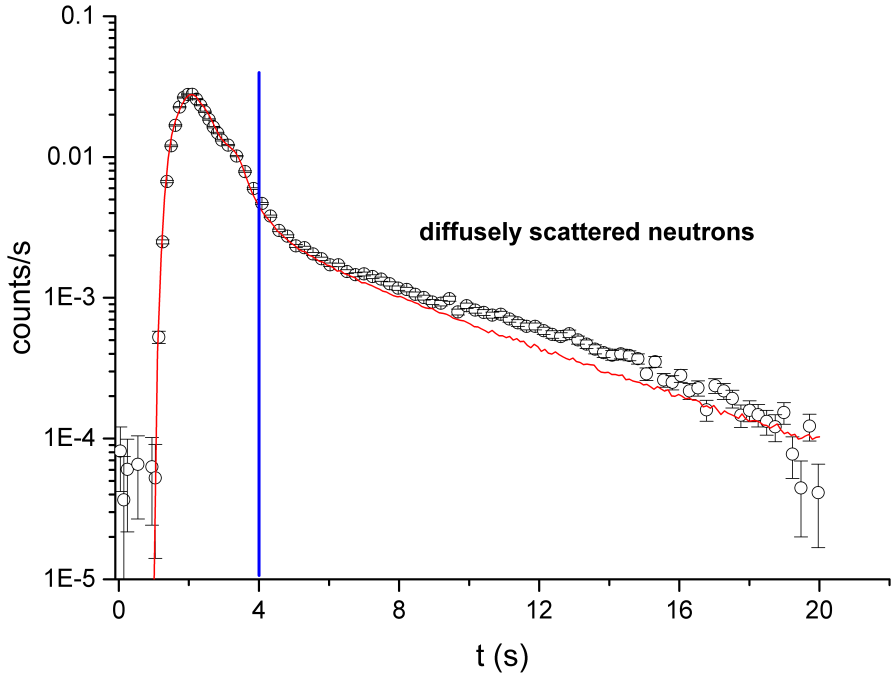

Figure 3.7: TOF spectrum for the 15 m long guide system. For flight times greater than 4 s (blue line) all neutrons are diffusely scattered. The red curve represents the best fit performed for this spectrum. The error bars arise from Poison statistics.

All neutrons with a velocity lower than 4.5 m/s are diffusely scattered neutrons because UCNs with a lower velocity are reflected at the with Fomblin contaminated aluminum window. For the spectrum of the 15 m guide (Fig. 3.7) UCNs, which are reaching the detector in the time range between 4 s and 20 s, are diffusely scattered. These neutrons are quasi stored in the guide system and are not specular reflected. These neutrons are not contributing to the transportable spectrum (see section 3.2.3). Some of them are stored up to 20 s in the system before they are detected or lost.
The transmission results for the higher velocities up to 10 m/s are also interesting for experiments, which are using this part of the spectrum, i.e. a magnetic bottle experiment or experiments manipulating the spectrum by guiding the neutron upwards.
The results of the transmission measurements are shown in Tab. 3.1. For the velocity region of 4.5 - 6 m/s the whole guide system showed a transmission of 34.9 $\pm$ 0.2 %. Also the results for all used optical components is shown in Tab. 3.1. From the transmissions, listed in Tab. 3.1, the following calculation can be made by following

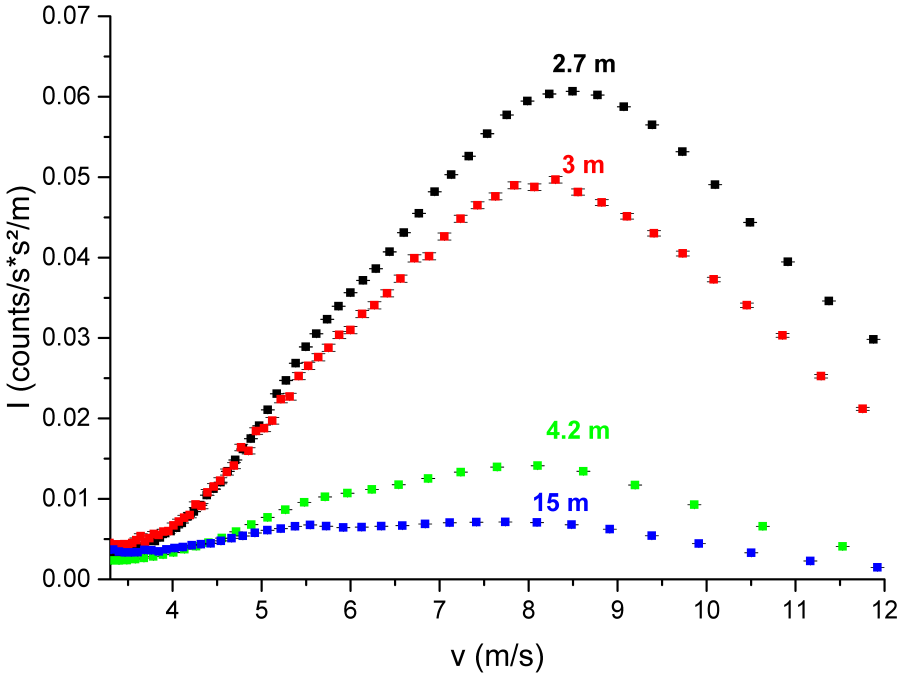

Figure 3.8: TOF spectra for different length of the guide system in dependence of the velocity. The error bars arise from Poisson statistics and error propagation.

Equation 1.34:

$$T_m = \left(\frac{T_{full}}{T_{2x45^\circ} \cdot T_{2x45^\circ} \cdot T_{shutter} \cdot T_{slits}} \right)^{1/13,5} \tag{3.4}$$

Giving $T_m = (96.1 \pm 0.6)\%/m$ for a velocity between 4.5 - 6 m/s. These results are in good agreement with further results in [93] of $T_m = (92.9 \pm 1.3)\,\%/m$, according also for the bigger guide radius is taken into account for the presented results in Fig 3.7.

3.2.2 Storage Measurement

For the storage measurements UCN shutters are develop and build. A detailed description can be found in [104]. The concept is based on the movement of a guide section (open) or alternatively a cap made of a silicon wafer, coated with NiMo (85/15wt%) glued on an aluminum support structure (closed) with a pressed air cylinder into or out of the beam. In the closed position the cap is pressed against the end of the storage cell to minimize the UCN losses caused by leakage through

guide sections	10-8 m/s [%]	8-6 m/s [%]	6-4.5 m/s [%]	6-4.5 m/s with delayed UCN [%]	comments
15 m	10.5 ± 0.1	15 ± 0.1	34.9 ± 0.2	53.1 ± 0.3	maximum guide length
3 m	77.4 ± 0.3	88.7 ± 0.2	98.8 ± 0.1	99.8 ± 0.1	two 1.5 m guides
4.2 m	42.4 ± 0.1	54.2 ± 0.2	83.4 ± 0.3	96.0 ± 0.3	2 guides & 2 x 45 ° bends
2 x 45 ° bends	51.7 ± 0.2	60.4 ± 0.2	86.7 ± 0.4	86.9± 0.4	only the bend
shutter & bend	76.7 ± 0.4	80.9 ± 0.5	95.5 ± 0.7	95.3 ± 0.7	with 22 ° bend
shutter	92.3 ± 0.5	89.4 ± 0.5	95.1 ± 0.7	95.2 ± 0.7	

Table 3.1: Results of the transmission measurements in [%] for different guide lengths and sections. The errors arise from Poisson statistics and from Gaussian error propagation.

gaps. For this position the measured gap was less than 0.03 mm, which corresponds to a measured UCN leakage rate of < 0.2 counts/s. In the open position a total gap of 0.5 mm in between the guide system and the guide section in the shutter is diagnosed.
The length of the storage volume is varied between 1.5 m and 15.5 m. Also a measurement in the last 1.5 m section, in front of the detector is performed to evaluate the transport properties of the guide system, also with the storage method. Furthermore, a storage measurement for each 1.5 m long guide section used in the experiment is carried out under the same measurement conditions.
A single storage measurement is always performed by following the listed steps:

1. **Cleaning time** 100 s**:** (Shutter positions: First closed, second open) This step was only performed once before the very first measurement of a cycle to empty the guide system and to avoid having undesirable neutrons in the system
2. **Filling time:** (Shutter positions: First open, second closed) The time depending on the length of the guide system, for example 150 s for the longest guide system
3. **Storage time:** (Shutter positions: First closed, second closed) The time was varied to get the storage curve
4. **Emptying time:** (Shutter positions: First closed, second open) The stored neutrons were emptied into the detector. The time was also adjusted to the guide system length.

As already mentioned, the filling time has to be optimized before a storage curve measurement can be carried out. For all the different guide length the described measurement sequences is used with adjusted filling time and constant storage time. The filling curve for the 15.5 m system is shown in Fig. 3.9.

By fitting an exponential attenuation curve, a filling time of 150 s can be chosen. Also for the storage in an 1.5 m guide section at the end of the longest setup, the filling time of 150 s is used. For the 1.5 m the filling time was 40 s and for the 4.5 m and 5.5 m only 50 s. The same time parameters are used as emptying time.
For the storage measurements the background rate with closed beam line shutter is also varying between the measurements, depending on the distance from the beam exit PF2/Test. For the setup with the longest distance to the PF2/Test beam line exit a background count rate of 0.02 counts/s is determined. And for the closest, the reference measurement, 0.25 counts/s as background is measured. All data taken are corrected for the corresponding background count rate.

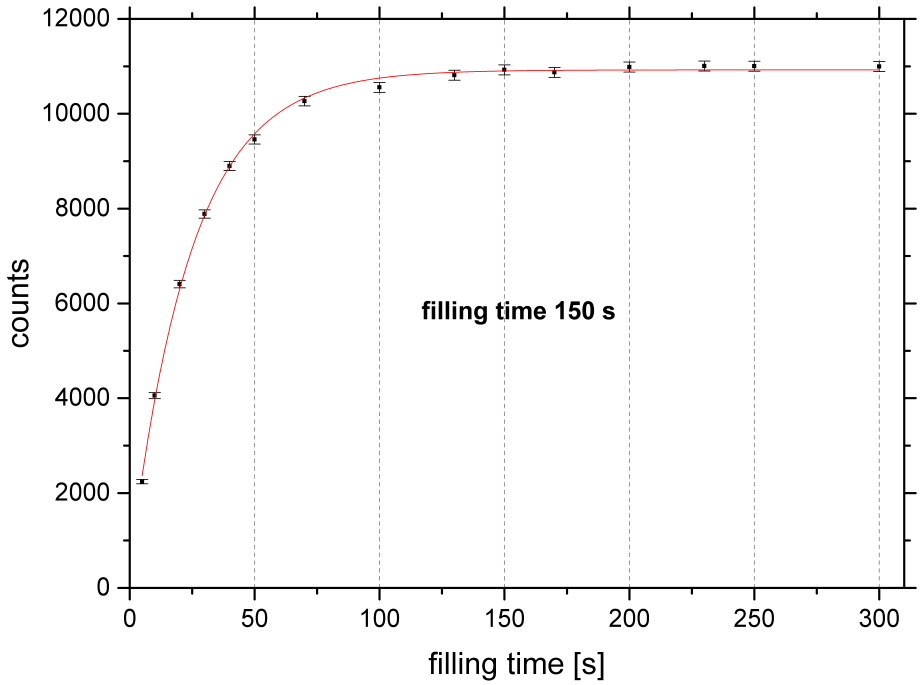

Figure 3.9: Filling time curve for the 15.5 m guide system. From the exponential fit a filling time of 150 s is determined. The error bars arise from Poison statistics.

For determining the effective neutron lifetime in the storage vessel and the initial UCN density in the volume a storage curve is measured, (i.e. for the 15.5 m shown in Fig. 3.10) by varying the storage time from 5 to 150 s.
For the data analysis an exponential decay function is used:

$$N(t) = A_1 e^{-t/\tau_1} \tag{3.5}$$

with A_1 beeing the initial UCNs at t= 0 s in the setup and τ_1 is the effective lifetime of the neutrons in the storage vessel. The first 20 s are set as cleaning time, because in this time also marginally trapped neutrons with a higher kinetic energy than the optical wall potential $V_{F,NiMo}$ are stored.
The corresponding storage curve together with the fit is shown in Fig. 3.10 and the results for the effective lifetime and the neutron density at t = 0 s in the different arrangements following from the fits are listed in Tab. 3.2. Comparing the lifetime and the neutron density for the 1.5 m long guide sections it is clear, that the performance of each guide is on a constant high level of 37 s storage time and an UCN density of 0.28 UCN/cm^3, considering the errors is reached. This result leads to

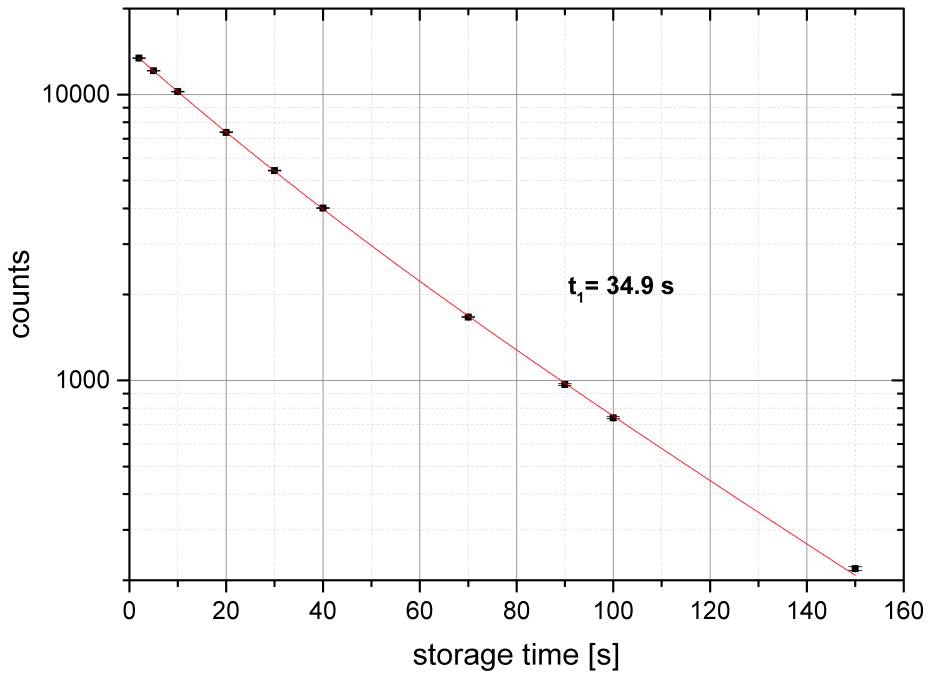

Figure 3.10: Storage curve for the 15.5 m guide system with a vacuum pressure of $8.3 \cdot 10^{-6}$ mbar. The fit is an exponential decay function. The corresponding fit results are listed in Tab. 3.2 and the error bars arise from Poison statistics.

the conclusion that the quality of the sputtering process for the neutron guides is well understood and reproducible. Also the influence of the vacuum on the storage properties in the 15.5 m long guide system is investigated (Tab. 3.2). As expected the effective lifetime of the neutrons in the guide system is increasing with the improvement of the vacuum. For the 15.5 m guide an effective lifetime of 34.9 s and an initial UCN density of 0.08 UCN/cm^3 is determined. Collated with the lifetime in 1.5 m it is obvious that the lifetime is in the same range and the UCN density is one third of the density in the short storage volume. The lower density can be explained with the bigger volume of 200 dm^3 and the transmission properties of the system. Comparing the results for the UCN density of guide no. 23 installed as the first segment with the density for storage in the last section it is clear that also only one third of the neutrons can be stored after a transportation of 14 m (Tab. 3.2). This result is in good agreement with the result for the 15.5 m and confirms the assumption in Section 3.2.3.
Since the effective lifetime is defined by Equation 1.35 in section 1.3.2 it is possible

to determine with τ_l the storage method the loss rate η for NiMo (85/15 wt%). Here $\tau_n = (880.3 \pm 1.1)$s [23] is the lifetime of the neutron, τ_l is the lifetime of the losses by absorption at the walls and up scattering and τ_{sl} are the losses due to slits. First τ_{sl} for the storage in a 1.5 m long guide is derived.The already mentioned gap at the end caps of the shutters of 0.03 mm are taken into account for slits and an estimated gap due to misalignment of 0.1 mm is considered. This results in an area of $A_{sl} = 43\,\mathrm{mm}^2$ of full absorbing slits.
First τ_l the loss probability per wall collision for the mean energy is obtained:

$$\bar{\mu}_{mat}(\bar{E}) = \frac{4 \cdot V_s}{A_s \cdot \bar{v} \cdot \tau_l} \tag{3.6}$$

with $\bar{v} = 3/4 \cdot v_{max}$, and v_{max} is the maximum velocity corresponding to the neutron optical potential $V_F = 221$ neV (Fig. 3.4). An 1.5 m long guide has a volume of $V_s = 15.6 \pm 0.3$ dm^3 and a surface of $A_s = 54.2 \pm 0.5$ dm^2. With this relations the loss probability per wall collision for the NiMo (85/15 wt%) coating in a 1.5 m long guide to $\bar{\mu} = (4.1 \pm 0.3) \cdot 10^{-4}$ can be calculated. Using the relation between the loss probability per wall collision and the energy independent loss rate, it follows:

$$\mu_{mat}(E) = 2\eta \left[\frac{V}{E} \arcsin \left(\frac{E}{V} \right)^{1/2} - \left(\frac{V}{E} - 1 \right)^{1/2} \right] \tag{3.7}$$

and a value for $\eta = (2.7 \pm 0.3) \cdot 10^{-4}$ can be derived. Compared with the theoretical value of $\eta = W/V_{eff} = 2.5 \cdot 10^{-4}$ the result of the measurement is in good agreement with it. Here W is the imaginary potential of the wall material.
With this result the medium length of the slits in between two guides in the storage volume of 16.3 m was determined to be 0.1 mm. Slits are mainly caused by misalignment and in pumping cubes the gaps are deliberately made for pumping the guide. Nevertheless, the results are promising for the future guide system at the FRM II, because the losses due to slits are not dominating the storage and transport properties of the guide system, and with further optimization of the accuracy of the neutron guide alignment for a future transport system at the FRM II UCN source the losses can be further minimized.

3.2.3 Diffusely Scattered UCNs

In the TOF spectra the delayed neutrons, which are diffusely scattered on their flight path, can be confined and further analyzed. These neutrons are shown in Fig. 3.7 in the region between t =4 s (marked with a blue line) and t =20 s. These delayed neutrons are an indicator for the roughness of the UCN guides. A higher roughness leads

length [m]	t_1 [s]	density [$1/cm^3$]	comments
1.5	36.8 ± 0.8	0.27 ± 0.01	guide no. 7
1.5	40.2 ± 1.0	0.29 ± 0.01	guide no.8
1.5	37.4 ± 0.7	0.28 ± 0.01	guide no. 12
1.5	35.7 ± 0.8	0.28 ± 0.01	guide no. 13
1.5	35.5 ± 0.8	0.28 ± 0.01	guide no. 16
1.5	35.3 ± 1.1	0.27 ± 0.01	guide no. 17
1.5	36.4 ± 0.9	0.27 ± 0.01	guide no. 20
1.5	37.4 ± 1.0	0.27 ± 0.01	guide no. 21
1.5	35.3 ± 0.7	0.27 ± 0.01	guide no. 22
1.5	39.1 ± 0.8	0.27 ± 0.01	guide no. 23
1.5	37.3 ± 1.0	0.09 ± 0.01	guide no. 23 last guide before detector
15.5	34.9 ± 0.6	0.08 ± 0.01	complete guide system vacuum $8.3 \cdot 10^{-6}$ mbar
15.5	32.7 ± 0.5	0.08 ± 0.01	complete guide system vacuum $3.2 \cdot 10^{-3}$ mbar
5.5	32.5 ± 0.6	0.20 ± 0.01	3 guides & 2 x 45 ° bends
4.5	34.0 ± 0.5	0.20 ± 0.01	first 3 guides

Table 3.2: Results for storage measurements in different guide length and vacuum conditions. The errors arise from Poison statistics and error propagation.

to a bigger amount of diffusely scattered neutrons, a worse transmission through the system and in turn to less neutrons for experiments. In combination the result for the storage measurement in the last guide in front of the detector with a feeding guide of approximately 15 m with a result of one third of the density measured in a guide direct behind the turbine exit. Comparing this value with the transmission through the 15 m long guide system of 34.9 ± 0.2 % without the diffusely scattered UCNs it is clear that these diffusely scattered neutrons are not contributing to a neutron flux to fill a storage experiment. Furthermore, they have a longer flight path through the guide system and perform more wall collisions. Therefore, they have a higher possibility to get lost by absorption, up scattering or escape through slits. In former transmission and storage measurements these diffusely scattered neutrons were never visible because of the measuring method and the setup configuration [95]. To get a value for the diffusely scattered neutrons, also Monte Carlo simulations with a modified code presented in [42], [105] and in Appendix G.4 for the guide system are

performed. An example is given in Fig. 3.7 (red curve), showing the best result of the simulation. With the simulation of the longest guide system an amount of 4 % diffusely scattered neutrons is determined. For the reference measurement the best agreement is achieved for a diffusely scattered UCN part of 0.5 %. This shows that the number of diffusely scattered UCNs increase with the length of the system [42]. Compared with UCN guides made of stainless steel, with a diffusely scattering part of 6 % for shorter guide systems, the achieved results in this work are notable improvements. For further investigations the matter of diffusely scattered UCNs in dependence of the guide length might be interesting and can be helpful for the further understanding of long UCN guide systems.
If the diffuse part of the spectrum with a velocity less than 4 m/s is considered, here, a value of $T_m = 99.2 \pm 0.6\%/m$ is diagnosed. This leads to the same result of measurements as it was performed in [91], where the diffusely scattered neutrons are not considered. Both results show transmission values over 99 %.

3.3 Conclusions to the Neutron Guide System for the UCN Source at the FRM II

With the results presented in this chapter an effective and cheap possibility is presented to transport UCNs, which are produced at the source 27 m away from the experimental area of the future nEDM. The inner guide surface is characterized with an AFM and are produced with the sputter technique with a 500 nm thick layer in house. For the storage measurement a shutter system with a measured UCN leakage rate of less than 0.2 Counts/s are build.
With the performed measurements for the first time the UCN transmission and storage characteristics of a 17.7 m long guide system could be demonstrated. The results showed that the guides have a reproducible high storage time of approximately 37 s and the transmission per meter is in the range of $T_m = 96.1 \pm 0.6\,\%/m$ for a velocity between (4.5 - 6 m/s). The storage time for UCNs in the complete guide system reduces to 34.9 ± 0.6 s. This loss can be explained with bigger slit area. The loss factor is determined to be of the order of $\eta = 2.7 \pm 0.3 \cdot 10^{-4}$ and is compared to the theoretical value of $\eta = 2.5 \cdot 10^{-4}$ in good agreement. For the transmission through the complete guide a part of 4 % of the UCN were diffusely scattered and these neutrons are not contributing to an UCN flux for filling a storage experiment.

Chapter 4

Neutron Handling System for nEDM

The transport and preparation of UCNs related to the sensitivity of the measurement is not negligible since the number of UCN has an influence via the $\sqrt{N}$ term in the sensitivity equation 2.4. This results for a next generation nEDM in the demand of high quality UCN handling components without influencing any other component of the nEDM.
The neutron handling system for the Munich nEDM project consists of several parts. Starting with non depolarizing straight guides (section 4.1), next the polarization device followed by beam splitters for dividing the beam into two equal parts for filling the two nEDM chambers where the Ramsey measurements take place (section 4.2). The later detection of the stored UCN will be done with simultaneous spin detection. Therefore, a special beam splitter was build and will be described in section 4.2. For each nEDM chamber a three way neutron switch is needed to guide the neutrons in the desired direction, which will be described in section 4.3.
The demands on the precession chambers are of high complexity. A long storage time in the double- chamber for the UCNs is essential for the Ramsey's method of separated oscillatory fields. However, not every material with a high neutron optical potential is qualified for this purpose. The electrodes should be non depolarizing and electrically conductive for the high voltage and should not disturb the high accuracy magnetic field measurements around the chamber. The main concerns on the insulator rings are a high insulation, but also the remaining claims, as for a neutrons guide, need to be satisfied for the high voltage electrodes. The storage chamber properties will be discussed in section 4.5.

4.1 NiMo Coated Neutron Guides

For the next generation nEDM project at the FRM II source the decision to use glass guides coated with NiMo (85/15 wt%), also for polarized UCN, is made because they have the following properties.

- NiMo (85/15 wt%) coating is non-depolarizing
- Tests of in house produced guides with a layer thickness < 1000 nm have shown a highly non- magnetic and non magnetizable behavior for tests with a magnetic field of 30 mT [106].
- The coatings do not show excess noise or thermally induced currents on the level of 1 pT [107].

The UCNs are transported from the source in guides with an inner diameter of 115 mm, as described in section3.1, to the nEDM setup. The feeding guide system for the nEDM setup is also made of glass tubes coated with NiMo (85/15 wt%) but with an inner diameter of 80 mm. It is planned to use a beam splitter for dividing the beam into two parts for the spectrometer chambers as junction between both diameters used. The coatings are performed as described in section 3.1. Characterization measurements at PF2/ UCN at the ILL showed for the tested guides a transmission value of 96.3 $\pm$ 1.2 %/m, which was also shown by the measurements in [93], which were performed as described in section3.2.

4.2 Beam Splitters

For different locations in the experiment beam splitters (BS) with a high transmission are required. To fullfill this demand the losses due to slits of this neutron optical device have to be minimized because they are the main loss issues. Another demand on all developed devices is a high modularity to enable upgrades or repairs with a small effort as possible. An additional requirement is the compactness and manageability of the components. Taking all this into account the beam splitters were made of NiMo (85/15 wt%) coated glass guides with an inner diameter of 80 mm.
For first tests a beam splitter with an opening angle of 60° between the dividing legs was manufactured, shown in Fig. 4.1(b). For the simultaneous spin detection (see section 5.6.1) a beam splitter with an opening angle of 120° with a 30° chicane on each dividing leg was designed 4.1(a). The symmetric division of the beam splitters was tested by measuring the transmission through both splitters was measured. For

(a) Beam splitter No. 1 (BS No.1) with an opening angle of 120° with a 30° chicane for the simultaneous spin detection part

(b) Beam splitter No. 2 (BS No.2) with an opening angle of 60° between the dividing legs of the beam splitter

Figure 4.1: Different beam splitter designs for the nEDM experiment in Y arrangement.

the later experiment a division of the neutron beam of nearly 50 % is required.

4.2.1 Characterization Measurements of the Beam Splitters

Measurements were performed at the ILL PF2-UCN beam line in Grenoble. Therefore the linear chopper system, designed and described by the author of [42], was used. Next, a measurement was performed with the beam splitter and a flight path of 1 m glass guide attached and one without the beam splitter only with the 1 m glass guide. One leg of the beam splitter was closed with an aluminum window, on the other leg A a Cascade U detector was installed. The same measurement was performed to get the transmission through the second leg B. The results are shown in Tab. 4.1 and with

$$A_{sp} = \frac{(N_A - N_B)}{N_A + N_B} \tag{4.1}$$

the asymmetry between both legs can be estimated.
To determine the transmission T a measurement without the beam splitters was carried out, using:

$$T_{BS} = \frac{N_{BS}}{N_{ref}} \tag{4.2}$$

Results are shown in Tab. 4.1.
The transmission through BS No. 1 is 53.1 ± 0.3 % and the asymmetry amounts to −0.33 ± 0.15 % for UCNs with a velocity between 3.3 and 6 m/s. This BS was constructed for the simultaneous spin detection, so it was constructed for a high

transmission between the two legs to enable the polarized UCNs of high probability to reach the right side to get analyzed and detected, which will be further discussed in section 5.6.
For the second BS No. 2 an asymmetry of $-0.19 \pm 0.10\,\%$ was measured for the same velocity range. The transmission for BS No. 2 being $82.6 \pm 0.4\,\%$ much higher than for BS No. 1. This is owing to the different angles of the beam splitters and the chicane in BS No. 1. However, both measurements showed that the legs for the beam splitters performed nearly symmetrical.

	Count rate BS No.1 [1/s]	Count rate BS No.2 [1/s]
leg 1	51.3 ± 0.1	79.7 ± 0.1
leg 2	50.9 ± 0.1	79.4 ± 0.1
asymmetry [%]	-0.33 ± 0.15	-0.19 ± 0.10
transmission [%]	53.1 ± 0.3	82.6 ± 0.4

Table 4.1: Result for the beam splitter characterization measurements for the velocity range between 3.3 and 6 m/s. The errors arise from Poison statistics and error propagation.

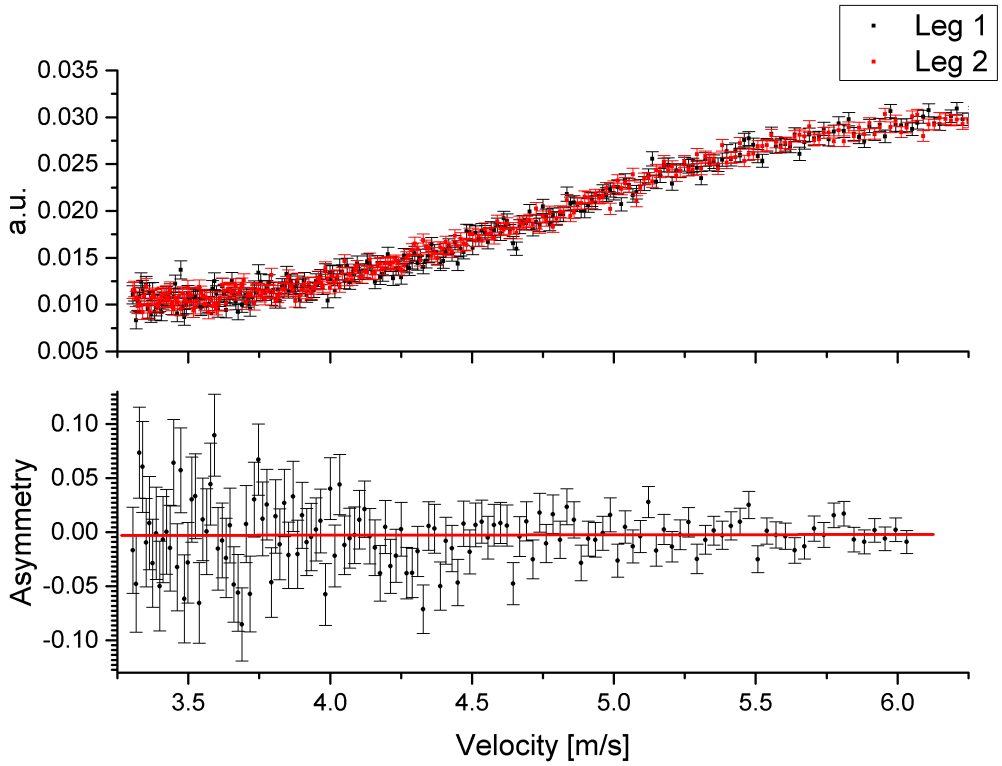

Figure 4.2: Transmission asymmetry for BS No.1 in dependence of the UCN velocity. The red line in the lower plot represents the mean asymmetry of $-0.33 \pm 0.15\,\%$. In the upper plot the error bars arise from Poison statistics and in the lower the propagation of the errors was done with Gaussian error propagation.

4.3 Switch

For delivering UCN to different parts of the nEDM setup two three way switches are required, for each spectrometer chamber respectively one. The first direction is to fill the spectrometer chamber with UCNs from the source, the second for guiding the UCN through a 90° bend to the detector after storage in the spectrometer chamber and the third way is from the UCN source direct to the detector for monitoring.

4.3.1 Construction of the Switch

The complete switch system including the linear stage DC motor is in a vacuum housing made of aluminum (Fig. 4.3(a)). During vacuum tests the system reached a vacuum of 10^{-6} mbar.

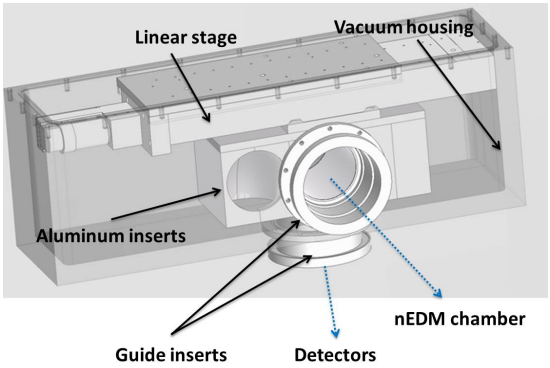

(a) Sectional illustration of the switch. The front side of the aluminum housing is faded out. The aluminum inserts are mounted on an assembling plate which is screwed to the linear stage. The blue arrows indicate the direction of the neutron flight path.

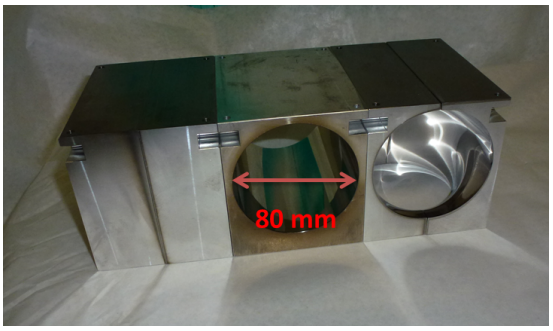

(b) Polished aluminum inserts of the switch with an diameter of 80 mm, and coated with 500 nm NiMo. The 90° bends are made of half shells and the straight part is made of one part.

Figure 4.3: Sectional illustration (a) and picture (b) of the insert of the nEDM UCN switch.

Since all components get in contact with polarized UCN in the setup, also these parts of the switch has to be non magnetic to avoid depolarization. Fig. 4.3 (b) the picture shows the insert of the switch. The curved parts are made of aluminum half shells covered with a NiMo (85/15 wt%) layer on the inside, where the parts get in contact with the neutrons. In Fig. 4.3 these half shells are placed on the right and the left side. The straight through part (in Fig. 4.3 in the middle) is made of one piece prepared in the same way as the curved parts. These neutron guide sections are mounted on an assembling plate and screwed on a linear stage M-4143PD with a C-863 Mercury Step Controller from PI [108] made of aluminum (see Fig. 4.3 (a)). The maximum travel distance is 300 mm. Assembling the insert part to the neutron guides in the appropriate height, the complete linear stage is height adjustable. The inserts for assembling the neutron guides to the switch (see Fig. 4.3 (a)) are flexible in order to minimize the gap between neutron guide and insert part of the switch.

4.3.2 Characterization of the Switch with UCNs

In first tests the reliability of complete system under vacuum conditions is checked without neutrons. After the switch passed this tests it is characterized at the ILL PF2-UCN beam line in Grenoble. For the transmission measurement a velocity

selector[1] was used. Neutrons, coming from the neutron turbine, are transported through a 1 m electropolished stainless steel guide to the velocity selector (Fig. 4.4). Behind the velocity selector the neutrons are guided one meter higher to shift the neutron spectrum and thus getting higher neutron intensities. After this a transition flange from stainless steel with an inner diameter of 78 mm to glass guides with 80 mm was installed. Next, a 500 mm glass guide is installed followed by a Cascade detector [99]. In this configuration the reference measurement is performed. The switch was placed in the beam line between the glass guide and the detector. Between a 300 mm long glass guide is used (Fig. B.1) to direct the neutrons from the switch to the detector.

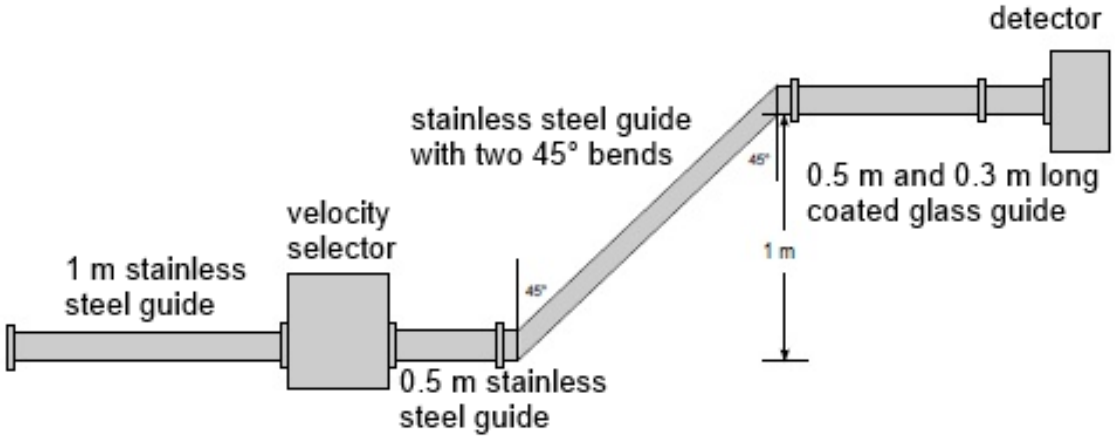

Figure 4.4: Illustration of the characterization setup for the switch used at the ILL PF2-UCN beam line. The glass guides are coated with 500 nm NiMo (85/15 wt%). For testing the switch, it was mounted between the glass UCN guides.

The results for the 90° switch position and the straight through position is shown in Fig. 4.5. It shows a mean transmission in the velocity region of $5 - 7$ m/s of 90 ± 1 % for the straight through position and 80 ± 2 % for the 90° positions. These results satisfy the requirements for the nEDM. Nevertheless it is planned to manufacture the 90° switch parts of one piece to reduce slits and increase the UCN transmission.

[1] lend from Dr. Ullrich Schmidt, Universität Heidelberg

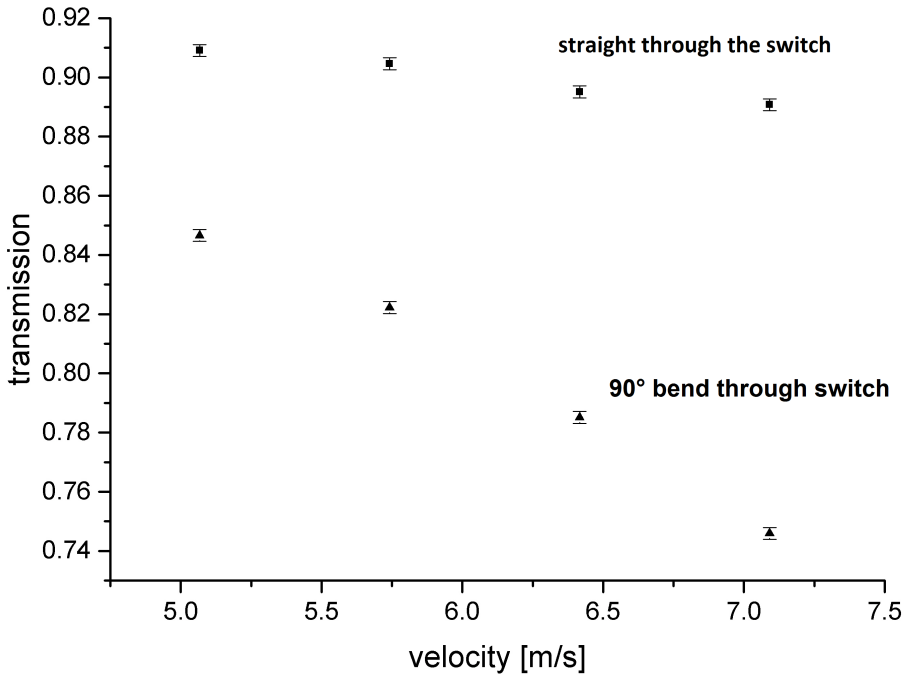

Figure 4.5: Results of the results of the transmission measurements. The squares represent the results for the flight path straight through the switch and the triangular symbols are for one of the 90° bends.The error bars arise from Poison statistics.

4.4 Bend Sections

Different bend sections for the nEDM setup made of glass were build and tested with neutrons as part of this thesis. The main goal is to get an optimal UCN transmission. To reach this, the bend sections were constructed as described in section 3.1 for the guiding system from the UCN source to the nEDM setup. The bends only differ in the diameter from those described in section 3.1. They have an inner diameter of 80 mm. The bends are made of polygon sections with an angle of $7.5° \pm 0.5°$. The angle varies by means of the cutting process produced externally. They have to be chosen in dependence of the total angle, which is required for the special application. Here the total bend has an angle of 45 °. The preparation, coating and the gluing process is described in section 3.1.
The bend has an outer radius of 575 mm and a flight length of 680 mm made of four sections. The two side pieces are at the outside 200 mm long and the middle pieces 150 mm.

4.4.1 Characterization of the Bend Sections with UCN

The characterization is done with the same system as it is described in section4.2. The results are shown in Tab. 4.2. The transmission values are divided in velocity regions. The most interesting one is the region of $6 - 3.3\,\mathrm{m/s}$ with an transmission of (79.4 ± 0.2) %. Comparing this with an electropolished stainless steel 45° bend section, usually used for UCN experiments, the transmission is about 15 % higher [109].

velocity region	$10-8$ m/s	$8-6$ m/s	$6-3.3$ m/s
transmission[%]	67.7 ± 0.1	71.3 ± 0.1	79.4 ± 0.2

Table 4.2: Transmission for a 45° bend sections.The errors arise from Poison statistics and error propagation.

4.5 Precession Chamber

The precession chambers for the Munich nEDM will be a double chamber arrangement as already described in section 2. For storage experiments materials with a high Fermi potential and a relatively low absorption cross section have to be chosen. Before hand, beryllium (252 neV) and BeO (261 neV) [21] were frequently used for coating storage vessels. However, beryllium has the disadvantage of being a highly toxic and because of this fact the coated surfaces are complicated to produce and to handle. To circumvent these problems other materials were investigated, like Diamond-Like Carbon (DLC) for coating the electrodes. The Fermi potential of DLC depends on the sp^3 fraction in the coated layer. The higher the sp^3 fraction the higher the Fermi potential. It varies between 195 neV and 305 neV [110]. Other UCN storage properties were investigated by several groups [111], [110], [112], [113]. This well characterized material is now under usage in several experiments all over the world and replaced beryllium coatings for the electrodes in most of the nEDM projects.
For the insulator ring quartz or glass ceramics are commonly used [13], [73]. In most experiments a covering layer of an insulating material with a higher Fermi potential than quartz with 90 neV is coated on the surface getting in contact with the UCN. In many experiments BeO was used. Due to problems with this material new materials were investigated to replace BeO by an equivalent material. At the PSI a polystyrene

(PS) ring coated with deuterated PS with an Fermi potential of 161 neV [114] is used for the insulator ring PSI [115].
In [114], [116] and [117] also deuterated PolyEthylene (dPE) was investigated on its suitability for a coating in the precession chamber. The Fermi potential is 215 neV [116] and also other investigated properties are promising. The storage time for UCNs in a glass guides, coated with dPE was about 60 s. The loss coefficient η was calculated to be $1.3 \pm 0.3 \cdot 10^{-4}$. With this result a free precession time for the future Munich nEDM of 125 s to 250 s is within the realms of possibility [116].
For the Munich nEDM project both chambers are constructed in the same way. For the electrodes a NiMo (85/15 wt%) coating is planned. The insulator in between itself should be a quartz ring coated with dPE.

4.6 Conclusions of the Neutron Handling System for nEDM

All UCN guides for the future nEDM experiment have an outer diameter of 90 mm with a wall thickness of 5 mm and are coated 500 nm with NiMo (85/15 wt%). The here tested bend sections are composed of polygon sections with an angle of $7.5° \pm 0.5°$ and for a 45° in a velocity region of $6 - 3.3$ m/s a transmission of 79.4 ± 0.2 % was measured.
For the straight guides a transmission of 96.3 ± 1.2 %/m was measured.
The switch showed in the characterization measurement a transmission for the velocity region of $5 - 7$ m/s of 90 ± 1% for the straight through position and 80 ± 2 % for the 90°.
The beam splitters had a transmission of 53.1 $\pm$ 0.3 % for BS No. 1 and for BS No. 2 82.6 $\pm$ 0.4% for the velocity range of $6 - 3.3$ m/s. The asymmetry is calculated to -0.33 $\pm$ 0.15 % for BS No. 1 and for BS No. 2 to -0.19 $\pm$ 0.10 %. All these results of the measurements are necessary to determine the UCN transport losses for the future nEDM setup.

Chapter 5

Spin Manipulation System for nEDM

The future spin manipulation system for the nEDM consists of a superconducting magnet for manipulating the spectrum of the neutrons in the spectrometer chamber in dependence of the spin. The guiding fields are made of Helmholtz or solenoid coils, depending on the operating place. For the magnetization of the polarizer foils permanent magnets are used. The planned system for the spin analysis for the nEDM is based on detecting both spin components at the same time. In the following sections a detailed description of all developments in the subsystems will be given.

5.1 Manipulation of the UCN Spectrum

In order to manipulate the UCN spectrum filled in a spectrometer chamber, a combined system of a superconducting magnet and a fast adiabatic spin flipper arrangement is planned, as it is shown in [118] and [119]. With this device it is also possible to investigate velocity dependent systematic effects.
The functional principal is shown in Fig. 5.2. Here, one spin component is accelerated and the other one is decelerated. This effect can be scaled with the strength of the magnetic field of the superconducting magnet. It is also possible to increase the magnetic field in a way that one spin component is repulsed by the field and the other one can pass. With such a so called polarizer magnet 100 % polarization can be achieved.
For the Munich nEDM both spin components are filled into the storage chamber, where the accelerated spin component is cleaned out over time. To reach this a superconducting magnet with a magnetic field of 1.5 T is needed, for the used magnet the maximum field is 3 T. A photo of the delivered magnet is shown in Fig. 5.1 For cooling the cryostat liquid Helium is used with a closed cycle refrigerator. The magnet has a warm bore with a diameter of 200 mm to insert the UCN guide and

Figure 5.1: Photo of the superconducting magnet after delivery in December 2015.

the fast adiabatic spin flipper. The length is 1.285 m with a homogeneity inside the magnet of 10 ppm in a volume of 120 mm diameter and a length of 100 mm. The stray field is 0.1 mT in a distance of 2 m. In Appendix F the by Oxford Instruments measured specifications of the magnet are shown. The spin flipper will work at a frequency of 40 MHz. However, for different reasons the delivery of the magnet was delayed and this part of the spin manipulation system unfortunately could not be finished and tested within this thesis.

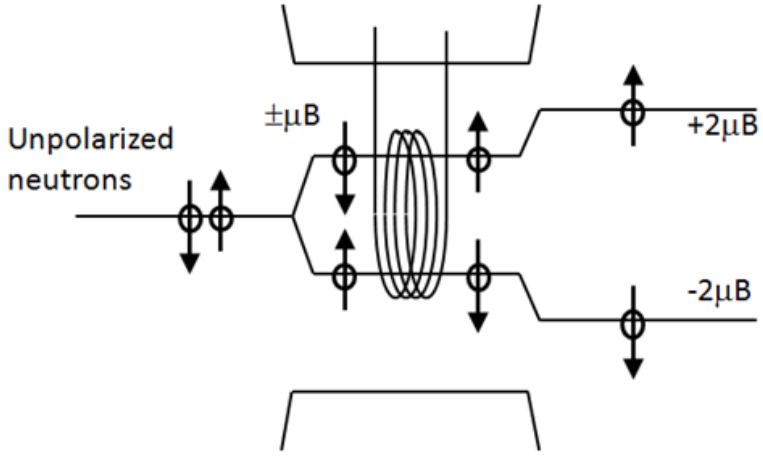

Figure 5.2: Illustration of the functional principle of the UCN spectrum manipulator. Here, unpolarized UCN entering from the left side the magnet, are split in dependence of the spin orientation and magnetic field strength in two energy levels by the Zeeman effect. A spin flipper located in the magnetic field changes the spin orientation by 180° and the energy shift. When UCNs leave the magnet, it causes a repeated acceleration for one component and a deceleration for the other component. Taken from [120]

5.2 Polarizer Development

For the nEDM measurement a high polarization is indispensable. The influence on the sensitivity via α on each measurement can be diagnosed from Equation 2.4. For the future nEDM measurement foils are necessary for the spin analyzing system, as will be described in section 5.6.
For UCNs it is best to polarize them by transmission through a thin magnetically saturated foil. In previous experiments [121] polarizations of (95 ± 2) % were achieved. For one spin state the potential is low due to the saturation flux the Zeeman shift in the foil and it can pass with low losses. The other state is reflected, because of the UCN energy is lower than the potential.
Typical polarizers are made of a 300 nm iron layer coated on a silicon waver or a thin aluminum foil. Polarizations better than 95 % can be achieved. Because in UCN experiments they are used in transmission mode, the choice for a polarizer substrate is limited by several factors: The material has to have a low neutron optical potential, a low absorption cross section and has to be thin. There is also the possibility to use multilayer polarizers made of iron and silicon, like it is done for cold neutrons. The advantage for such a multilayer polarizer is that also faster neutrons can be polarized and with UCN polarizations of nearly 100 % are possible. For the measurements in

this thesis both kinds of polarizers were produced on aluminum foils with a thickness of 0.1 mm and silicon wafers with a magnetron sputtering facility and both tested at the ILL.

5.3 Broadband Adiabatic Spin Flipper

For different applications several spin flipper coils as shown exemplary in Fig. 5.3 with different windings and length were build as part of this thesis. Therefore, a supporting structure made of a plexiglass tube was utilize. On this supporting structure with different length, spin flippers are winded with a copper wire with a diameter of 1 mm. Spin flippers with 20 (10 cm length), 30 (15 cm length), 60 (20 cm length) and 80 (25 cm length) windings were build, as it is shown for example in Fig. 5.3. The inductance for these coils were measured to 70 μH for the coils with 20 windings, to 90 μH for 30 windings, 250 μH for 60 windings and 350 μH for 80 windings.

Figure 5.3: Picture of a broadband adiabatic spin flipper for the future nEDM setup with an inner diameter of 100 mm and a length of 110 mm with 30 windings of a 1 mm copper wire.

To provide the spin flipper coils with a high frequency (HF) a function generator and an amplifier is needed. To verify the amplitude and the frequency of the HF also a current probe is needed. On the amplifier the demands are, that it should work linear and current stable and provide the spin flipper coil with a small ohmic resistance with a HF and an adequate current. The needed frequency band for a stable amplification was between 10 kHz and 200 kHz. For this purpose an

operational amplifier from Servowatt DCP 130/60 [122] is used. As a functional generator an Agilent Keysight 33210A [123] is used.

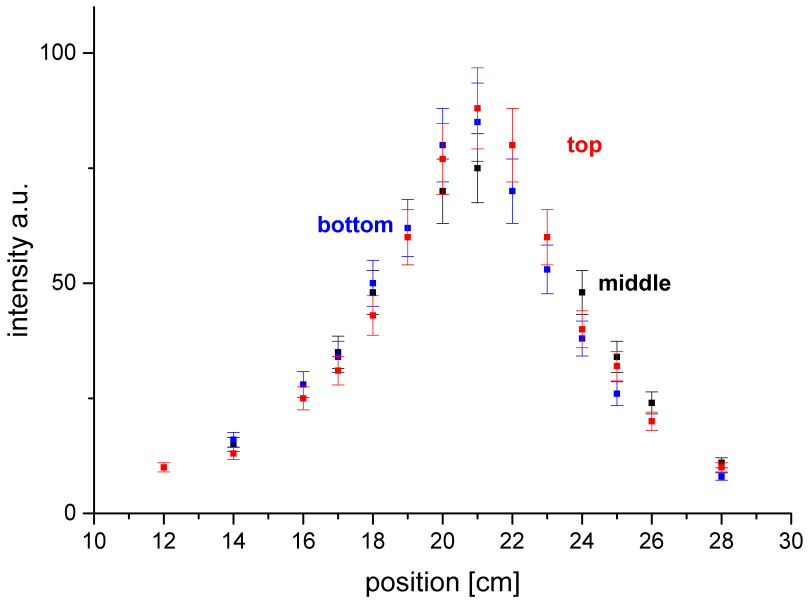

Figure 5.4: Measurements of the trend of the magnetic field in a spin flipper with an inner diameter of 100 mm and a length of 110 mm with 30 windings for a frequency of 70 kHz and a current of 600 mA and for three different positions. The errors are following from measurement uncertainties from positioning the pick up coil and from Poison statistics. The different colors are representing the measurement heights in the UCN guide. The parameter on the x axis is the position of the pick up coil parallel to the neutron flight path.

To map the field inside a neutron guide with a 30 winding spin flipper, shown in Fig. 5.3, a measurement with a pickup coil was performed for a frequency of 70 kHz and a coil current of 600 mA. The results are shown in Fig. 5.4. Considering the error bars in Fig. 5.4 the HF magnetic field is for different positions identical in the magnitude, independent from the position in the guide. Also measurements for the left and the right side were performed and yields the same result (not shown in Fig. 5.4).
Further measurements were performed with a constant current to measure the magnetic field trend for the flippers and the magnitude of the field because in future experiments only the coil current will be monitored. Fig. 5.5 shows the result for

such a calibration of a measured current and the magnetic field in the spin flipper. Such a calibration curve was measured for each spin flipper coil and shows the dependence of the magnitude of the magnetic field in dependence of the position of in the spin flipper coil.

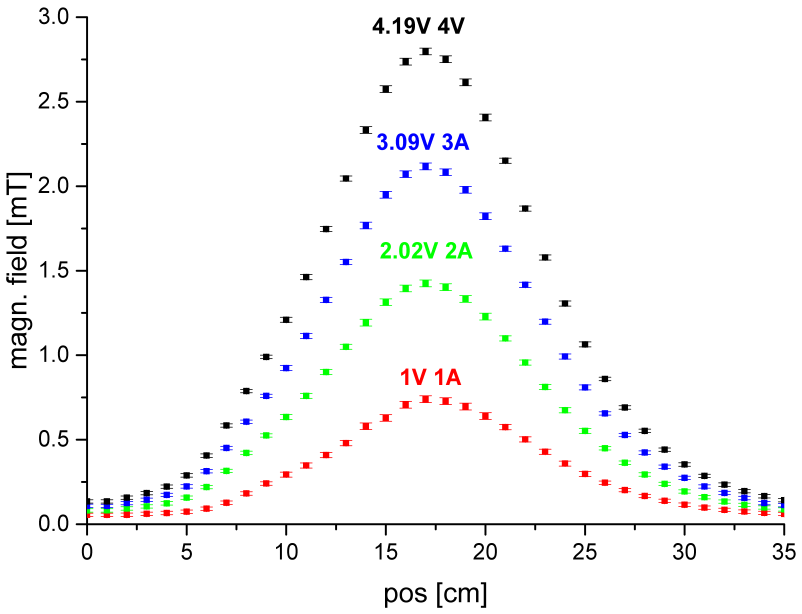

Figure 5.5: Result of a characteristic calibration measurement of the magnetic field for a spin flipper with an inner diameter of 100 mm and a length of 25 cm with 80 windings in dependence of the current or applied voltage. The data sets for the different applied currents with the corresponding voltage are marked with different colors. The error bars arise from Poison statistics and measurement uncertainties.

5.4 Spin Guiding System

The concept for the spin guiding system based on rectangular Helmholtz coils combined with solenoid coils. The field strength of the guiding coils are in the range of 0.3 mT - 1 mT. To find the properties and the dimensions of the coils, especially for the critical parts like the guiding field for the simultaneous spin detection part, simulations are done with Comsol Multiphysics®. Those build coils are tested on their polarization conservation first time in 2013 at the ILL. Another goal of these tests was to examine the conservation of the adiabatic spin transport for a combination of

different coils and especially the adiabatic transport of the spin between coils with different field orientations. More details on the simulation of the coils can be found in the master thesis in [124].

5.5 Polarizer and Spin Flipper Characterization Measurements

For the characterization of the different spin flippers and polarizers a setup is build and its spin flip efficiency is considered. The UCN are guided through a NiMo (85/15 wt%) coated glass tube with an inner diameter of 80 mm to a linear chopper (Fig. 5.6). Behind the chopper a flight path of 2.1 m coated glass guides, interrupted by a polarizer wafer/foil holder (Fig. 5.6) and an analyzer wafer/foil holder (Fig. 5.6), is situated and especially build for this experiment. The polarizer foils were magnetized with permanent magnets on both sides with 10 mT. To preserve the polarization and to create a gradient magnetic field, one square and two rectangular Helmholtz coils were designed and winded (Fig. 5.6). This is shown in Appendix E Fig. E.1 taken during the beam time in 2013.

The spin flippers are placed in a region of the holding field with B approximately

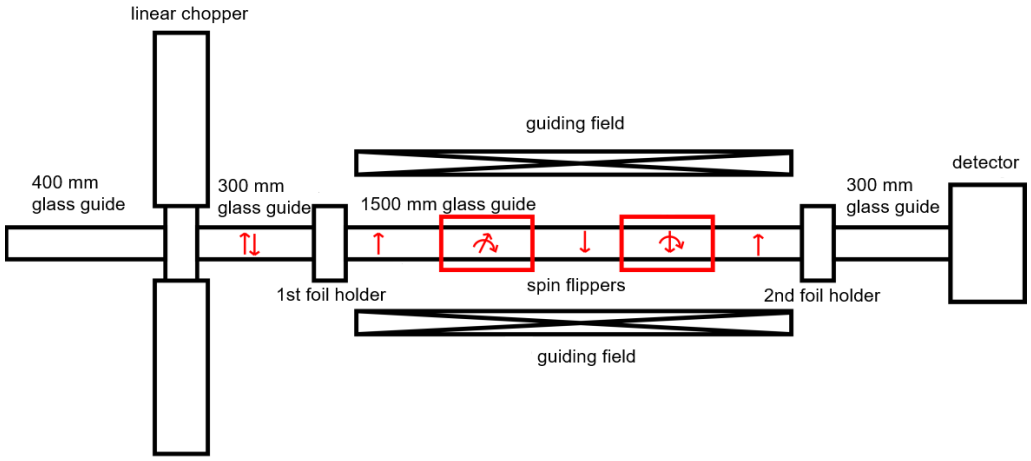

Figure 5.6: Illustration of the experimental setup for the characterization measurements. The UCNs coming from the turbine from the left hand side, are guided with a 1 m long stainless steel guide with an diameter of 70 mm through a transition adapter and 400 mm long glass tube. All glass guides in the setup are coated with 500 nm NiMo (85/15 wt%). The red arrows indicate the orientation of the incoming neutron spin and while its translation by the respective component.

0.7 mT and ∇B approximately $22\mu T/cm$. For the first tests a multilayer polarizer made of soft magnetic iron and silicon sputtered on a silicon waver are used as described in section 5.2.
First the transmission for UCN through the different polarizers is measured. Therefore, only one polarizer is inserted into the wafer/foil holder for the polarizator (Fig. 5.6) and the wafer holder for the analyzer (Fig. 5.6) was empty. With this configuration the results shown in Fig. 5.7 are measured. The following transmission measurements are performed:

- Reference measurement without any wafer
- For a wafer coated with a 300 nm iron layer
- For a 10 layer super polarizer made of iron and silicon. The layer structure is shown in Appendix D.1 Tab. D.1

At the wafer holder a magnetic field of 10 mT is applied to magnetize the polarizer and the chopper parameters are chosen that every 900 ms the beam is opened for 30 ms. The measured offset of the opening function is diagnosed to be 27 ms.
The results of both polarizers for neutrons with velocities between 3.5 m/s and 7.5 m/s reveal a similar performance. But for higher velocities the iron polarizer performance decreases and neutrons with the wrong spin orientation are able to pass, where the super polarizer is still polarizing up to a velocity of 9 m/s. For the future nEDM application a higher polarization power is a great advantage because the UCNs are accelerated on the way through the UCN guide system to the analyzer, because the spin analyzing system is mounted 1 m under the setup. By using the super polarizer an increase of the visibility is possible. For the velocity region of high polarization about 40 ± 2 % of the neutrons are able to pass. With this setup the absorption for the transmitted spin component is in the order of 10 %.

Before the different spin flippers are tested, they need to be tuned on the optimal working point. This was done by variation of the frequency keeping the current constant and via versa, for each spin flipper respectively. A typical value for the used current is 500 mA and for the frequency of 21 kHz. With this settings it is possible to measure the different counting rates for calculating the efficiencies for the spin flipper coils [58], [60]:

$$f_1 = \frac{(N_{11} - N_{10})}{(N_{00} - N_{01})} \quad f_2 = \frac{(N_{11} - N_{01})}{(N_{00} - N_{10})} \tag{5.1}$$

where f_1 and f_2 are the spin flip efficiency for the flippers to be characterized the different count rates N_{11}: SF1 on SF2 on, N_{10}: SF1 on SF2 off, N_{00}: SF1 off SF2

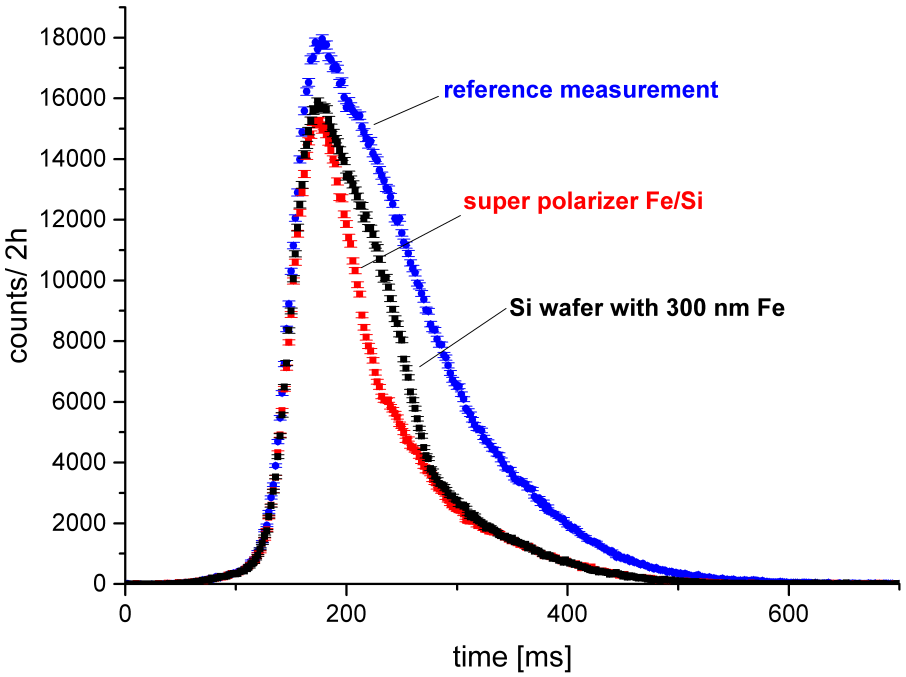

Figure 5.7: Results of different transmission measurements, with a measuring time of 2 hours. For the polarizers a magnetic holding field of 10 mT is applied. Blue markers indicate the result for the measurement without a wafer in the wafer holder. Black indicate results with a wafer with a 300 nm iron layer and red the use of an iron silicon multilayer polarizer. The error bars arise from Poison statistics.

off, N_{01}: SF1 off SF2 on. The results are shown in Tab. 5.1. All tested combinations yield high flipping efficiency.

Windings No.	Spin flipper 1, Efficiency [%]	Spin flipper 2, Efficiency [%]
20	$99.9\,^{+0.1}_{-0.8}$	99.0 ± 0.7
30	$99.6\,^{+0.4}_{-0.9}$	99.1 ± 0.8
60	98.6 ± 0.7	$99.7\,^{+0.3}_{-0.8}$

Table 5.1: Results for the spin flip efficiency measurement using different windings of the coils. The uncertainties arise from error propagation.

The 60 winding spin flipper 2 is chosen for tests with the different custom-build polarizer foils. The measurements for the polarizers build of multilayer of iron and

silicon coated on a silicon waver are tested and resulted in a polarization of 99.1 $^{+0.9}_{-2.5}$ % with a holding field of B = 10 mT at the foil holders. For a single iron layer 300 nm on an aluminum substrate with a holding field of B = 10 mT at the foil holders, a polarization of 96.2 +/- 2.5 % (Fig. 5.8) resulted.

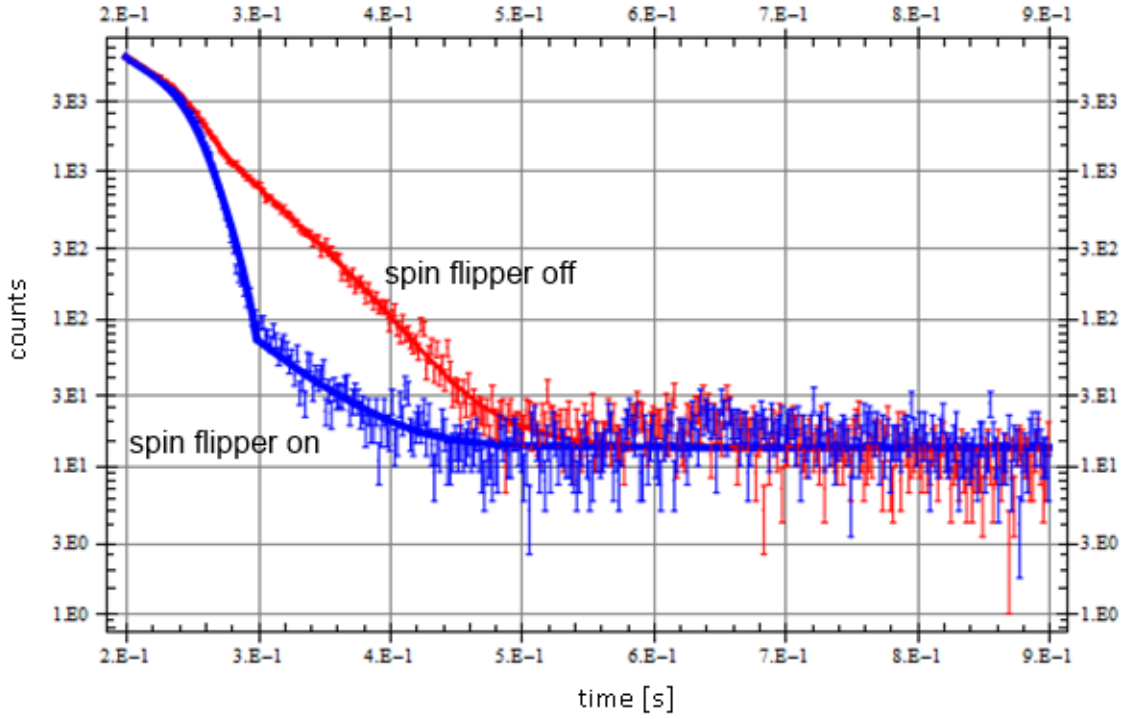

Figure 5.8: Results of a polarizer characterization measurement using a magnetic holding field of 10 mT. The figure shows in blue the result for the measurement with spin flipper on and in red with spin flipper off. The error bars arise from Poison statistics.

Additional depolarization tests were performed by replacing the last Helmholtz coil by a 50 cm solenoid as it is shown in Fig. 5.9. This test is the first step in answering a key question for the nEDM setup: Is it possible to guide the polarized UCN into the shielded room, passing several layers of μ- metal, without loosing any polarization?
The tests showed that the spin follows the magnetic field adiabatically and the polarization was diagnosed to be 99.3 $^{+0.7}_{-2.4}$ % with a holding field of B = 10 mT at the foil holders for the super polarizer made of iron and silicon. Comparing this with previous results for the super polarizer, it appears that the performance is similar and the spin follows the guiding fields as expected, what is also shown in Fig. 5.10. In Fig. 5.10 also the higher polarizing power of the super polarizer in comparision with a single iron layer can be seen by comparing the black curve representing the iron

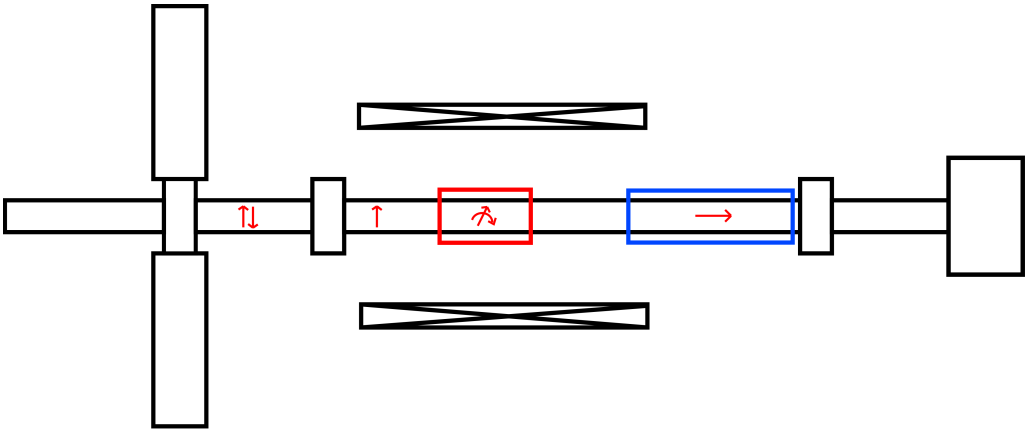

Figure 5.9: The technical drawing shows a slightly modified setup to the already in Fig. 5.6 in detail described one. The modification is the replacement of the last Helmholtz coil by a 50 cm long solenoid coil (here in blue) to investigate the adiabatic spin transport by performing a 90° spin rotation and back.

foil with the red curve representing the super polarizer. Additional measurements were performed using μ- metal plates around the guide will be presented in section 6.3.4.

Several further tests were performed to investigate the depolarization of UCN by external influences:

- A Helmholtz coil was reversed to generate a zero crossing region.
- One side of a Helmholtz coil was reversed to generate a zero crossing region for the UCNs.
- A permanent magnet was positioned on the UCN guide during a measurement.
- A zero crossing region short in front of the analyzer was created.

For all these attempts to depolarize the UCN no decline of the polarization was visible and from which the conclusion follows, that the spin guiding and manipulation parts are suitable for the nEDM project and can be implemented in the way they were tested.

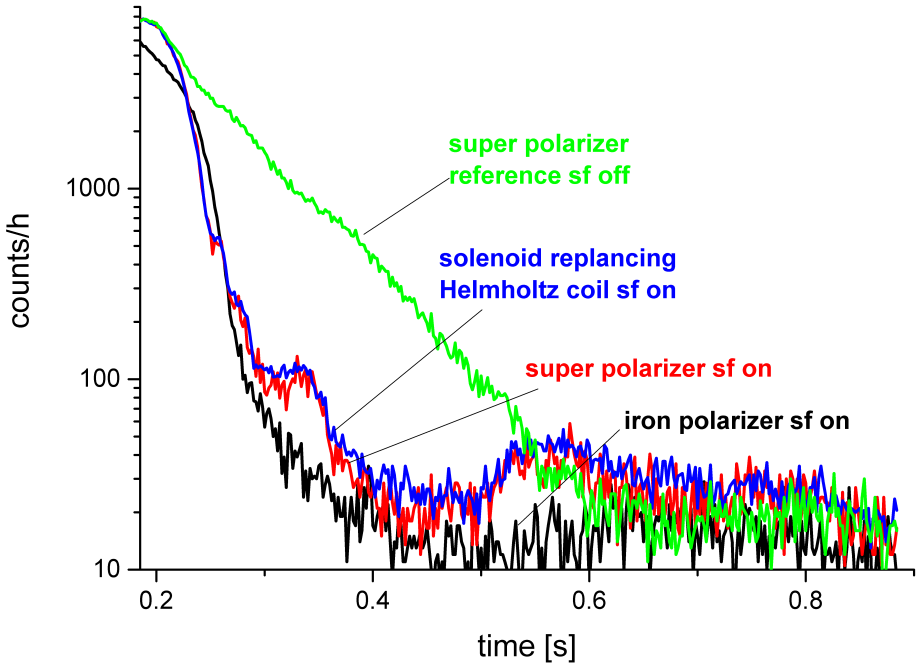

Figure 5.10: Results for a selection of the polarization measurements. In green a reference measurements with a super polarizer as polarizer and analyzer, the Helmholtz coils as guiding field and both spin flippers switched off. The corresponding measurement with a spin flipper on is shown in red. The blue curve is the result of a measurement with a solenoid coil replacing a Helmholtz coil in the guiding field and also one spin flipper is switched on. The black curve is the result for two iron foils used as analyzer and polarizer.

5.6 Simultaneous Spin Analyzing System

So far most of the current nEDM collaborations (e.g. by the RAL-SUSSEX-ILL [62]), used a sequential spin analyzing system. A schematic illustration is shown in Fig. 5.11 (a)). Here, the spin components are detected one after another by switching the spin flipper on and off. Using this method the remaining spin component is stored in the system, consisting of the guide system, the switch and the storage chamber. The effective neutron lifetime for this system is much smaller compared with the emptying time. So the statistic for the as second detected component is limited by this fact. Another UCN loss channel is the possibility of depolarization for these neutrons stored for the emptying time. Also both spin components in the

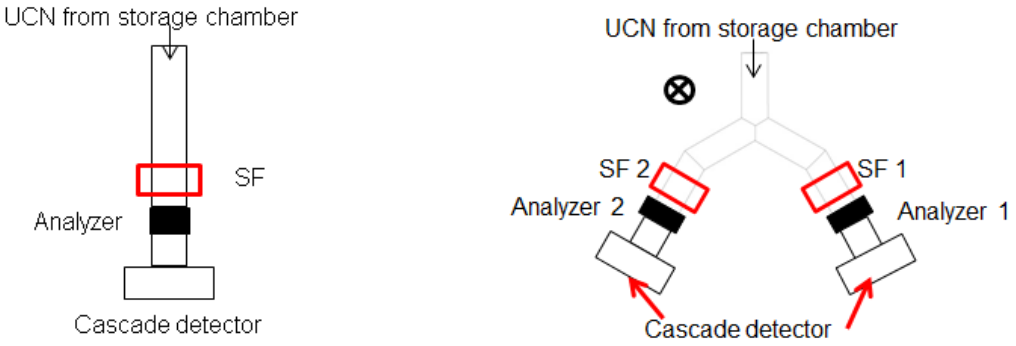

(a) Schematic illustration of the required components for a sequential spin detection system

(b) Schematic illustration of a simultaneous spin detection system

Figure 5.11: Different concepts for nEDM spin detection systems.

same cycle are treated in a different way. This asymmetric treatment can cause spurious systematic effects. For the RAL-SUSSEX nEDM measurement, build up at the PSI UCN source, all losses of the initially stored neutrons are estimated to be higher than 50 % [65]. Since the nEDM sensitivity scales with the square root of the amount of neutrons $\sqrt{N}$ (compare equation 2.4) it is desirable to decrease these losses. This way a more effective UCN analyzing system would directly increase the sensitivity for each nEDM run. With such a system visibilities of $\alpha = 0.596$ were reached in previous studies [65].
The visibility is defined as following:

$$\alpha = \frac{(N_A - N_B)}{N_A + N_B} \tag{5.2}$$

where N_A and N_B are the count rate for the different spin components in the detector.
This considerations lead to the idea to use a simultaneous spin analysis system for a next generation nEDM. This idea was also implemented in the next generation nEDM project at the PSI. A detailed description and characterization of this apparatus is given in [125] and [65] and a first version of such a system and the usage in a nEDM experiment was done at LNPI in 1981 [72]. Therefore a beam splitter, as already described in section4.2, is installed in the emptying arm of the EDM apparatus and is shown in 5.11 b). In each arm an analyzer foil is located in front of the detector for detecting both spin orientations at the same time without the mentioned drawbacks due to the storage of one spin component above the analyzer. In this thesis a highly modular simultaneous spin analyzing system is constructed and characterized in section 5.6.1 and 6. Beside the modularity of the setup the

main requirements on the system are a low depolarization, high UCN transmission especially between the two arms with the analyzers, a high spin analyzing power, and additionally a high visibility α.

5.6.1 Spin Detection System

With a setup consisting of a beam splitter with an opening angle of 60°, two spin flippers, two foil/wafer holders and only one detector, first only short successful feasibility studies for the Munich spin detection concept were performed at the ILL in 2013.

Together with the measurements presented in section 5.5 a simultaneous spin detection system was planned, build and finally tested in a beam time in 2014 at the ILL as part of a mockup nEDM setup to characterize all developed UCN optical components and spin manipulation system and will be presented in section 6. Here, only the measurements linked to the characterization of the simultaneous spin detection system are treated. The UCNs enter the setup from top and are divided by the beam splitter (Fig. 5.12). For both arms the transmission for UCNs is similar. They pass on both sides a spin flipper with a copper housing (Fig. 5.12) and the analyzer foils and are guided by a 300 mm long NiMo coated glass guide to a Cascade detector. Further results will be presented and discussed in section 6.
With the knowledge acquired in the measurements presented in section 5.5 a guiding field, composed of rectangular Helmholtz coils for the future nEDM simultaneous spin detection system is manufactured. The dimensions of the coils are adapted to the neutron guides and operated with a magnetic field of 0.4 -2.4 mT. In the middle of the beam splitter a pentagon Helmholtz coil (Fig. 5.12) is installed. Otherwise in all outgoing directions a rectangular Helmholtz coil is installed (Fig. 5.12). The spin flippers for each arm of the beam splitter is installed in a region of a gradient field generated by the Helmholtz coils and the stray field of the magnets for polarizing the analyzers.

The magnetic field gradient across the simultaneous spin detection setup was measured and is shown for the middle of the neutron guide in figure 5.13. The spin flippers of a length of 100 mm and a total length of 110 mm with 30 windings were in the position at 7 cm behind the waver and ended at the position of 17 cm. The spin flippers were covered with an 1 mm thick copper shield to prevent crosstalk of both arms. Measurements on this topics with a pickup coil showed no influences of the two arms on each other. As analyzer two super polarizers coated on

a silicon wafer, tested within the measurements presented in section 5.5, are applied.

In order to characterize the system it is necessary to find the working point of the spin flippers. Therefore, the frequency and the current of the spin flippers was varied until the count rate for the detector was minimal. The results of the measurements are shown in Fig. 5.14. Here the frequency is tuned and the current is kept constant. For each measurement also the counts of the respective other detector is measured, in order to check for possible crosstalk of the arms (see Fig. 5.14). This measurements also show that the two spin flippers have different working points for frequency and current as displayed in Tab. 5.2. This could be caused by the performance of the

	Frequency [kHz]	Current [A]
Spin flipper 1	72.0 ± 0.1	4.5 ± 0.2
Spin flipper 2	80.0 ± 0.1	5.8 ± 0.2

Table 5.2: Result of the spin flipper characterization measurements showing the selected working points for the simultaneous spin detection system.

used amplifiers and the position of the spin flipper in the guiding field. However, these differences have no negative influence on the the spin flip efficiency. The count rates for both spin flippers change from approximately 1000 counts/ms with spin flipper of to approximately 130 counts/ms. All measurements were performed in the direct measurement mode configuration, as will be described in detail in section 6.1. In this configuration the switch is in the direct emptying position, meaning the complete incoming UCN spectrum is guided to the detectors and also neutrons with too high energies which were not polarized. These neutrons are the dominant factor of the remaining count rates in this characterization measurement. Therefore a visibility for the simultaneous spin detection system without storing the neutrons is calculated to be $\approx 78\,\%$ (see Tab. 5.3). In measurements reported in [126] a visibility of $63.4 \pm 1.8\,\%$ was reached in the PSI nEDM experiment. This is compared with a sequential spin analysis of $59.7 \pm 2.2\,\%$ an improvement. However, a visibility of bigger than $\approx 78\,\%$ is a great improvement of the sensitivity for a nEDM experiment. All further results with stored UCNs for the visibility α will be presented in section 6.3.3.

	arm 1	arm 2
visibility α [%]	77.3 ± 2.8	78.5 ± 3.1

Table 5.3: Result for the visibility in direct measuring mode.

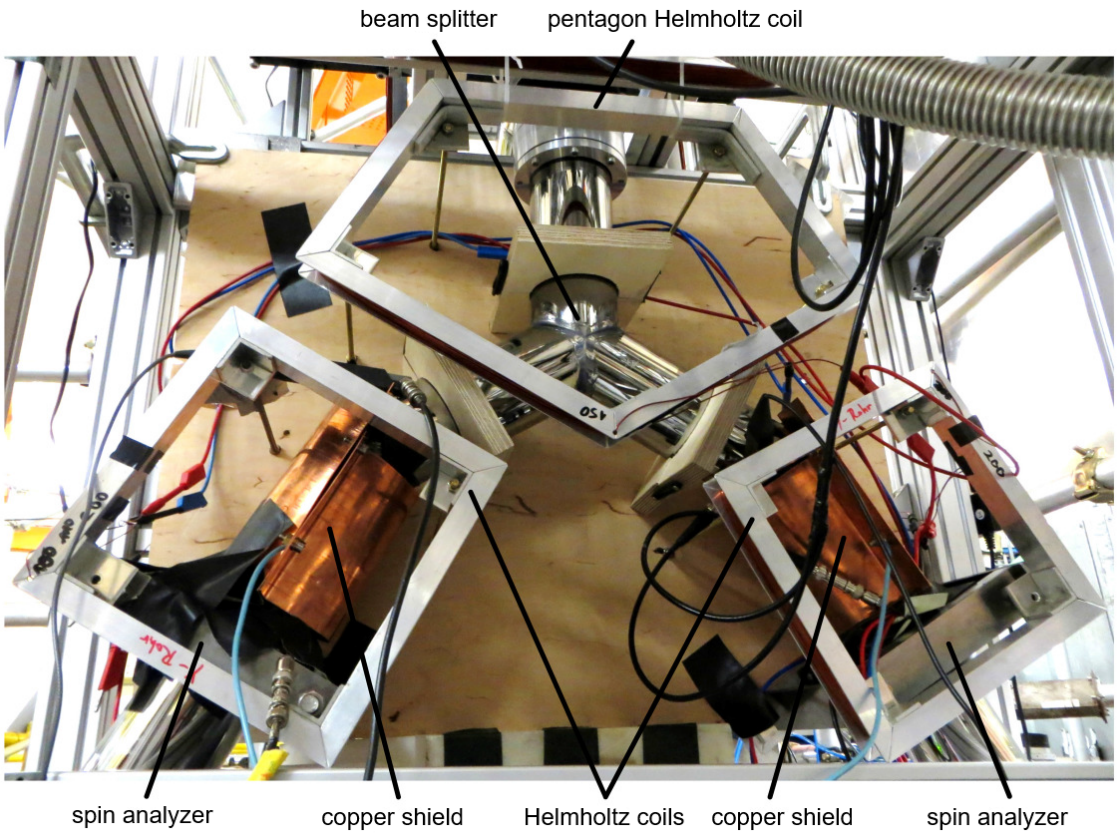

Figure 5.12: Picture of the simultaneous spin detection system already istalled in the nEDM mockup setup (see section 6). UCN coming from the top through an UCN guide are divided by the beam splitter. The complete setup is in a magnetic holding field generated by a pentagon Helmholtz coil and two quadratic Helmholtz coils. Half of the coils (not shown) are installed behind the non magnetic supporting structure. The divided neutron beam is then guided to the analyzers, passing respectively a spin flipper with a copper housing to prevent crosstalk. Taken from [124]

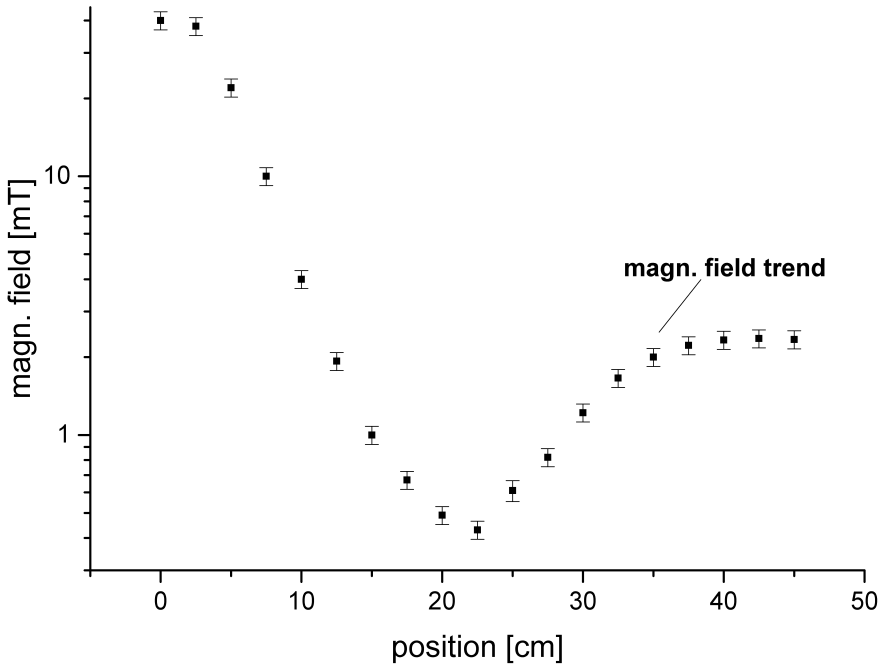

Figure 5.13: Magnetic field trend for the left arm of the simultaneous spin detection setup. The position 0 cm is in the middle of the wafer/foil holder with installed permanent magnets and ends in the middle of the pentagon Helmholtz coil (Fig. 5.12). The error bars arise from Poison statistics.

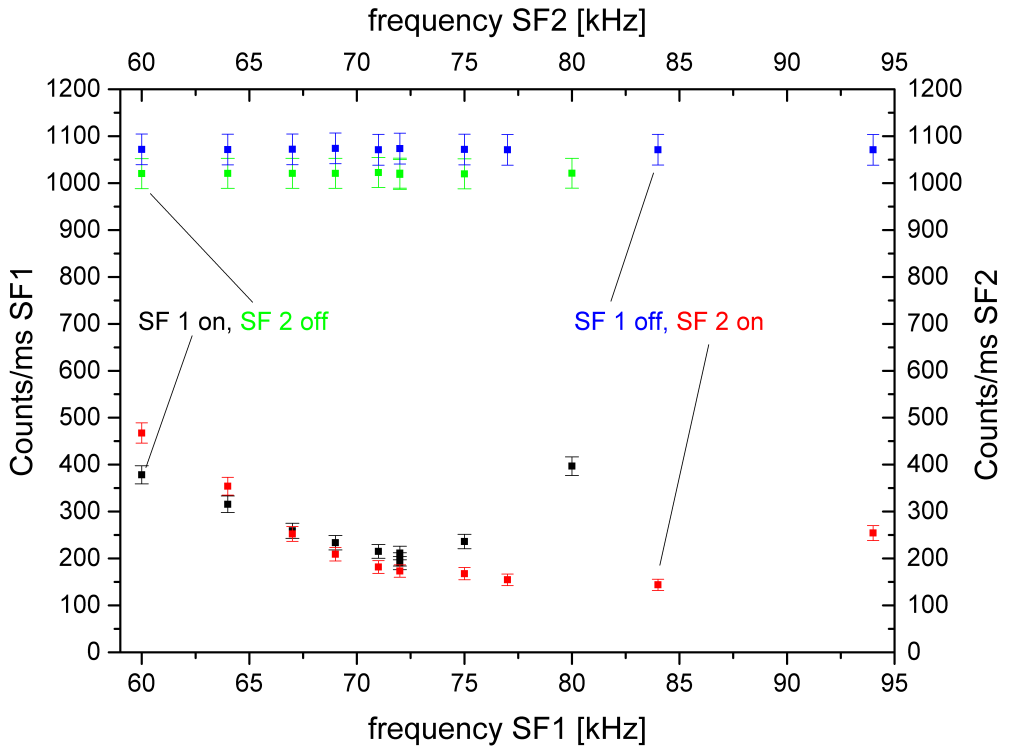

Figure 5.14: Result of tuning the frequency with constant current. Red markers indicate measurements for spin flipper 2 and the black markers the spin flipper 1. While the measurements were performed the respective spin flipper was on, the other arm was switched off. The corresponding measurement to the red one is shown in blue and for the black one in green.The error bars arise from Poison statistics.

5.7 Conclusions of the Spin Manipulation System for nEDM

The presented super polarizers, developed for the future nEDM, showed during the characterization measurement a polarizing power of over 99 %. For a single iron layer a value of 96 % was diagnosed. Compared with the polarization of 90 % achieved for iron foils as in studies such as [65] for the PSI nEDM experiment, this is a notable improvement because the polarization power influences directly the visibility and thus the sensitivity of the nEDM.
All manufactured and characterized spin flippers show an efficiency of over 99 % for rotating the spin. Measurements with the spin flippers installed in the simultaneous spin detection system, which are covered with a 1 mm copper shielding showed no influence on the non-active arm. The guiding field coils were designed, build and characterized and achieved the requirements.
The simultaneous spin analyzing system is successfully aligned in combination with the beam splitter described in section 4.2.1 with the guiding field made of rectangular Helmholtz coils. With a well tuned setup, and in direct measurement mode an asymmetry between the arms of about 78 % was measured. This is especially a promising result for the visibility determination (section 6.3.3), because for this measurement all neutrons reaching the detectors came direct from the UCN source and were not stored before. Compared with the simultaneous analyzing system presented in [126] with a visibility of 63.4 ± 1.8 % installed in the current PSI nEDM experiment, the concept based on super polarizers enables a much better spin analyzing power and visibility for nEDM experiments. All together for the simultaneous spin analyzing system installed under the mock up nEDM setup an improved value for the visibility is estimated.

Chapter 6

nEDM Test Setup Measurements

For a realistic test of all components needed for the Munich nEDM experiment a measurement was performed at the ILL PF2-UCN beam line in Grenoble. The intention of the measurement was to run all components together, described in the Chapters 4 and 5 under data taking conditions and to identify possible problems. The main issues of the measurements are:

- Commissioning of the switch and the plug shutter:
  The UCN switch was successfully tested in 2013 (section 4.3). The performance in combination with the nEDM test setup will be tested and a long term test of the mechanic parts. In order to fill the storage chamber from the side without loosing to much phase space, a special plug shutter was realized, which additionally should decrease geometric phase effects at the edges. The shutter so far was never tested, hence the functionality of this mechanism was in the focus of the tests.
- Commissioning and investigation of a simultaneous spin detection system:
  In order to increase the sensitivity of the Munich nEDM setup the neutron spin state in comparison to former measurements (sequential spin analysis) should be analyzed simultaneously (section 5.6). For this purpose two detectors, equipped with the already well characterized super polarizers (section 5.5) were used and the visibility α was determined.
- Determination of the storage time:
  The sensitivity of the EDM increases linear with the measurement time. For the requested beam time four types of precession chamber settings (pure quarz insulator ring or an insulator ring coated with dPe) electrodes coated with NiMo and a chamber coated with Fomblin were used.
- Determination of the spin relaxation time (T1):
  In order to get some impression on the wall relaxation of the used materials, especially the T1 time of polarized UCN is of key interest. Keeping in mind that there will be no magnetic shield installed around the setup, the measurements

will certainly suffer from magnetic field gradients around the setup. Hence, a Helmholtz coil was installed around the storage chamber to prevent this effect.

6.1 Experimental Setup

The experimental setup consists of different subsystems, which are all have contact points to each outher and have to be adjusted to each other to guaranty a smooth measurement process. The subsystems of the setup are:

- neutron guiding/storage system and spin analyzing system
- spin guiding system
- vacuum and pressed air system
- data acquisition system
- measurement control software

These will be described in detail in the following sections. In Fig. 6.1 a schematic drawing of the neutron guiding system and the spin guiding/storage system are illustrated.

Neutron Guiding and Storage System

In the setup shown in Fig. 6.1 neutrons are provided from the Steyerl turbine (section 1.2.2). They are guided from the PF2-UCN beam line exit (Fig. 6.1) through the main beam line shutter (Fig. 6.1) into the experimental area. Here, all guides are made of electropolished stainless steel guides with an outer diameter of 81 mm and a wall thickness of 1 mm. Stainless steel guides were used in this part of the setup because the experimental shutter and the first 45° bend were provided from ILL. For the the part of the setup with polarized neutrons starting with the polarizer (Fig. 6.1) only coated glass guides were used because of the high depolarization of stainless steel guides. Pictures, illustrating the described parts of the setup, are shown in App. G. The complete setup is build on an aluminum support structure.

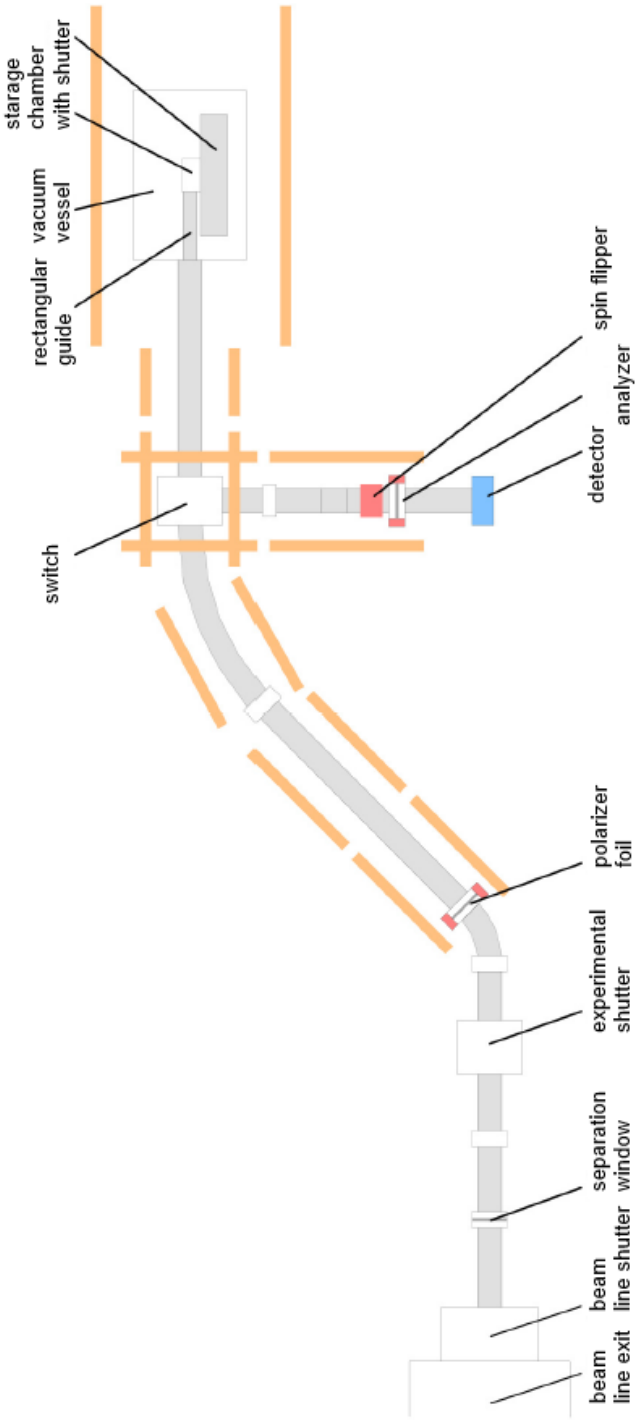

Figure 6.1: Illustration of the setup from the side. The guiding fields are made of rectangular Helmholtz coils and are shown in orange here. They are arranged around the neutron guides, shown in gray. Taken from [124] Fig. 11.

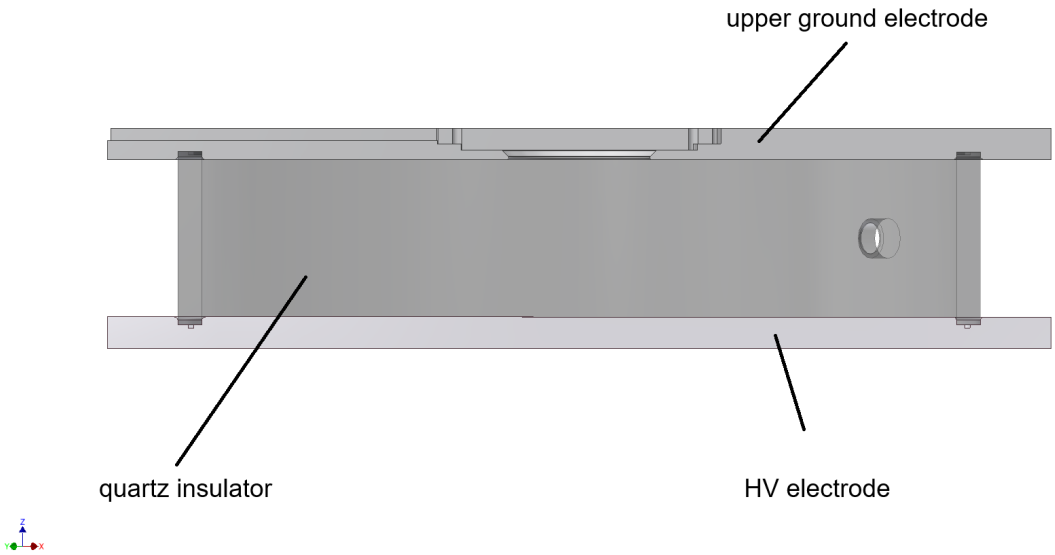

Figure 6.2: Sectional drawing of the nEDM spectrometer chamber. Through a hole in the upper ground electrode the neutrons are filled into the chamber. The quartz insulator is in between the ground electrode and the HV electrode at the bottom.

The neutrons are guided by a 300 mm stainless steel guide through the separation aluminum window (Fig. 6.1) to the experimental shutter (Fig. 6.1). This experimental beam shutter is installed to suppress the neutron background during a measurement from the turbine after filling the setup. Then the neutrons are guided through a 250 mm long guide and a 45° bend section into the polarizer foil holder (Fig. 6.1), which is also serving as a transition piece to NiMo coated glass guides with an outer diameter of 90 mm and a wall thickness of 5 mm. Behind the polarizer foil the neutrons are guided through an 1 m long glass guides and a 45° glass bend section (Fig. G.4) into the switch (Fig. 6.1 and Fig. G.5).
From the switch the neutrons can be guided into a vacuum vessel (Fig. 6.1) through a transition to the rectangular feeding guide (width of 80 mm, a height of 56 mm and a length of 300 mm; Fig. 6.3 and Fig. 6.1). The transition to a rectangular guide section is necessary for the future nEDM experiment, because the space on top and bottom of the precession chamber (Fig. 6.2) is limited by the magnetometers. All components were adjusted with the purpose to avoid slits between the different components.

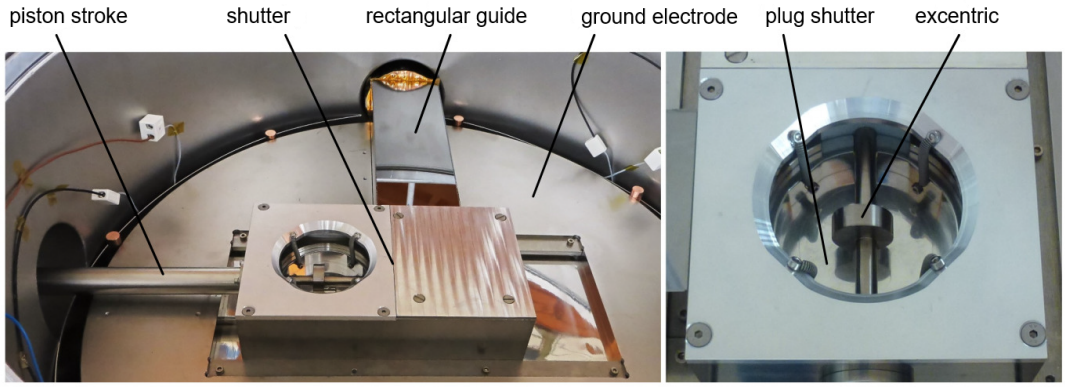

Figure 6.3: Picture of the precession chamber shutter system. Fig. 18. in [124].

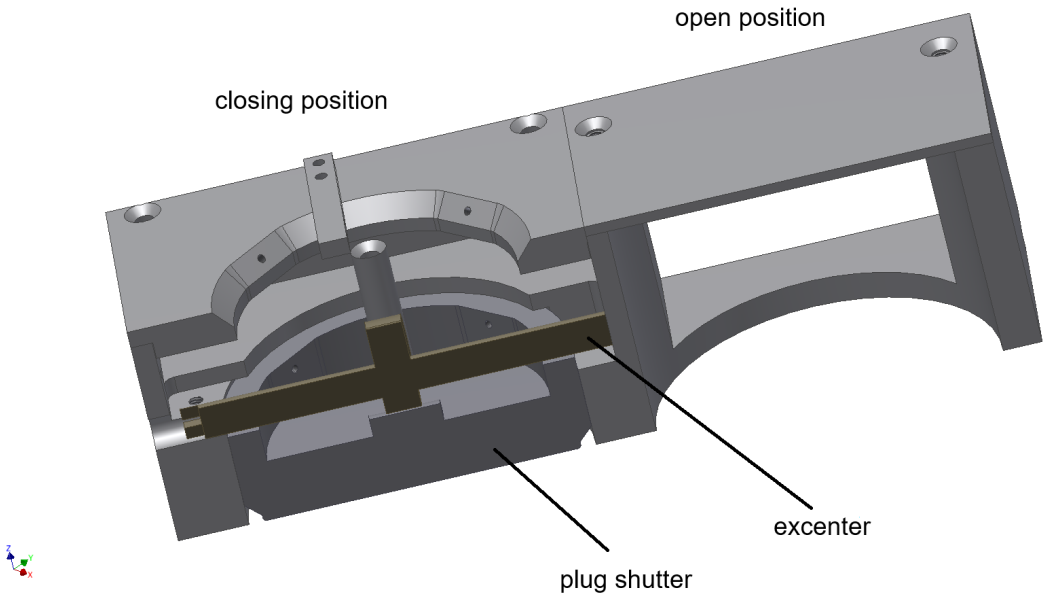

Figure 6.4: Sectional drawing of the nEDM spectrometer shutter system. On the left side is the closed position with the plug shutter with the excenter and on the right side the filling position.

Afterwards the neutrons are guided through the shutter (Fig. 6.3 and Fig. 6.1) into the precession chamber (Fig. 6.1). The shutter system is shown in detail in Fig. 6.3 and in a sectional drawing in Fig. 6.4. The shutter can be linearly moved with a piston stroke from the side, which is driven with a pressed air cylinder. If the shutter is pulled to the left side in Fig. 6.3 neutrons can be filled into the chamber. To close the chamber the piston stroke is pushed to the right side and then the plug

(Fig. 6.3) is pushed down by a rotational movement of an excenter and closes the chamber. A slit less than 0.1 mm is measured in closed position. More details on materials suitable for the precession chamber are described in detail in Section 4.5. The other direction starting again at the switch guides the neutrons to the simultaneous spin analyzing system, consisting of the spin flippers (Fig. 6.1) and the analyzer foil holders with foils (Fig. 6.1) and the detectors (Fig. 6.1). This system is described in detail in Section 5.6. Here, Fig. 6.1 shows only a side view. For a frontal view schematic drawing see Fig. G.8 and for a picture see Fig. 5.12. The neutrons are guided on their way through the system 1 m upwards to shift the

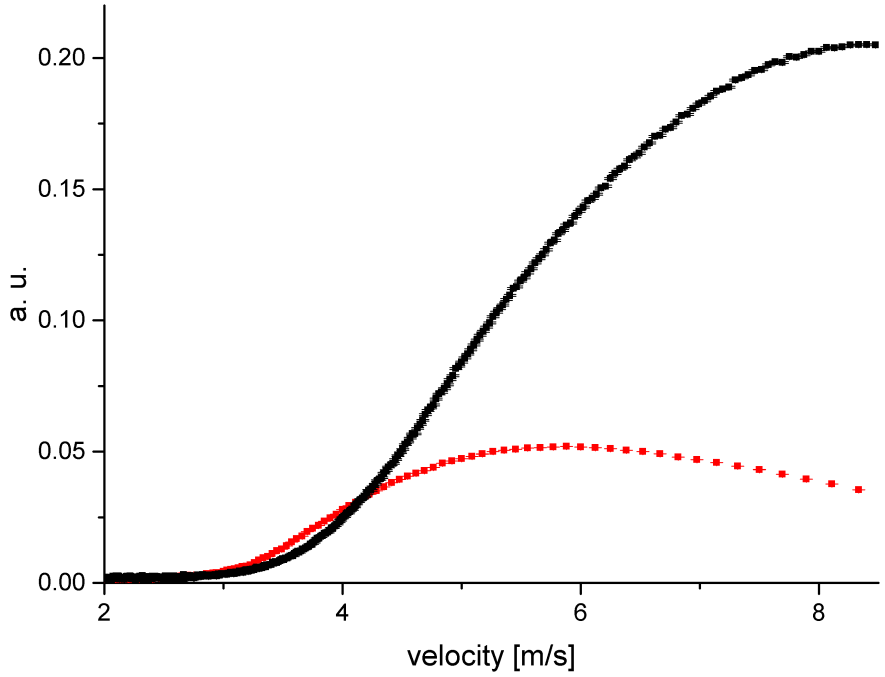

Figure 6.5: Result of a time of flight measurement to investigate the energy spectrum shift by guiding the UCNs 1 m upwards. In black is the spectrum on beam line height and in red the spectrum 1 m above is shown. The error bars arise from Poison statistics.

UCN spectrum (Fig. 6.5). This adaption is necessary because quartz has a neutron optical potential of 95 neV and is used as insulator in the precession chamber and the aluminum separation window (Fig. 6.1), at the beginning of the setup has a neutron optical potential of 54 neV. Hence, only neutrons in the small velocity band between 3.2 m/s and 4.2 m/s can be used in the experiment. But with a shifted

neutron spectrum there will be also neutrons with velocities less than 3.2 m/s (Fig. 6.5). This way a gain of more than 30 % of storeable neutrons was achieved.

Vacuum and Pressed Air Systems

For performing UCN storage measurements a vacuum in the range of 10^{-6} mbar is necessary. To reach this aim two turbo molecular pumps HiPase 300 from the company Peiffer Vacuum [127] are used in combination with an Adixen ACD 15 rough pump. One is installed at the switch and the other one at the vacuum vessel housing, at the precession chamber. With this system a vacuum of $2.2 \cdot 10^{-6}$ mbar was achieved during the experiment.
For several components in the setup pressed air is used, such as for the precession chamber shutter for the linear movement and for the rotational movement, the experimental shutter and the valves between the turbo molecular pumps and the rough pump. To drive this devices a pressure of 8 bar from the supply line was used.

Data Acquisition System and Measurement Control Software

For the Data acquisition and for controlling the setup two computers with different tasks are used. One computer is responsible for the Cascade detector control software and the data acquisition. A flow chart for this part is shown in Fig. G.1. The other computer is used for handling the measurement process and communicate all relevant data of a measurement via a RS 232 connection to the first computer where they are saved together with the detector data. A flow chart for this part of the setup is shown in Fig. G.2.
The detailed description will start with the hardware components to be controlled by PC 1 (Fig. G.1). The two detectors had to be supplied with high voltage of 1125 V. Therefore, a NHQ 203M from iseg [128] was used. The recorded pre-amplified signals from both detectors were send respectively to a DAQ Box, were all data processing takes place. From the DAQ Boxes the data were send to PC 1 and displayed with the cascade detector control software [99]. The detectors were flushed with an argon carbon dioxide mixture (90/10 %). For coordinating the detectors with the measurement cycles they were started and stopped with an external 5 V trigger signal mastered by PC 2.
PC 2 (Fig. G.2) is connected with two control boxes with a National Instruments

card inside, respectively. Control box 1 was doing the communication with the control panel of the Steyerl Turbine and coordinated the signal requests, veto and permission. With this box several position sensors and the vacuum sensor were read out. Three sensors were monitoring the rotational movement for the precession chamber, one inside, if the plug is moving and two outside, if the rotational movement was executed. For the linear motion one position sensor was installed on top of the dummy ground electrode and one outside at the slides for the motion support structure.
With control box 2 (Fig. G.2) the spin flippers were operated and the two amplifiers were switched. The frequency for the spin flippers was tuned manually. The current and the frequency was controlled with current probe installed at the spin flippers and visualized with an oscilloscope. The box also controlled the pressed air valves between the turbo molecular pumps and the rough pump, also the pressed air valve moving the piston stroke of the precession chamber shutter and the rotary motion to close the precession chamber plug and for the experimental shutter. Also the switching of the guiding fields is operated with this box. PC 2 also moved and controlled the the linear stage in the switch.
All this information and control possibilities were covered in a control program, programmed with Labview, to coordinate the measurement process. The different possible measurement modes and a sequence of these are presented in the next section.

6.2 Measurement Procedure

With the setup two measurement modes were possible. A direct measurement mode without storing the neutrons and a storage mode. They will be described in the next sections. For all measurements the neutron switch in the Steyerl Turbine had to be requested. If the switch is at the PF2-UCN beam line position the control panel send the permission signal and PC 2 was setting a veto for the filling or measuring time (depending on the measurement mode) and simultaneously stopped sending a request signal. After a variable time, depending on the measurement, the veto was also stopped and the switch could supply another beam position with UCNs.

Direct Measurement Mode

The direct measurement mode was primarily for tuning the spin flippers and studying their behavior in different operating modes. It was possible to vary the switching order of the two spin flippers or both could be switched on or off in parallel. The variable measurement time is always split in two equal parts, one half of the time with the chosen setting and the other with opposite settings to get a direct comparison. The neutrons are guided from the Steyerl Turbine through the switch direct to the detectors. At the beginning of the measuring time the experimental shutter (Fig. 6.1(4)) is automatically opened by the control program and closed at the end.

Storage Measurement Mode

In the storage measurement mode where two analyzing modes were possible, the sequential and simultaneous analyzing mode. In the sequential analyzing mode both spin flippers were on or off at the same time. In this mode the emptying time was automatically increased by a factor of two because the not analyzed spin component was stored in the system during the first emptying period. In the simultaneous analyzing mode one spin flipper was off, while the other one was on and both spin components were analyzed at the same time. The different storage times for each measurement cycle have to be chosen. Also the filling and the emptying time have to be defined. This two time periods are predefined for later storage measurements and are fixed in the beginning of a measurement cycle. A measuring sequence was structured in the following way (Fig. 6.6):

1. First the setup is initialized. Therefore, the precession chamber shutter is opened, the switch is driven to the monitoring position, where the UCNs will be guided directly to the detector arm. Both spin flippers are switched off and a beam request is sent to the turbine control. If the permission from the turbine control is received the detectors are triggered and the experimental beam shutter is opened, starting a 20 s monitoring measurement.
2. After this monitoring time the experimental beam shutter is closed for usually 20 s until the switch is moved into the filling position.
3. Now the precession chamber is filled with UCNs for a certain time. For quartz combined with NiMo coated electrodes it was i.e. 80 s (Fig. 6.7).

4. After the filling time the precession chamber is closed and the storage time starts, which is varied between the measurements. During this time the switch is moved to the emptying position (from the chamber to the simultaneous spin analyzing system arm) and the preselected spin flipper is switched on.
5. Now the stored neutrons are emptied to the detectors and the spin is analyzed. After the emptying time the detector gets a repeated trigger signal to stop the measurement.

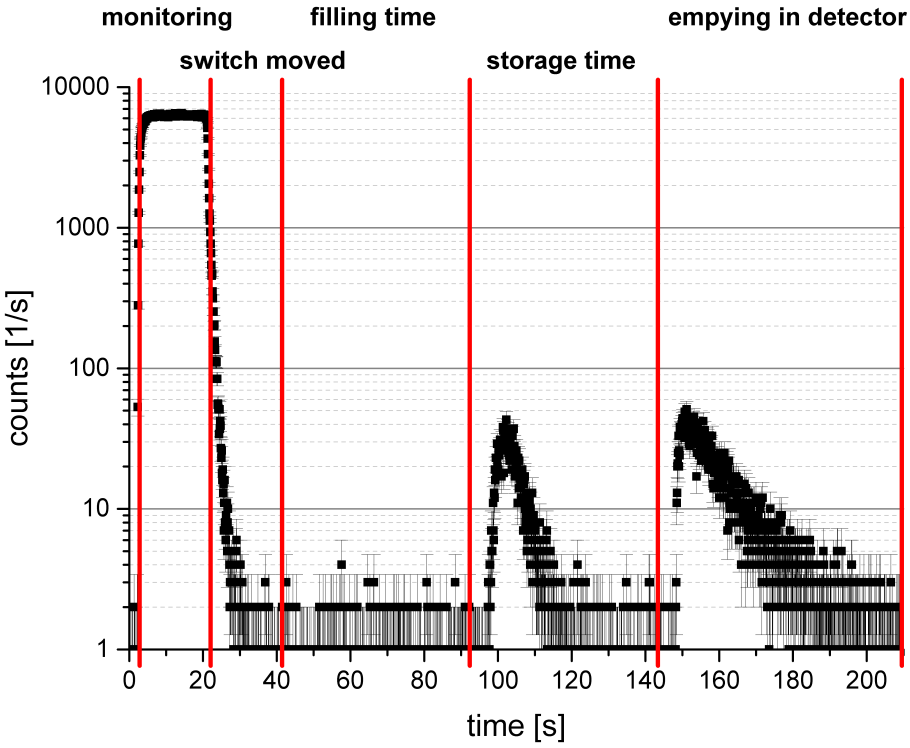

Figure 6.6: The time series of the count rate shows a typical measurement sequence in the storage mode for a detector with spin flipper off. After the monitoring time, the switch is moved in filling position, followed by the filling time, then the neutrons are stored and are emptied to the detection arm. The error bars arise from Poison statistics. While the UCNs were stored already a first emptying peak occurred. This arises from UCNs stored in between the closed precession chamber and the switch and are guided to the detector when the switch is moved to the emptying position.

Before collecting data for a storage curve with different precession chamber coatings and their preparation, a filling curve and an emptying curve have to be measured. The results of these measurements are presented in the following sections.

Filling and Emptying Curves

For measuring the filling curve the emptying and the storage time were set to a constant period. The filling time was varied as it is shown for example for the precession chamber with NiMo coated electrodes and the quartz insulator ring in Fig. 6.7. For each material used in the precession chamber, an individual filling curve was measured and the optimal filling time at the point, when the curve reaches the plateau. The chosen filling times are listed in Tab. 6.1 in dependence of the precession chamber material. The filling curve follows an single exponential growth, as fitted in Fig. 6.7.

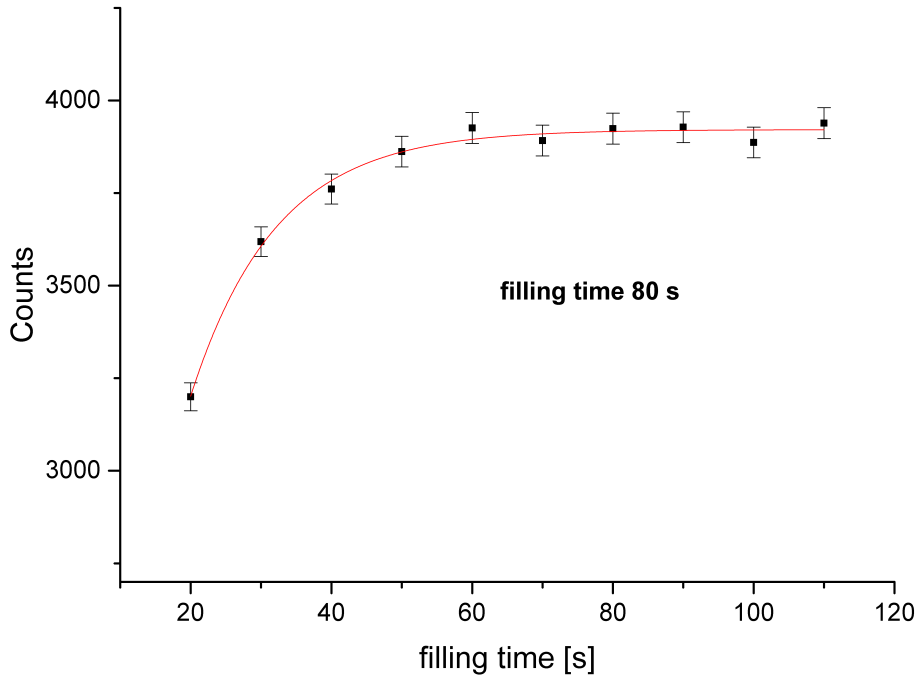

Figure 6.7: Filling curve for the precession chamber with NiMo coated electrodes and the quartz insulator ring. The red curve shows an exponential fit function and the optimal filling time was found to be 80 s for this configuration. The error bars arise from Poison statistics.

An example for an emptying curve after a storage of the UCNs of 20 s in the precession chamber with NiMo coated electrodes and the quartz insulator ring is shown in Fig. 6.8. Here a double exponential decay was necessary for fitting, because UCNs with two different emptying constants are stored in the chamber. The component of

fast UCNs cleans out for longer storage times. For the faster UCNs an emptying time constant of $t_1 = 9.4 \pm 0.4\,\mathrm{s}$ was found and for the slower component $t_2 = 18.6 \pm 2.4\,\mathrm{s}$. For a storage time of 70 s the emptying curve can be fitted with a single exponential decay with an emptying time constant of $t_1 = 20.7 \pm 0.4\,\mathrm{s}$.

precession chamber material	filling time [s]	emptying time [s]
NiMo/quartz	80	80
NiMo/dPE	80	80
Fomblin	100	140

Table 6.1: Filling and emptying times chosen f in dependence of the different precession chamber materials.

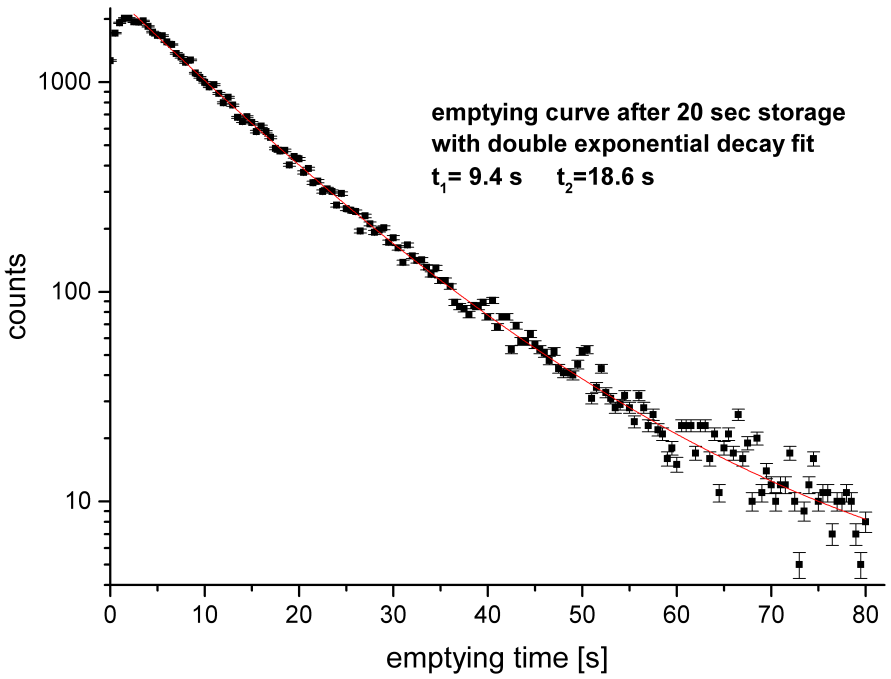

Figure 6.8: Emptying curve after storing UCNs for 20 s in the precession chamber with NiMo (85/15 wt%) coated electrodes and the quartz insulator ring. An double exponential decay was fitted to the measuring points. The error bars arise from Poison statistics.

6.3 Results and Evaluation

In order to figure out the suitable material for the future nEDM experiment precession chamber in Munich, different materials were tested. For the test two full scale quartz rings were used, one without any coating and one dPE coated. The dummy electrodes were made of aluminum and all parts, which were in contact with UCNs were polished and coated with 500 nm NiMo (85/15 wt%). Another test arrangement was an aluminum chamber, completely coated with Fomblin grease. The results for the measurements will be presented in the following sections.

6.3.1 Effective Lifetime Determination

For each tested material in the setup a storage curve was measured. Therefore, the storage time of the UCNs in the precession chamber was varied and repeated for a robust statistic. All shown data are background corrected and the error bars arise from Poison statistic ($\Delta N = \sqrt{N}$). The background was monitored during each measurement and was $\sim 0.8\,\text{counts/s}$. In the App. H in Tab. G.1 the repetitions of the measurements for a single storage time is listed for each storage curves. The following sections treat the measurement of the storage curves. Only a subset of the curves are shown, the others can be found in App. G.3. In every storage curve a double exponential fit was applied to diagnose the storage times and the initial amount of UCNs:

$$y = A_1 \cdot e^{x/t_1} + A_2 \cdot e^{x/t_2} \tag{6.1}$$

This fitting function was chosen because the UCN spectrum is divided into a faster and a slower part (Fig. 6.8), hence A_1 represents the initial amount and t_1 the effective lifetime of fast UCNs, and A_2 the initial amount and t_2 the effective lifetime of the slow UCNs. The fitting parameters for each measurement are listed in the respective section. The achievements of the various measurements will be discussed in the following.

Quartz NiMo Chamber

First, a pure quartz ring in combination with NiMo coated electrodes was tested. One measurement was performed where the components were installed after cleaning with acetone. For the other measurement the quartz ring was prepared by cleaning it in an ultrasonic bath with 5 % Tickopur R27 soap. Afterward the

ring was flushed with purified water and heated in a vacuum oven for 12 h at a temperature of 150° C.

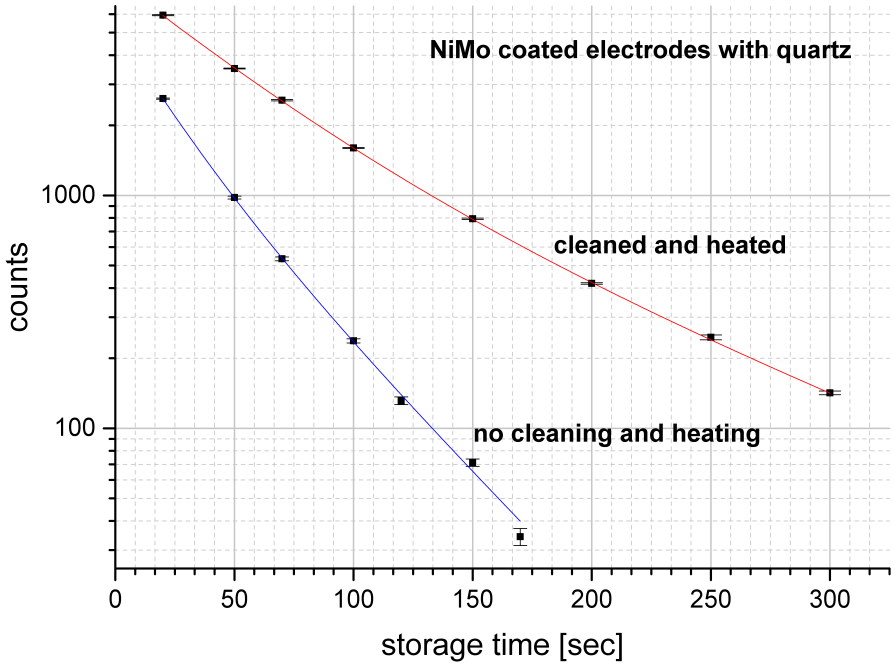

Figure 6.9: Storage curves for precession chamber with NiMo (85/15 wt%) coated electrodes and the quartz insulator ring after cleaning and heating (red curve) and before cleaning and heating (blue curve). The fits were done with a double exponential function and the error bars arise from Poison statistics.

	A_1	A_2	A_0	t_1 [s]	t_2 [s]	χ^2_{red}
without heating	3052 ± 1234	2318 ± 1611	5370 ± 2845	21 ± 8	42 ± 7	3.91
with heating	6291 ± 355	2201 ± 412	8492 ± 767	47 ± 2	106 ± 7	1.78

Table 6.2: Fitting parameters for the double exponential decay fit for the storage curve precession chamber with NiMo (85/15 wt%) coated electrodes and the quartz insulator ring.

The storage curve for the chamber with the cleaned quartz ring is shown in Fig. 6.9 and the results of the fitting curve for both measurements are listed in Tab. 6.2. The storage curve without cleaning and heating is shown in App. G.3 Fig. G.9. By

comparing the results, a clear improvement of the effective lifetimes t_1 by a factor of 2.2 and for t_2 2.5 is notable, which is due to an efficient preparation of the quartz ring. The initial UCN numbers N_0 in the chamber increased also by a factor of 1.6 and also the storage time in the chamber could be increased in the maximum from 170 s up to 300 s (compare Fig.G.9 and Fig. 6.9). But the amount of neutrons found through the fit has to be corrected because of losses due to the guiding from the precession chamber to the detector. Also the correction of the counted number of stored neutrons in the chamber for t_0 has to be done with respect of detector efficiency. The fractional bottle loss during emptying of $18/106 = 0.17$ has to be considered [62]. Therefore the emptying time is divided by the effective lifetime of the UCNs in the storage chamber. The main contribution to the detector loss is given by the transmission through the aluminum entrance window of the Cascade detector, which was measured to be 0.9 ± 0.02. On the way from the precession chamber to the detector the UCNs are guided through the following parts of the setup with the corresponding transmission:

- The precession chamber shutter with an estimated transmission of 0.8
- The rectangular guide with a length of 300 mm and an estimated transmission of 0.9
- In sum 1600 mm straight glass guides with a transmission of 0.96 per meter
- The switch has a transmission of 0.8
- The beam splitter has an transmission of 0.53
- The polarizer foil has a transmission of 0.9

Further, half of the UCNs are in the respectively other detector arm of the simultaneous spin detection system and have a probability of 0.5 to be reflected to the correct arm to be detected. Taking all this into account only ≈ 0.15 of the UCN are detected after the passage of the emptying system. Taking this into account for calculating the initial UCN amount in the precession chamber (volume 19600 cm^3) the initial polarized UCN density is 3 $\mathrm{UCN/cm}^3$. For the future nEDM in Munich an UCN transport system, similar to the tested one, has to be used because of the double chamber arrangement. Some parts of the transport system can be further optimized, like the transmission through the switch, the shutter of the precession chamber or the beam splitter. Nevertheless, further minimizing the transmission losses by optimization of the components are a key issue for increasing the number of neutrons, and so the sensitivity of the nEDM. Another conclusion which can be drawn, is that for a double chamber experiment only a simultaneous spin analyzing

system can be used, because in a sequential measurement the un-analyzed spin component is lost faster before it is analyzed. This was also confirmed in sequential

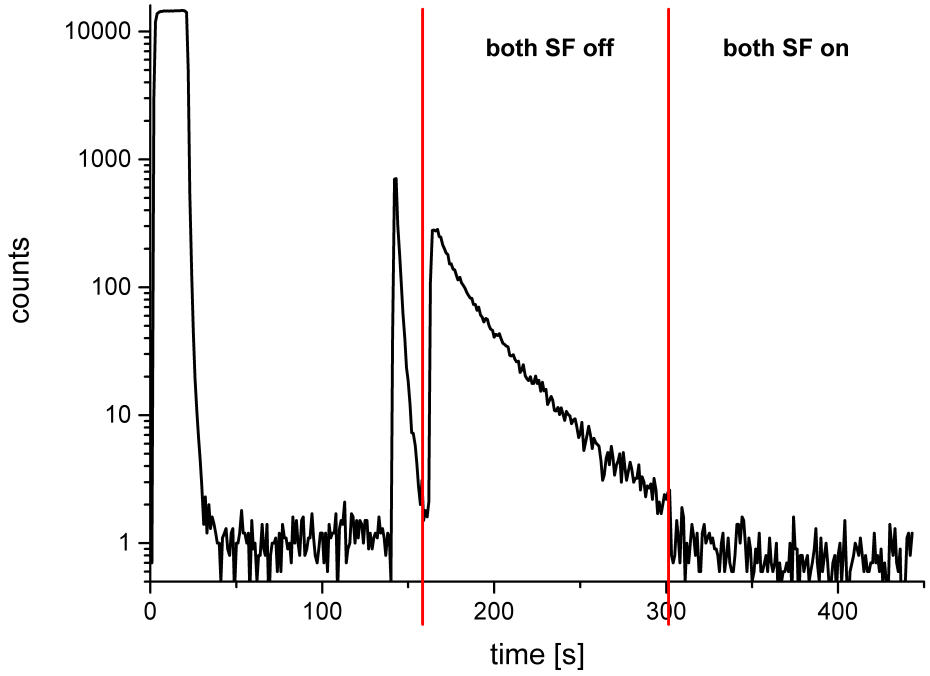

Figure 6.10: Measurement sequence of a sequential spin analysis measurement. First both spin flippers are switched off and after 140 s of emptying time the spin flippers are switched on. After this time no UCNs with the second spin state were notable.

analyzing tests with the presented system in this work. Also for a storage time of 20 s, shown in Fig. 6.10, no signal could be measured for the second analyzed spin state after an emptying time of 140 s for the first spin state that was analyzed.

dPE NiMo Chamber

The next material combination to be characterized in the mock up setup was a dPE coated quartz ring with NiMo (85/15 wt%) coated electrodes. But an incident caused the rectangular glass feeding guide to implode, because the system was vented to fast. All of the evacuated experimental parts outside the vacuum vessel, housing the precession chamber, was vented by a small slit between rectangular

guide and precession chamber shutter. Normally the system was vented slowly to guarantee a pressure exchange between the parts, obviously this time the guide was not resisting the pressure differences.
Despite, removing the glass chips, cleaning all of the components and installing a spare rectangular guide the storage time decreased by a factor of two (see Tab. 6.2 and Tab. 6.3). To check further causes of the decreasing storage time, all components were exchanged, appart from the quartz insulator ring and the NiMo (85/15 wt%) coated electrodes. To check, if the decrease in storage time was caused by contamination of the quartz insulator or the electrodes, the quartz ring coated with dPE was used.
A glass guide coated with dPE was successfully tested in [31] on its properties as precession chamber material. With a neutron optical potential of 214 neV, a storage time of 61 s in a 500 mm glass guide with an inner diameter of 115 mm and a loss coefficient $\eta = 1.3 \cdot 10^{-4}$ dPE is a promising covering material for the insulator ring. With the repaired setup all measurements presented in the following sections were performed.
Before the measurement with the dPE coated insulator ring could be started, a measurement for comparison with the cleaned pure quartz insulator ring was performed. The corresponding results for the fit of the storage curve shown in App. G.3 Fig. G.10 are presented in Tab. 6.3. The initial UCN number decreased notable by approximately 1400 UCN compared to the results shown in Tab.6.2. The storage

NiMo electrodes with	A_1	A_2	A_0	t_1 [s]	t_2 [s]	χ^2_{red}
dPE insulator	7455 ± 223	2663 ± 355	10118 ± 578	19 ± 1	50 ± 2	1.53
quartz insulator	3805 ± 377	3241 ± 542	7046 ± 919	24 ± 3	56 ± 3	1.33

Table 6.3: Fitting parameters for the double exponential decay fit for the storage curve precession chamber with NiMo (85/15 wt%) coated electrodes and a dPE insulator ring and for a chamber with NiMo (85/15 wt%) coated electrodes and quartz insulator.

curve for the measurement with the dPE coated insulator ring is shown in App. G.3 Fig. G.11 and the corresponding results of the double exponential decay fit are also presented in Tab. 6.3. Here, the storage times for both measurements are in the same range considering the errors. However, comparing the initial UCN numbers in the dPE coated insulator ring are approximately 3000 UCN more stored because of the higher neutron optical potential of the dPE.
For the combination of the NiMo (85/15 wt%) coated electrodes and the dPE

coated insulator ring a higher storage time could be expected due to the low loss coefficient of dPE and results presented by [31]. The electrodes contribute 71.4 % of the precession chamber surface. Hence, the storage time is dominated by the electrodes. Considering that in the former measurement setup a storage time for the long living UCN component for the quartz chamber of 106 ± 7 s was achieved, the main cause of the drops could be attributed to changes in the surface quality of the electrodes. A possible reason could be that the NiMo (85/15 wt%) coating on the aluminum electrodes (neutron optical potential of 54 neV) was fractionally removed, for a better bonding of the coating on the substrate a 50 nm thick titanium layer (neutron optical potential for titanium of -48 neV) was used. If the UCNs hit such a region of the electrode the neutrons are lost with a higher probability.

Fomblin Chamber

Another precession chamber material that was tested was a Fomblin coated chamber with a neutron optical potential of 107 neV [103]. Fomblin is often used in neutron storage experiments because Fomblin grease does not contain hydrogen and therefore no water film can arise on its surface. Another advantage is that in such a volume slits are closed by the grease and very high storage times can be reached to measure the neutron lifetime.
Here, Fomblin was used for the check after the incident, whether the UCN transport system performs like before or if there are small magnetic centers, caused by invisible and cleanable glass chips. Because of this magnetic centers the polarization of the UCN gets lost and the visibility decreases.
For the measurements the NiMo (85/15 wt%) coated electrodes were additionally coated with a thin film of Fomblin. As insulator ring an aluminum dummy with the same dimensions as the quartz ring was used and also coated.
The storage curve with corresponding fitting results of the measurements are shown in Fig. 6.11 and Tab. 6.4, showning that the initial UCN density increased in comparison with the NiMo (85/15 wt%) electrodes and the heated quartz ring by 40 %. Looking especially on the initial UCN number of the long living UCN component, an increase of a factor of 2 is notable. In turn this factor can also be seen in the storage time for Fomblin of 240 s in comparison to 106 s for NiMo (85/15 wt%) with quartz. With this test the long storage time in a nEDM storage chamber could be shown. However, conventional Fomblin grease is not suitable with high voltage and causes sparks, beginning at a voltage of 30 kV for a distance of the electrodes of 10 cm.

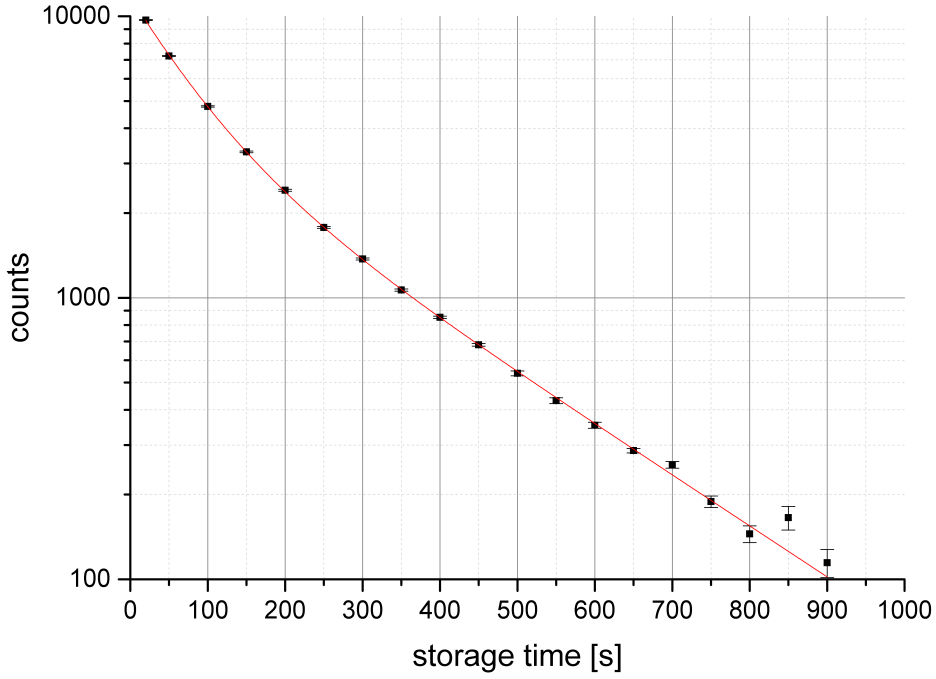

Figure 6.11: Storage curve for the Fomblin coated precession chamber with a double exponential fit. The corresponding fit results are listed in Tab. 6.4 and the error bars arise from Poison statistics.

A_1	A_2	A_0	t_1 [s]	t_2 [s]	χ^2_{red}
7425 ± 147	4322 ± 171	11747 ± 318	74 ± 2	240 ± 4	1.97

Table 6.4: Fitting parameters for the double exponential decay fit for the storage curve of the precession chamber coated with Fomblin shown in Fig. 6.11

6.3.2 Loss per Bounce Probability $\bar{\mu}$ and Loss Factor η

The materials used in a precession chamber have to achieve a low loss per bounce probability, beside a high neutron optical potential. For the different material combinations, tested in this thesis the median loss per bounce probability $\bar{\mu}$ and from this following loss factor η were calculated to check the capability for the future nEDM experiment.
With the equations presented in section 1.3.2 these two parameters can be determined. In Equation 1.35 the measured effective lifetime is determined by the measure-

ments presented in Section 6.3.1 and the neutron lifetime is $\tau_n = (880.3 \pm 1.1)\,\mathrm{s}$ [23]. The silt sizes in the precession chamber and the linked losses have to be well assessed, otherwise the loss coefficient is over- or underestimated. The slits in the precession chamber are measured to be under 0.007 mm for the quartz/dPE ring with the NiMo (85/15 wt%) coated electrodes. All of these slits are small channels with no direct escape possibility. Hence, the UCNs have to make several reflections in the slits to leave the chamber and therefore have a high probability to be reflected back into the chamber. This was explored in the work presented in [129]. The author found, that for a slit with the width of 0.25 mm $\approx$ 80 % of the UCNs are reflected back. For the precession chamber the slits are significant smaller and the reflection rate can be estimated to be much higher. Following this, the losses caused by slits can be assumed to be almost negligible.
If τ_l is known from previous calculations, $\bar{\mu}$ can be calculated with Equation 1.38 and with Equation 1.20 the loss factor η can be estimated. For the calculation of a chamber with a combination of quartz and any other material Tab. 6.5 the mean velocity for quartz was used, because after several wall collisions with both materials the neutron optical potential of quartz dominates and the stored spectrum becomes softer. For the Fomblin coated chamber no slits were taken into account, because it can be assumed that remaining small slits are closed by the grease. The results are comparable to other results for $\bar{\mu}$ and η in a nEDM precession chamber, as presented in [114] Tab. 5.9 for the RAL-Sussex nEDM experiment. The errors arise from Gaussian error propagation.

	$\tau_{eff}[s]$	$\bar{\mu}$	η
Fomlin chamber	240 ± 4	$(1.3 \pm 0.2)\cdot 10^{-4}$	$(1.0 \pm 0.1)\cdot 10^{-4}$
NiMo with dPE	50 ± 2	$(5.2 \pm 0.8)\cdot 10^{-4}$	$(4.1 \pm 0.6)\cdot 10^{-4}$
NiMo with quartz chamber 1	106 ± 7	$(3.3 \pm 0.5)\cdot 10^{-4}$	$(2.6 \pm 0.4)\cdot 10^{-4}$
NiMo with quartz chamber 2	56 ± 3	$(6.9 \pm 1.0)\cdot 10^{-4}$	$(5.5 \pm 0.8)\cdot 10^{-4}$

Table 6.5: Loss per bounce probability $\bar{\mu}$ and loss factor η for the different materials used in the precession chamber. The errors are calculated with Gaussian error propagation.

The value for $\bar{\mu}$ the dPE insulator ring with the NiMo (85/15 wt%) coated electrodes is compared to $\bar{\mu}_{dPE} = 1.4 \cdot 10^{-4}$ [31] by a factor of 3 worse. But this measurement was performed after the incident with the rectangular feeding guide. By comparing the results before the incident for the quartz ring in combination with the NiMo (85/15 wt%) electrodes also a degradation of the performance of a factor of 2 was

found. This supports the assumption done in the end of section 6.3.1 that the surface of the electrodes was damaged.

6.3.3 Visibility α and Longitudinal Spin Polarization Lifetime T_1 for the Different Precession Chambers

The visibility α and the longitudinal polarization lifetime of the spin T_1 are also important property of the precession chamber and the system.

The visibility was examined in dependence of the emptying time. Here for example

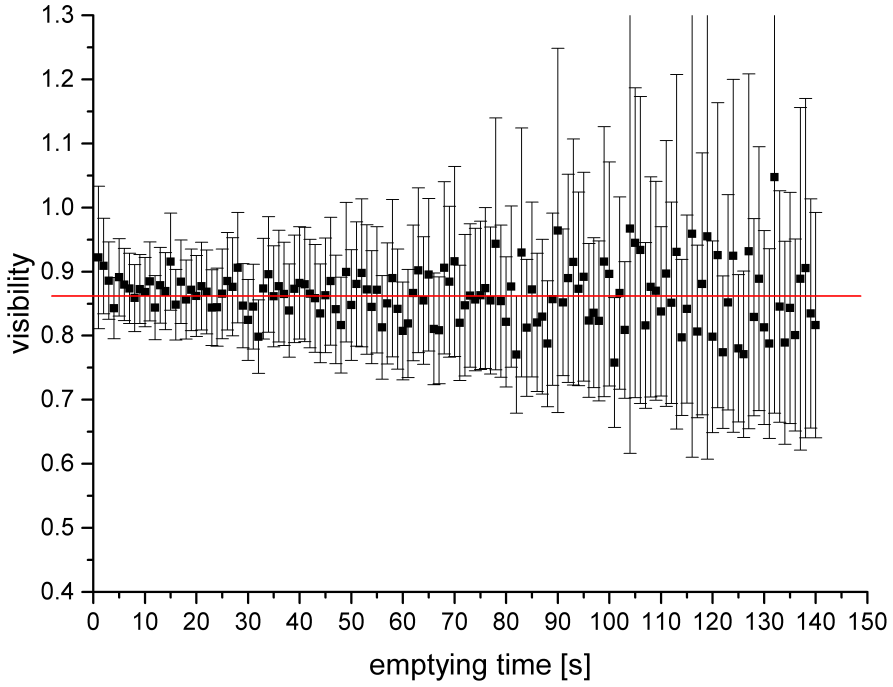

Figure 6.12: Time series of the asymmetry between the two detection arms in dependence of the emptying time after a storage time of 100 s. The error bars arise from Poison statistics and error propagation.

the result for the Fomblin coated chamber is displayed. is shown in Fig. 6.12 for an storage time of 100 s, from which follows, that over the emptying time the visibility stays constant. Also for the NiMo (85/15 wt%) coated electrodes in combination with the quartz chamber the visibility stays constant over the emptying time at a level of $\approx$ 85%. Compared to the measurements in direct mode the results show a further improvement to the in section 5.7 calculated emptying time of approximately

78 %. For all tested material combinations the visibilities are displayed in Fig. 6.13. The visibilities were calculated with formula 5.2 and the errors were calculated with Gaussian error propagation. The visibilities are shown in dependence of the storage time, where the curve for the nEDM chamber, without a holding field (Fig.6.13 in pink) shows a clear decrease of the visibility of less than 70 % for all storage times up to 150 s is observed. The red data set represents the measurement with the quartz insulator with NiMo (85/15 wt%) coated electrodes. The visibility decreases from 86 $\pm$ 1% for 20 s storage to 79 $\pm$ 1% for 300 s storage time, following an exponential decay as described by Equation 6.2. For the dPE coated insulator ring with the NiMo (85/15 wt%) electrodes the visibility decreases much faster than for the comparable measurement with quartz (shown in Fig. 6.13 blue and green data sets). From this it can be suggested that the dPE coated ring is contaminated with any depolarizing material (i.e. water or oil with magnetic particles). An oil film can arise in the surface during the coating process.
The incident with the rectangular guide can not explain the contamination, because the possible contaminated NiMo (85/15 wt%) electrodes did not show any influence on the reference measurement with the quartz ring (Fig. 6.13). In order to explain this result, further test series have to be performed to clarify the reason of the contamination.
For the Fomblin coated chamber the results show a gentle exponential decay up to a storage time of 700 s (6.13 in black). Beyond this storage time only a few measurements were performed. But the result suggests that also for really long storage times the visibility is above 80 %. However, for all materials the measured visibility was above 80 % for a storage time of 200 s.
Out of the visibility data the spin polarization lifetime T_1 time can be extracted by fitting an exponential decay, described by [65]:

$$\alpha(T) = \frac{N_A - N_B}{N_A + N_B} = \frac{P_0 e^{-T/T_1}}{1 + \frac{p_{fast}}{1-p_{fast}} e^{-T(1/\tau_{fast} - 1/\tau_{slow})}} \tag{6.2}$$

Here, P_0 is the initial polarization of the UCNs, p_{fast} is the ratio of fast UCNs and τ_{fast} and τ_{slow} are the effective lifetimes for the different UCN velocities, respectively, as in Section 6.3.1.

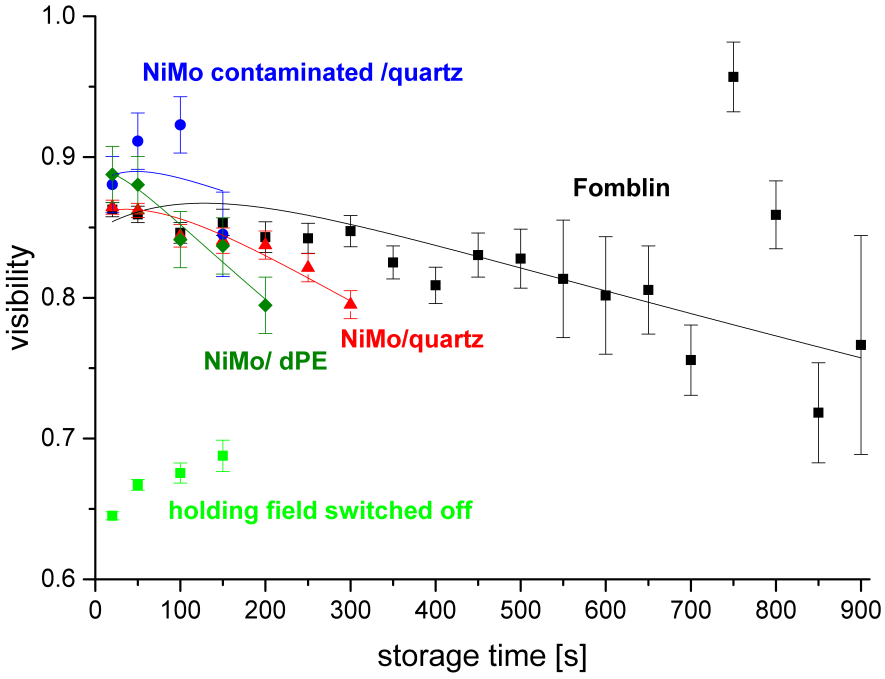

Figure 6.13: The time series shows the visibility for the different precession chamber materials in dependence of the storage time. The black data points are measured with the Fomblin coated chamber, the red ones are for quartz insulator with NiMo (85/15 wt%) coated electrodes (NiMo (85/15 wt%) with quartz chamber 1), the blue for NiMo (85/15 wt%) after contamination (NiMo (85/15 wt%) with quartz chamber 2), the dark green one for dPE insulator with NiMo (85/15 wt%) coated electrodes and green is for a measurement with quartz insulator with NiMo (85/15 wt%) coated electrodes and the magnetic holding field around the precession chamber switched off. The fits are done with Formula 6.2 and the parameters are listed in Tab. 6.6. The error bars arise from Poison statistics and error propagation.

The fitting results are shown in Tab. 6.6 for the different data sets, where for all fits the initial polarization was fixed at 91 %, because the best fits for all data sets could be achieved. This value differs from the polarization found in the characterization measurements in section 5.5 leading to the assumption that somewhere on the transport way some UCNs are depolarized. Also the effective lifetimes were fixed for the fits.

The results are showing high T_1 times 2307 $\pm$ 119 s for NiMo (85/15 wt%) in

	P_0	T_1	p_{fast}	t_{fast} [s]	t_{slow} [s]	χ^2_{red}
Fomblin chamber	0.91	4901 ± 715	0.07 ± 0.01	74 ± 2	240 ± 4	5.79
NiMo with quartz chamber 1	0.91	2307 ± 119	0.055 ± 0.005	47 ± 2	106 ± 7	0.75
NiMo with dPE	0.91	1536 ± 103	0.02 ± 0.01	19 ± 1	50 ± 2	0.23
NiMo with quartz chamber 2	0.91	4023 ± 3619	0.03 ± 0.04	24 ± 3	56 ± 3	1.64

Table 6.6: Fitting parameters for fits shown in Fig. 6.13.

combination with the quartz insulator ring. Compared with the results of the RAL-Sussex nEDM experiment [65] with a T_1 time of 1930 s the precession chamber performance is suitable. The Fomblin coated chamber showed the highest T_1 time with 4901 $\pm$ 715 s. But as already mentioned Fomblin can not be used in the future nEDM setup. As expected from the visibility results the T_1 time for dPE is with 1536 $\pm$ 103 s much smaller because of the depolarization.
The depolarization probability is defined by:

$$\bar{\beta} = \frac{1}{\bar{\nu} \cdot T_1} \tag{6.3}$$

where $\bar{\nu}$ is the mean wall collision frequency. For the quartz insulator with the NiMo (85/15 wt%) coated electrodes a value of 25 Hz is found [130]. Therefore, the depolarization probability is calculated to $\bar{\beta}_{NiMo/quartz} = 1.73 \pm 0.17 \cdot 10^{-5}$. The error is calculated with Gaussian error propagation. The here found result is comparable with other tested material like DLC for usage in a nEDM precession chamber as presented by the author of [63].
Magnetic field measurements at the Physikalische Techinische Bundesanstalt (PTB) performed on the used electrodes to clarify, if magnetic centers in the electrodes cause depolarization of the stored UCN showed no influences for the holding field range of the mock up setup [106].
A confirmation of the results in further measurements with the nEDM μ-metal shield and the nEDM B_0 field, would give a significant increase of the visibility.

If this results can be confirmed in a next step measurement with the nEDM μ-metal shield and the nEDM B_0 field the visibility can be significantly increased. In [65] the visibility for operation under the RAL-Sussex nEDM experiment was measured to 63.4 ± 1.8 %. Comparing this with the results presented in this work the visibility can be improved by a factor of nearly 20 % for a nEDM storage time of 200 s.

6.3.4 μ-Metal Shield Passage

Because of the sharp magnetic field gradients at the edges, the spin polarization conservation during the μ-metal shield passage is a crucial factor for the future nEDM setup. To investigate the influence of this passage for the future nEDM, three layers of μ-metal with an hole of 100 mm for the neutron guide were build. The μ-metal was taken from the same batch as the plated for the real shield described in Section 2.4.1. A picture of the test setup is shown in Fig. G.7, Appendix G.2.

The three layers were mounted on the feeding and emptying arm of the precession

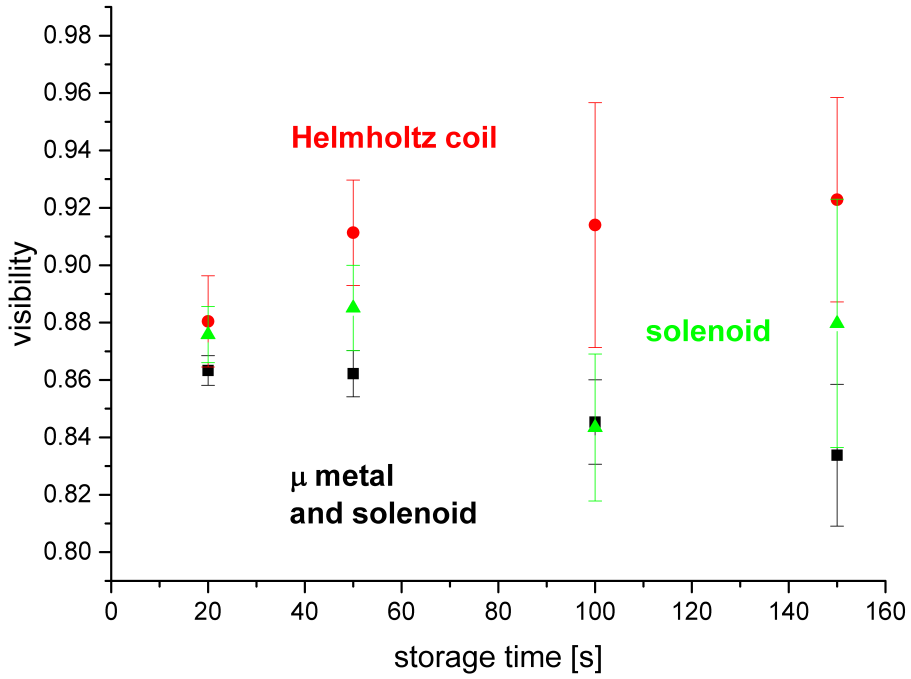

Figure 6.14: The time series shows the visibility for different configurations for the position with the μ-metal passage. The error bars arise from Poison statistics and error propagation.

chamber (Fig. 6.1 between (6) and (7)), respectively, and a storage curve was measured for the different configurations as described in section 6.2. The data was taken after the incident with the rectangular feeding guide and with the NiMo (85/15 wt%) coated electrodes and the Quartz insulator. Hence, the necessary data for the visibilities were only measurable with a suitable statistic up to a storage time of up to 150 s. In Fig. 6.14 the visibility is shown for the data taken with the Helmholtz coil in red. The green data set was measured with a solenoid coil with a field of 2 mT

around the neutron guide at the position, where the μ-metal shield dummy will be mounted. In Fig. 6.14 are the data that were taken with the solenoid coil driven with a field of 2 mT located between μ-metal and neutron guide shown in black. Fig. 6.15

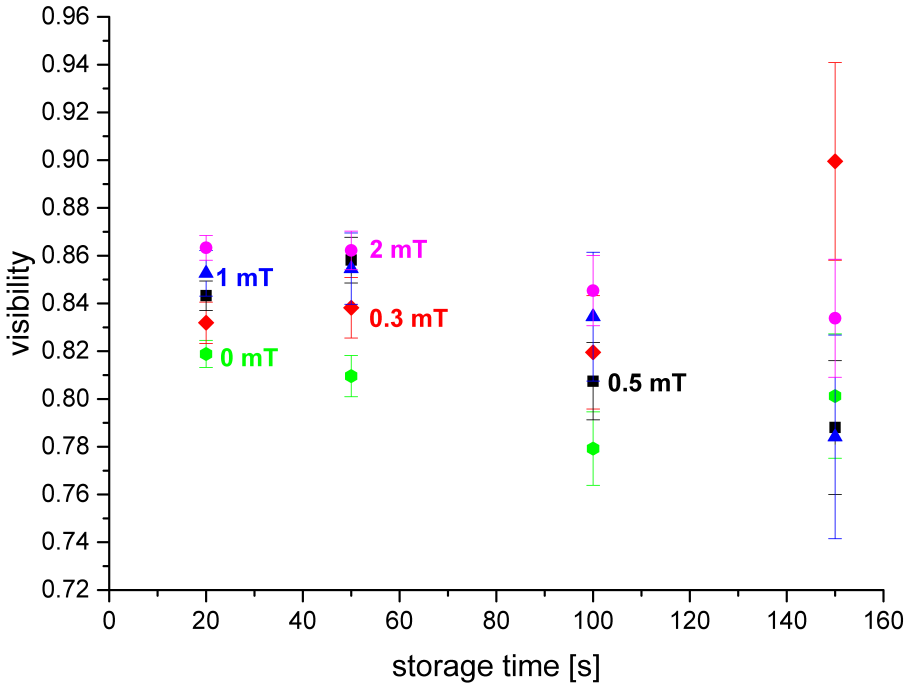

Figure 6.15: The time series shows the visibility for different applied fields in a solenoid coil as guiding field through three layers of μ-metal. The μ-metal was installed between precession chamber and switch. The error bars arise from Poison statistics and error propagation.

shows the results of a study to examine the influence of the magnetic field to avoid decreases of the visibility. The magnetic field of the solenoid was varied between 0.3 and 2 mT. The measurement without a magnetic field is shown in green. Already a magnetic field of 0.3 mT shows a compensating effect and the visibility is in the same range like without the μ-metal around the neutron guide with respect to the errors. The measurements were showing that the μ-metal shield passage without a compensating magnetic field will cause depolarization of the UCN and decrease the visibility. For the future nEDM setup a guiding field, maybe in another configuration is necessary.

6.4 Conclusions of the nEDM Test Setup Measurements

With the nEDM mock up measurement the UCN related designed, build and commissioned components for the future nEDM setup were characterized.
The switch and the plug shutter worked reliable and the tested systems can be established in the future nEDM setup. The analyzing power of the simultaneous spin analyzing system for the precession chamber with electrodes coated with NiMo (85/15 wt%) and a quartz ring is 84 $\pm$ 1% for a storage time of 200 s. Compared with the results of the RAL-Sussex nEDM simultaneous spin analyzing system an improvement of approximately 20 % could be reached. Additional the analyzing power stayed constant over lifetime T_1 is 2307 $\pm$ 119 s and the loss factor η is determined to 2.6 $\pm 0.4 \cdot 10^{-4}$. All these results are suitable compared to other nEDM experiments.
The results for the Fomblin coated precession chamber shows that without slits an effective lifetime up to 240 $\pm$ 4 s is possible. Also the T_1 time is with 4901 $\pm$ 715 s high. But Fomblin can not be used for a nEDM measurement because it is not HV suitable.
For the dPE coated insulator ring only an effective lifetime of 50 $\pm$ 2 s was achieved because of the destruction of the NiMo (85/15 wt%) coating of the electrodes. Nevertheless the visibility and the T_1 decreased faster in contrast to the comparable NiMo (85/15 wt%) coated electrodes with the quartz ring.
The calculations respective to the UCN transmission through the guide system was considered to be 15 % from the precession chamber to the detectors. This result can be improved by optimized bend sections above the precession chamber and in the switch. Also the beam splitter for the simultaneous spin analyzing system can be further optimized to achieve a higher transmission without decreasing the visibility.

Chapter 7

Summary and Conclusion

Within this thesis an UCN guide system with a total length of 17.7 m and bend section with in sum approximately 220° bends was build for the first time. The neutron guides were made of 1.5 m long glass tubes, all coated in a sputtering facility, special developed for coating these guides with 500 nm NiMo (85/15 wt%). The UCN guides is investigated on surface roughness with AFM measurements and the neutron optical potential of NiMo (85/15 wt%) is determined to be $V_F = 221\,\mathrm{neV}$ with the neutron reflectometer TREFF for a planar sample and in a guide with MIRA at the FRM II. With the measured setup a transmission per meter of $T_m = 96.1 \pm 0.6\,\%/m$ for the velocity between 4.5 m/s to 6 m/s is determined. To determine the diffusely scattered neutrons in the long guide system MCNP simulations were performed for the longest and the reference setup. For the transmission through a 15 m long guide a part of 4% of the UCN were diffusely scattered, for the reference with 2.7 m only 0.5 %. The result of the storage measurement after a guide system of 14 m was that the diffusely scattered neutrons are also not contributing to the useable UCN spectrum. This leads to the conclusion that in a longer guide system the diffusely scattered UCN part increases and that these UCNs are lost for an experiment installed after such a long feeding guide system. For a further measurement the matter of diffusely scattered UCNs in dependence of the guide length might be interesting and can be helpful for understanding the transport properties of long UCN guide systems.

For the storage measurement shutters were constructed, build and characterized and an UCN leakage rate of $< 0.2\,\mathrm{Counts/s}$ could be measured. The result of the storage measurements was a storage time of constant high level of 37 s for all tested guides with a corresponding UCN density of 0.28 UCN/cm^3. For storing UCNs in the complete guide system the storage time decreased only to $34.9 \pm 0.6\,\mathrm{s}$ because of the bigger slit area. With this results a loss rate per wall bounce is determined to $\eta = 2.7 \pm 0.3 \cdot 10^{-4}$ and is in good agreement with the theoretical value of $\eta = 2.5 \cdot 10^{-4}$.

The neutron guide system for the future nEDM experiment at the FRM II was

also build and characterized within this thesis. The guides had an outer diameter of 90 mm, a wall thickness of 5 mm and were coated with 500 nm NiMo (85/15 wt%). For the necessary straight UCN guides a transmission of 96.3 $\pm$ 1.2 %/m was measured using the same measurement principle as for the guides from the UCN source to the experiment. Also bend sections and beam splitters, made of glass, are necessary for guiding the neutrons to the precession chamber. They had all been constructed, build and tested successfully. The transmission for a 45° angle for a velocity region of 6 $-$ 3.3 m/s was 79.4 $\pm$ 0.2 %, and for the beam splitters a transmission in the same velocity range of 53.1 $\pm$ 0.3 % for BS No. 1 and for BS No. 2 82.6 $\pm$ 0.4% was measured, respectively. For the beam splitters also the asymmetry was determined to -0.33 $\pm$ 0.15 % for BS No. 1 and -0.19 $\pm$ 0.10 % for BS No. 2. Additionally a switch was build and in the characterization measurement the results for the velocity region of 5 $-$7 m/s are 90 $\pm$1% transmission for the straight through position and 80 $\pm$2 % for the 90° bend position.

Next to the UCN handling system also the spin manipulation system for the future nEDM has been developed within this work. Polarizer foils with a polarization power of over 99 % haven been developed. For the spin manipulation also different spin flippers were produced and all showed an efficiency of over 99 % for rotating the spin. Also the guiding fields, consisting of different Helmholtz coils were simulated and build for guiding the spin from the polarizer to the magnetic shielded room, housing the future nEDM, and for the section to the detectors. For the spin analysis a simultaneous spin analyzing system has been build and showed a visibility in direct measurement mode of about 78 %.

The next step was building a full size mock up setup of the future nEDM spectrometer to check the compatibility of all developed components. Additional to this also a precession chamber with a new developed shutter system was introduced. With stored UCN the simultaneous spin analyzing system showed an analyzing power of 84 $\pm$ 1% for a storage time of 200 s. Compared with the sequential spin analyzing system of the RAL-Sussex nEDM the simultaneous spin analyzing system shows an improvement of approximately 20 % for the visibility.

For the precession chamber with electrodes coated with NiMo (85/15 wt%) and a quartz ring an effective lifetime of 106 $\pm$ 7 s could be achieved. The corresponding polarization decay time T_1 was found to 2307 $\pm$ 119 s and the loss coefficient per wall bounce η was determined to be 2.6 $\pm 0.4 \cdot 10^{-4}$. For a Fomblin coated precession chamber without slits an effective lifetime up to 240 $\pm$ 4 s was possible. Also the T_1 time was high with 4901 $\pm$ 715 s, but however, the used Fomblin grease can not be used for a nEDM measurement because it is not HV suitable. Also a dPE coated

chamber is characterized. But because of problems with the apparatus only an effective lifetime of $50 \pm 2\,\mathrm{s}$ was measured. Nevertheless, for dPE the visibility and T_1 decreased faster in contrast to the comparable NiMo (85/15 wt%) coated electrodes with the quartz ring. This suggests that dPE has to be further characterized as a precession chamber material.

Since all planned next generation nEDMs are basing on a double chamber experiment all UCN guide systems get more complicated and the losses are increasing further. For the overall UCN transmission, reaching from the precession chamber to the UCN detectors, calculation, taking the achieved UCN transmissions through all UCN optical components into account, led to a value of approximately 15 %. But this number can be increased by further improvements of the guide system. This can be reached by increasing the beam splitter transmission by 30 % with the already characterized beam splitter. Or by optimizing the switch insert to reach a transmission increased by 10 %. Also the transmission through the precession chamber shutter and the rectangular feeding guide is not optimized jet and can be further improved.

In summary a complete working UCN guide system for the future Munich nEDM was developed in this thesis. This is including also the UCN transport from the UCN source to the experimental area. Also the spin polarizing and guiding system for the nEDM was build and characterized in this thesis. Furthermore most of the developed parts can be used for the future setup. Nevertheless some parts, like the rectangular feeding guide, has to be replaced by another neutron optical component, because the guides will enter the vacuum vessel of the future nEDM with another angle. Further a well characterized simultaneous spin analyzing system with the world wide highest visibility for a nEDM measurement was developed.

List of Figures

List of Tables

Bibliography

[1] Large Hadron Collider (LHC), Cern. `http://www.lhc-facts.ch/index.php?page=home`, 2016.

[2] G. Aad et al. Observation of a new particle in the search for the Standard Model Higgs boson with the ATLAS detector at the LHC. *Physics Letters B*, 716(1):1 – 29, 2012.

[3] S. Chatrchyan et al. Observation of a new boson at a mass of 125 GeV with the CMS experiment at the LHC . *Physics Letters B*, 716(1):30 – 61, 2012.

[4] Peter W. Higgs. Broken symmetries and the masses of gauge bosons. *Phys. Rev. Lett.*, 13:508–509, Oct 1964.

[5] F. Englert and R. Brout. Broken symmetry and the mass of gauge vector mesons. *Phys. Rev. Lett.*, 13:321–323, Aug 1964.

[6] R. H. Cyburt, B. D. Fields, and K. A. Olive. Primordial nucleosynthesis in light of WMAP. *Physics Letters B*, 567(3–4):227 – 234, 2003.

[7] A. D. Sakharov. Violation of CP Invariance, C Asymmetry, and Baryon Asymmetry of the Universe. *Soviet Journal of Experimental and Theoretical Physics Letters*, 5:24, January 1967.

[8] V. L. Fitch, R. F. Roth, J. S. Russ, and W. Vernon. Evidence for constructive interference between coherently regenerated and CP-nonconserving amplitudes. *Phys. Rev. Lett.*, 15:73–76, Jul 1965.

[9] A. Abulencia et al. Observation of $B_s^0 - \overline{b}_s^0$ oscillations. *Phys. Rev. Lett.*, 97:242003, Dec 2006.

[10] D. Colladay and V. Alan Kostelecký. CPT violation and the standard model. *Phys. Rev. D*, 55:6760–6774, Jun 1997.

[11] The ACME Collaboration. Order of magnitude smaller limit on the electric dipole moment of the electron. *Science*, 343(6168):269–272, 2014.

[12] S K Lamoreaux and R Golub. Experimental searches for the neutron electric dipole moment. *Journal of Physics G: Nuclear and Particle Physics*, 36(10):104002, 2009.

[13] C. A. et al. Baker. Improved Experimental Limit on the Electric Dipole Mo-

ment of the Neutron. *Physical Review Letters*, 97(13):131801, 2006.

[14] J. Engel, M. J. Ramsey-Musolf, and U. van Kolck. Electric Dipole Moments of Nucleons, Nuclei, and Atoms: The Standard Model and Beyond. *Prog. Part. Nucl. Phys.*, 71:21–74, 2013.

[15] W. C. Griffith, M. D. Swallows, T. H. Loftus, M. V. Romalis, B. R. Heckel, and E. N. Fortson. Improved limit on the permanent electric dipole moment of ^{199}Hg. *Phys. Rev. Lett.*, 102:101601, Mar 2009.

[16] J. M. et al. Pendlebury. A Revised Experimental Upper Limit on the Electric Dipole Moment of the Neutron. *Physics Review D*, 092003:1–23, 2015.

[17] M. G. D. van der Grinten. CryoEDM: A cryogenic experiment to measure the neutron electric dipole moment. *Nuclear Instruments and Methods in Physics Research, Section A: Accelerators, Spectrometers, Detectors and Associated Equipment*, 611(2-3):129–132, 2009.

[18] C. A. et al. Baker. CryoEDM: a cryogenic experiment to measure the neutron Electric Dipole Moment. *Journal of Physics: Conference Series*, 251:012055, 2010.

[19] Maurits Van Der Grinten and Cryoedm Collaboration. Experimental searches for electric dipole moments. *Journal of Physics G Nuclear and Particle Physics*, 36(10):104002, 2001.

[20] S. N. Balashov, K. Green, M. G. D. van der Grinten, P. G. Harris, H. Kraus, J. M. Pendlebury, D. B. Shiers, M. A. H. Tucker, and D. L. Wark. A Proposal for a Cryogenic Experiment to Measure the Neutron Electric Dipole Moment (nEDM). *Arxiv*, page 34, 2007.

[21] R. Golub, D. Richardson, and S.K. Lamoreaux. *Ultra-Cold Neutrons*. Taylor & Francis, 1991.

[22] V.K. Ignatovich. *The Physics of Ultracold Neutrons*. Oxford science publications. Clarendon Press, 1990.

[23] K. A. Olive et al. Review of Particle Physics. *Chin. Phys.*, C38:090001, 2014.

[24] Perkeo Homepage Universität Heidelberg. `http://www.physi.uni-heidelberg.de/Forschung/ANP/Perkeo/theorie.php`, 2015.

[25] Hartmut Abele. The neutron. its properties and basic interactions. *Progress in Particle and Nuclear Physics*, 60(1):1 – 81, 2008.

[26] Perc Homepage Universität Heidelberg. `http://www.physi.uni-heidelberg.de/Forschung/ANP/PERC/`, 2016.

[27] Heinz Maier-Leibnitz Zentrum. `http://www.mlz-garching.de/instrumente-und-labore/teilchenphysik/penelope.html`, 2015.

[28] A. et al. Serebrov. Measurement of the neutron lifetime using a gravitational trap and a low-temperature Fomblin coating. *Physics Letters B*, 605(1-2):72–78, 2005.

[29] F. et al. Atchison. Measurement of the Fermi potential of diamond-like carbon and other materials. *Nuclear Instruments and Methods in Physics Research, Section B: Beam Interactions with Materials and Atoms*, 260:647–656, 2007.

[30] F. et al. Atchison. Storage of ultracold neutrons in a volume coated with diamondlike carbon. *Phys. Rev. C*, 74:055501, Nov 2006.

[31] Th. et al. Brenner. Deuterated polyethylene coatings for ultra-cold neutron applications. *Applied Physics Letters*, 107(12), 2015.

[32] K. Bodek et al. Storage of ultracold neutrons in high resistivity, non-magnetic materials with high fermi potential. *Nuclear Instruments and Methods in Physics Research Section A: Accelerators, Spectrometers, Detectors and Associated Equipment*, 597(2–3):222 – 226, 2008.

[33] Institut Laue Langevin, Ultracold neutron facility. `https://www.ill.eu/instruments-support/instruments-groups/instruments/pf2/description/instrument-layout/`, 2016.

[34] A. Steyerl. A "neutron turbine" as an efficient source of ultracold neutrons. *Nuclear Instruments and Methods*, 125(3):461–469, 1975.

[35] A. et al. Steyerl. A new source of cold and ultracold neutrons. *Physics Letters A*, 116(7):347–352, 1986.

[36] R. Golub and J.M. Pendlebury. Super-thermal sources of ultra-cold neutrons. *Physics Letters A*, 53(2):133–135, 1975.

[37] W Schott, J M Pendlebury, I Altarev, S Groger, E Gutsmiedl, F J Hartmann, S Paul, G Petzoldt, P Schmidt-Wellenburg, and U Trinks. UCN production in superfluid helium. *European Physical Journal A*, 16(4):599–601, 2003.

[38] O. Zimmer, K. Baumann, M. Fertl, B. Franke, S. Mironov, C. Plonka, D. Rich, P. Schmidt-Wellenburg, H.-F. Wirth, and B. van den Brandt. Superfluid-helium converter for accumulation and extraction of ultracold neutrons. *Phys. Rev. Lett.*, 99:104801, Sep 2007.

[39] Oliver Zimmer, Florian M. Piegsa, and Sergey N. Ivanov. Superthermal source of ultracold neutrons for fundamental physics experiments. *Phys. Rev. Lett.*,

107:134801, Sep 2011.

[40] Y. et al. Masuda. Spallation ultracold neutron source of superfluid helium below 1 k. *Phys. Rev. Lett.*, 108:134801, Mar 2012.

[41] NIST Center for Neutron Research, 2016. `http://www.ncnr.nist.gov/resources/n-lengths/`.

[42] T. Lauer. *Investigation of a superthermal ultracold neutron source based on a solid deuterium converter for the TRIGA Mainz reactor*. Dissertation, Johannes Gutenberg Universität Mainz, Fachbereich Chemie, Pharmazie und Geowissenschaften, 2010.

[43] Bernhard Lauss. Ultracold neutron production at the second spallation target of the Paul Scherrer Institute. In *Physics Procedia*, volume 51, pages 98–101, 2014.

[44] A. Frei. *Produktion von ultrakalten Neutronen mit einem festen Deuteriumkonverter*. Phd thesis, Technische Universität München, Lehrstuhl für Experimentalphysik E18, 2008.

[45] Th. Lauer and Th. Zechlau. A prospective pulsed source of ultracold neutrons for experiments in fundamental neutron physics. *The European Physical Journal A*, 49(8):104, 2013.

[46] R. Golub. UCN at a triga reactor. *Nuclear Instruments and Methods in Physics Research, Section A: Accelerators, Spectrometers, Detectors and Associated Equipment*, 30:558–559, 1984.

[47] Heinz Maier-Leibnitz Zentrum. `http://www.mlz-garching.de/instrumente-und-labore/teilchenphysik/ucn.html`, 2016.

[48] D.M. Mattox. *Handbook of Physical Vapor Deposition (PVD) Processing*. Materials Science and Process Technology. Elsevier Science, 1998.

[49] K. Wasa, I. Kanno, and H. Kotera. *Handbook of Sputter Deposition Technology: Fundamentals and Applications for Functional Thin Films, Nano-materials and MEMS*. William Andrew, 2012.

[50] P.J. Martin. Review Ion-based methods for optical thin film deposition. *Journal of Materials Science*, 21:1–25, 1986.

[51] P.K.S.K.S.S. Harsha. *Principles of Vapor Deposition of Thin Films*. Elsevier Science, 2005.

[52] P. Sigmund. Theory of sputtering. I. Sputtering yield of amorphous and polycrystalline targets. *Physical Review*, 184(2):383–416, 1969.

[53] John A. Thornton. Influence of substrate temperature and deposition rate on structure of thick sputtered cu coatings. *Journal of Vacuum Science and Technology*, 12(4), 1975.

[54] Vladimir K Ignatovich. Ultracold neutrons — discovery and research. *Physics-Uspekhi*, 39(3):283, 1996.

[55] Klein M. *Experimente zur QM mit ultrakalten Neutronen.* Dissertation, Ruprecht- Karls- Universität Heidelberg, 2000.

[56] W. Faber, B. Bader, P. Heitjans, and A. Schirmer. On the use of a gradient resonance neutron spin flipper. *Nuclear Instruments and Methods in Physics Research Section A: Accelerators, Spectrometers, Detectors and Associated Equipment*, 294(1–2):241 – 244, 1990.

[57] V.I. Luschikov and Yu.V. Taran. On the calculation of the neutron adiabatic spin-flipper. *Nuclear Instruments and Methods in Physics Research Section A: Accelerators, Spectrometers, Detectors and Associated Equipment*, 228(1):159 – 160, 1984.

[58] J. Byrne. Determination of the efficiency of a neutron polarizer-analyser combination by the spin-flip method. *Nuclear Instruments and Methods*, 167(2):355 – 357, 1979.

[59] J. Byrne. *Neutrons, Nuclei and Matter: An Exploration of the Physics of Slow Neutrons.* Taylor & Francis, 1996.

[60] P. Geltenbort et al. A compact, large-diameter adiabatic spinflipper for ultracold neutrons. *Nuclear Instruments and Methods in Physics Research Section A: Accelerators, Spectrometers, Detectors and Associated Equipment*, 608(1):132 – 138, 2009.

[61] W.H. Kraan, S.V. Grigoriev, M.Th. Rekveldt, H. Fredrikze, C.F. de Vroege, and J. Plomp. Test of adiabatic spin flippers for application at pulsed neutron sources. *Nuclear Instruments and Methods in Physics Research Section A: Accelerators, Spectrometers, Detectors and Associated Equipment*, 510(3):334 – 345, 2003.

[62] C.A. Baker et al. Apparatus for measurement of the electric dipole moment of the neutron using a cohabiting atomic-mercury magnetometer. *Nuclear Instruments and Methods in Physics Research Section A: Accelerators, Spectrometers, Detectors and Associated Equipment*, 736:184 – 203, 2014.

[63] P. Fierlinger. *Losses and Depolarization of Stored Ultracold Neutrons on Diamond-like Carbon.* Phd thesis, Universität Zürich, 2005.

[64] J. P. Karch. Herstellung und Charakerisierung nicht depolarisierender UCN Leiter. Diplomarbeit, Johannes Gutenberg Universität Mainz, Fachbereich Physik, Mathematik und Informatik, 2011.

[65] Victor Hélaine. *Mesure du moment dipolaire électrique du neutron: analyse simultanée de spin et analyse préliminaire de données* . Phd thesis, Université de Cean Basse-Normandie, 2014.

[66] J. H. Smith, E M Purcell, and N F Ramsey. Experimental Limit to the Electric Dipole Moment of the Neutron. *Phys. Rev.*, 108(1):120–122, 1957.

[67] Norman F. Ramsey. A molecular beam resonance method with separated oscillating fields. *Phys. Rev.*, 78:695–699, Jun 1950.

[68] J.M. et al. Pendlebury. Search for a neutron electric dipole moment. *Physics Letters B*, 136(5-6):327–330, 1984.

[69] P. G. Harris, C A Baker, K Green, P Iaydjiev, S Ivanov, D J R May, J M Pendlebury, D Shiers, K F Smith, M Van Der Grinten, and P Geltenbort. New experimental limit on the electric dipole moment of the neutron. *Physical Review Letters*, 82(1):7, 1999.

[70] C. A. et al. Baker. Reply to Comment on An Improved Experimental Limit on the Electric Dipole Moment of the Neutron. *Physical Review D - Particles, Fields, Gravitation and Cosmology*, 98:149102, 2007.

[71] K.F. et al. Smith. A search for the electric dipole moment of the neutron. *Physics Letters B*, 234(1-2):191–196, 1990.

[72] I. S. et al. Altarev. A new upper limit on the electric dipole moment of the neutron. *Physics Letters B*, 102(1):13–16, 1981.

[73] A. P. et al. Serebrov. New measurements of neutron electric dipole moment. *arXiv*, page 9, 2013.

[74] I. S. et al. Altarev. New Measurement of the Electric-Dipole Moment of the Neutron. *Physics Letters B*, 276(1-2):242–246, 1992.

[75] J. M. et al. Pendlebury. Geometric-phase-induced false electric dipole moment signals for particles in traps. *Physical Review A - Atomic, Molecular, and Optical Physics*, 70(3):1–20, 2004.

[76] I. et al. Altarev. A next generation measurement of the electric dipole moment of the neutron at the FRM II. *Nuovo Cimento della Societa Italiana di Fisica C*, 35(4):122–127, 2012.

[77] Lins T. *High Precision Physics in Low Magnetic Fields: Implementation of*

a Sub-Nanotesla Field with Femtotesla Temporal Stability. Dissertation, Technische Universität München, Lehrstuhl für Experimentalphysik E18, 2016.

[78] Chesnevskaya S. *Investigation of electric fields, losses and depolarization of ultra-cold neutrons for the new nEDM experiment at FRM II*. Dissertation, Technische Universität München, Lehrstuhl für Experimentalphysik E18, 2015.

[79] Taubenheim B. *in preparation*. Dissertation, Technische Universität München, Lehrstuhl für Experimentalphysik E18, 2016.

[80] Sturm M. *in preparation*. Dissertation, Technische Universität München, Lehrstuhl für Experimentalphysik E18, 2016.

[81] Stuiber S. *in preparation*. Dissertation, Technische Universität München, Lehrstuhl für Experimentalphysik E18, 2016.

[82] Bartington Instruments Limited. `http://www.bartington.com/mag690-low-cost-three-axis-magnetic-field-sensor.html`, 2016.

[83] I. et al. Altarev. A magnetically shielded room with ultra low residual field and gradient. *Review of Scientific Instruments*, 85(7):6–9, 2014.

[84] I. et al. Altarev. A large-scale magnetic shield with 10^6 damping at millihertz frequencies. *Journal of Applied Physics*, 117(18), 2015.

[85] S. Afach et al. A measurement of the neutron to 199Hg magnetic moment ratio . *Physics Letters B*, 739:128 – 132, 2014.

[86] Taubenheim B. *Talk Annual nEDM meeting Munich 2014*. Talk, Technische Universität München, Lehrstuhl für Experimentalphysik E18, 2014.

[87] Rosner M. *Cesium status update 2*. Talk, Annual nEDM meeting, 2016.

[88] Kuchler F. *Electric dipole moment searches using the isotope 129-xenon*. Dissertation, Technische Universität München, 2014.

[89] Seidl S. *Characterization and noise measurement with an LTc-SQUID cryostat*. Bachelor thesis, Technische Universität München, 2012.

[90] S-DH Sputter-Dünnschichttechnik Heidelberg. `http://www.s-dh.de/`, 2015.

[91] T. Huber. *Transport and storage of Ultra-cold Neutrons in Replika-Guides*. Diploma thesis, Technische Universität München, Lehrstuhl für Experimentalphysik E18, 2011.

[92] Private communication with S. Wlokka, Technische Universität München, München, 2014.

[93] M. Daum et al. Transmission of ultra-cold neutrons through guides coated

with materials of high optical potential. *Nuclear Instruments and Methods in Physics Research Section A: Accelerators, Spectrometers, Detectors and Associated Equipment*, 741:71 – 77, 2014.

[94] B. et al. Blau. A prestorage method to measure neutron transmission of ultracold neutron guides. *Nuclear Instruments and Methods in Physics Research Section A: Accelerators, Spectrometers, Detectors and Associated Equipment*, 807:30–40, 2016.

[95] A. Frei, K. Schreckenbach, B. Franke, F.J. Hartmann, T. Huber, R. Picker, S. Paul, and P. Geltenbort. Transmission measurements of guides for ultracold neutrons using UCN capture activation analysis of vanadium. *Nuclear Instruments and Methods in Physics Research Section A: Accelerators, Spectrometers, Detectors and Associated Equipment*, 612(2):349 – 353, 2010.

[96] SCHOTT AG. `http://www.schott.com/tubing/german/special_glass/other_applications.html`, 2015.

[97] Technische Universität München, ZWE FRM II. `http://www.mlz-garching.de/wissenschaft-und-projekte/instrumentservice/neutronenoptik.html`, 2015.

[98] Technische Universität München, ZWE FRM II. `http://www.mlz-garching.de/instrumente/struktur/mira.html`, 2015.

[99] CDT CASCADE Detector Technologies GmbH. `http://n-cdt.com/`, 2015.

[100] Private communication with Dr. T. Lauer, Technische Universität München, München, 2014.

[101] J. Schroffenegger, P. Fierlinger, A. Hollering, P. Geltenbort, T. Lauer, H. Rauch, and T. Zechlau. Improved measurement of the neutron absorption cross section for very low velocities. *Physics Letters B*, 752:212–216, 2016.

[102] Lauer et al. to be published. 2016.

[103] S. Lamoreaux and R. Golub. Calculation of the ultracold neutron upscattering loss probability in fluid walled storage bottles using experimental measurements of the liquid thermomechanical properties of fomblin. *Physical Review C*, 66(4):044309, 2002.

[104] A. Hollering. Aufbau eines Neutronen Speicherexperiments zur Charakterisierung von Neutronenleitern für ultrakalte Neutronen. Bachelor thesis, Technische Universität München, E13, 2014.

[105] J. et al. Karch. Performance of the solid deuterium ultra-cold neutron source at

the pulsed reactor TRIGA Mainz. *The European Physical Journal A*, 50(4):1–11, 2014.

[106] Private communication with Dr. A. Schnabel, Physikalisch- Technische Bundesanstalt, Berlin, 2014.

[107] Private communication with Prof. Dr. P. Fierlinger, Technische Universität München, München, 2014.

[108] Physik Instrumente (PI) GmbH & Co. KG. `http://www.physikinstrumente.com/product-detail-page/m-414-701755.html?_ga=1.24879218.992335197.1448112435`, 2015.

[109] T. Zechlau. *Parameterstudien an der neuen Quelle für ultrakalte Neutronen am TRIGA Mainz*. Diploma thesis, Johannes Gutenberg Universität Mainz, 2012.

[110] F. et al. Atchison. Diamondlike carbon can replace beryllium in physics with ultracold neutrons. *Physics Letters B*, 642(1-2):24–27, 2006.

[111] F. et al. Atchison. First storage of ultracold neutrons using foils coated with diamond-like carbon. *Physics Letters B*, 625(1-2):19–25, 2005.

[112] Mark F. Makela. *Polarized Ultracold Neutrons: their transport in diamond guides and potential to search for physics beyond the standard model*. Phd thesis, Virginia Polytechnic Institute and State University, 2005.

[113] M. G. D. Van Der et al. Grinten. Characterization and development of diamond-like carbon coatings for storing ultracold neutrons. *Nuclear Instruments and Methods in Physics Research, Section A: Accelerators, Spectrometers, Detectors and Associated Equipment*, 423:421–427, 1999.

[114] Marcin Kuzniak. *The Neutron Electric Dipole Moment Experiment:Research and Development for the New Spectrometer*. Phd thesis, Jagiellonian University, 2008.

[115] Johannes Zenner. *The search for the neutron electric dipole moment*. Phd thesis, Johannes Gutenberg Universität Mainz, 2013.

[116] I et al. Altarev. Deuterated polyethylene coatings for ultra-cold neutron applications. *AIP*, 121604, 2015.

[117] K. et al. Bodek. Storage of ultracold neutrons in high resistivity, non-magnetic materials with high Fermi potential. *Nuclear Instruments and Methods in Physics Research, Section A: Accelerators, Spectrometers, Detectors and Associated Equipment*, 597(2-3):222–226, 2008.

[118] Adam Tarte Holley. *Ultracold Neutron Polarimetry in a Measurement of the β Asymmetry*. Phd thesis, North Carolina State University, 2012.

[119] H. Weinfurter, G. Badurek, H. Rauch, and D. Schwahn. Inelastic action of a gradient radio-frequency neutron spin flipper. *Zeitschrift für Physik B - Condensed Matter*, 72(2):195–201, 1988.

[120] nEDM homepage Munich Universität München. `http://www.universe-cluster.de/fierlinger/polbeam.html`, 2016.

[121] R. Herdin, A. Steyerl, A.R. Taylor, J.M. Pendlebury, and R. Golub. Experiment on the efficient polarization of ultracold neutrons. *Nuclear Instruments and Methods*, 148(2):353 – 357, 1978.

[122] Servowatt Leistungselektronik GmbH. `http://www.servowatt.de/de/`, 2016.

[123] Keysight Technologies Deutschland GmbH. `http://www.keysight.com/en/pd-1407410-pn-33210A/function-arbitrary-waveform-generator-10-mhz?cc=DE&lc=ger`, 2016.

[124] Seidl S. *Investigation of a spin manipulation system for the nEDM setup at the FRMII*. Master thesis, Technische Universität München,E 13, 2015.

[125] S. et al. Afach. A device for simultaneous spin analysis of ultracold neutrons. *The European Physical Journal A*, 51(11), 2015.

[126] S. et al. Afach. A device for simultaneous spin analysis of ultracold neutrons. *The European Physical Journal A*, 51(11):1–10, 2015.

[127] Pfeiffer Vacuum GmbH. `https://www.pfeiffer-vacuum.com/de/produkte/turbopumpen/hybridgelagert/hipace-300/`, 2016.

[128] iseg Spezialelektronik GmbH. `http://iseg-hv.de/de/products/detail/NHQ`, 2015.

[129] Schmidt-Wellenburg P.A. *Production of ultracold neutrons in superfluid helium under pressure*. Dissertation, Technische Universität München, 2009.

[130] Private communication with Dr. M. Bales, Technische Universität München, München, 2014.

[131] Varley F. Sears. Neutron scattering lengths and cross sections. *Neutron News*, 3(3):26–37, 1992.

Appendix

A Shutter Properties

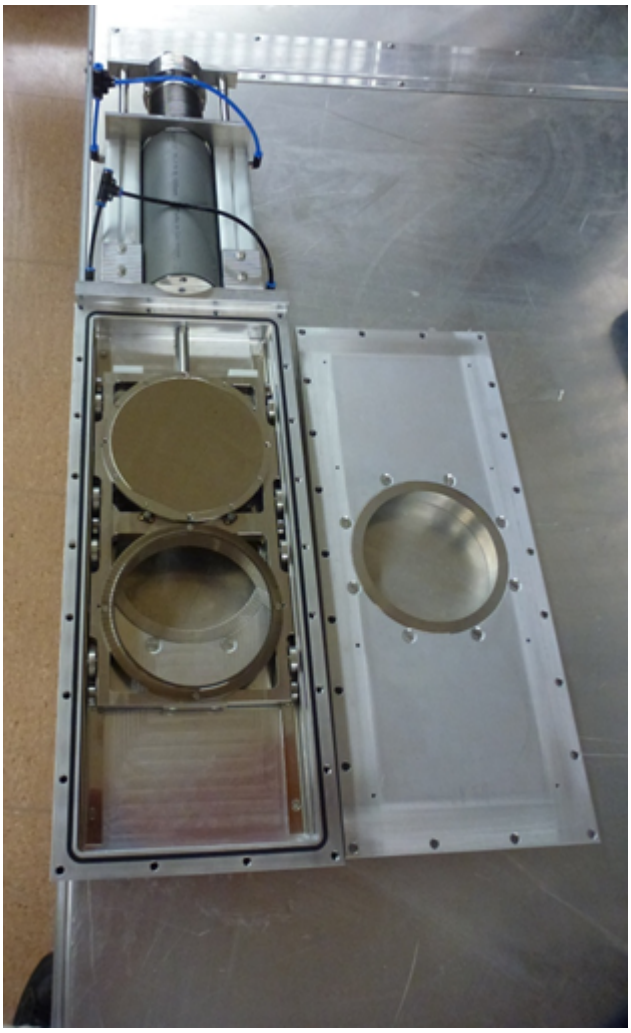

Figure A.1: Picture of an open shutter.

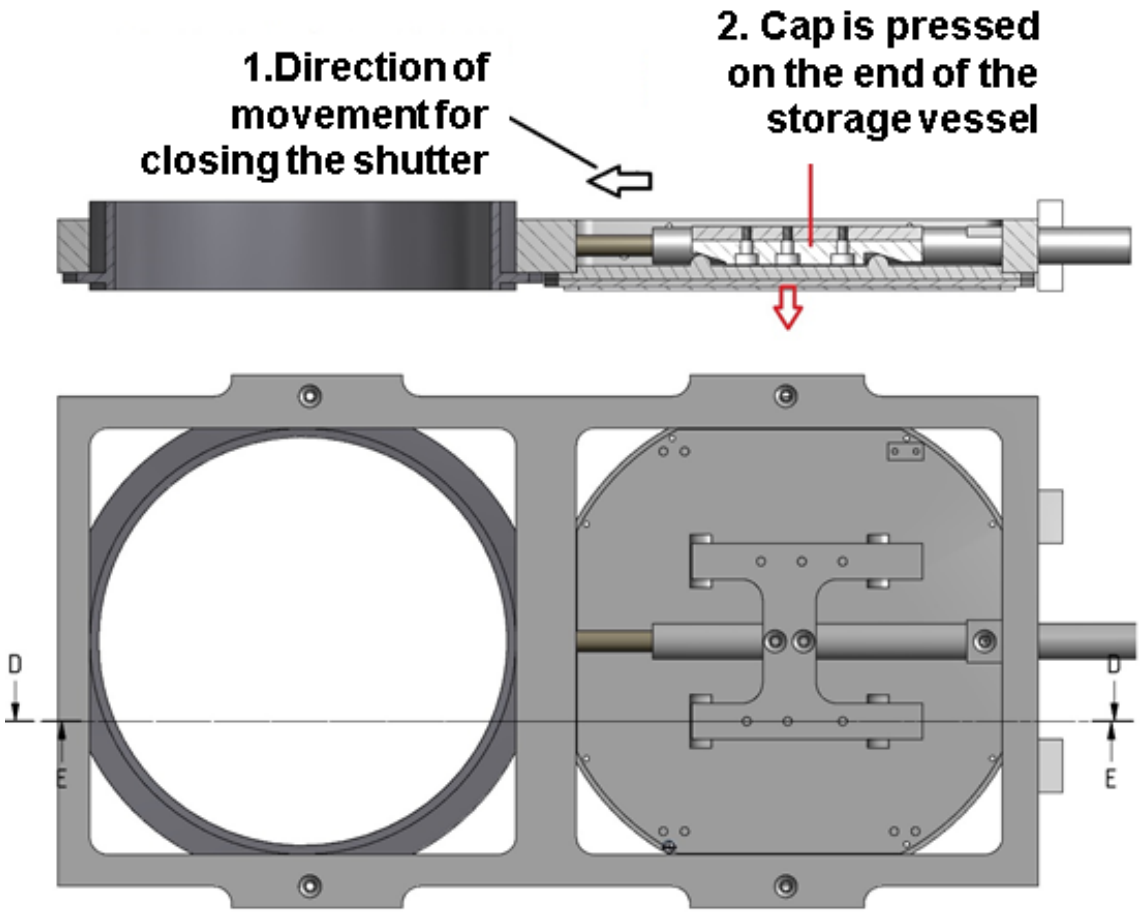

Figure A.2: Sketch of the slide of the self made shutters. First the carriage is moved in the closed position by pressed air cylinder and on the last mm of the movement the cap is pressed on the end of the storage vessel with a guide made of PVC (Polyvinylchlorid).

B Switch Characterization Setup

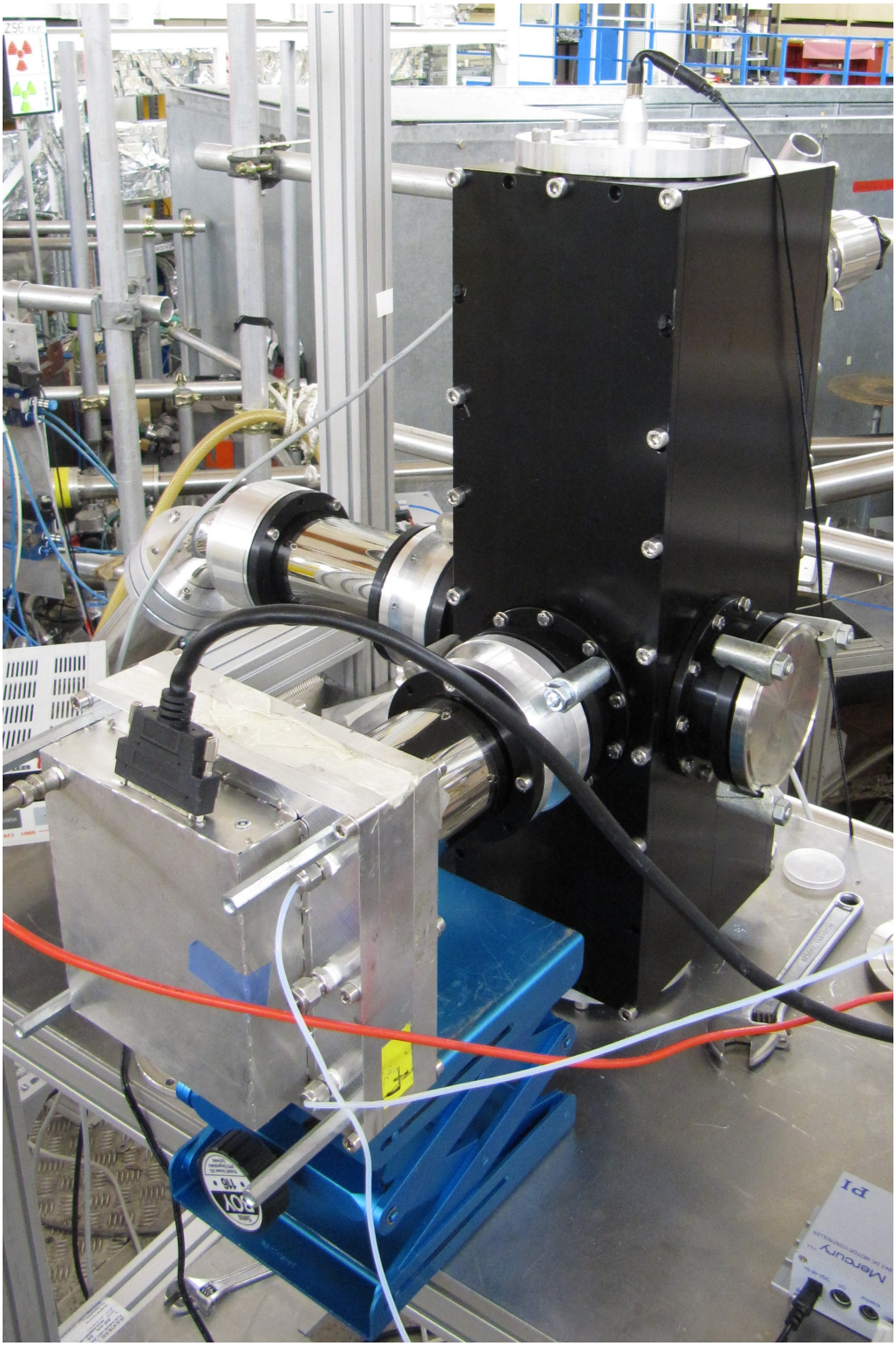

Figure B.1: Picture of the switch characterization setup. In the middle in black the switch. The neutrons come from the left and are detected with Cascade detector. Here the measurement of one of the 90° bends is shown.

C Bend Sections

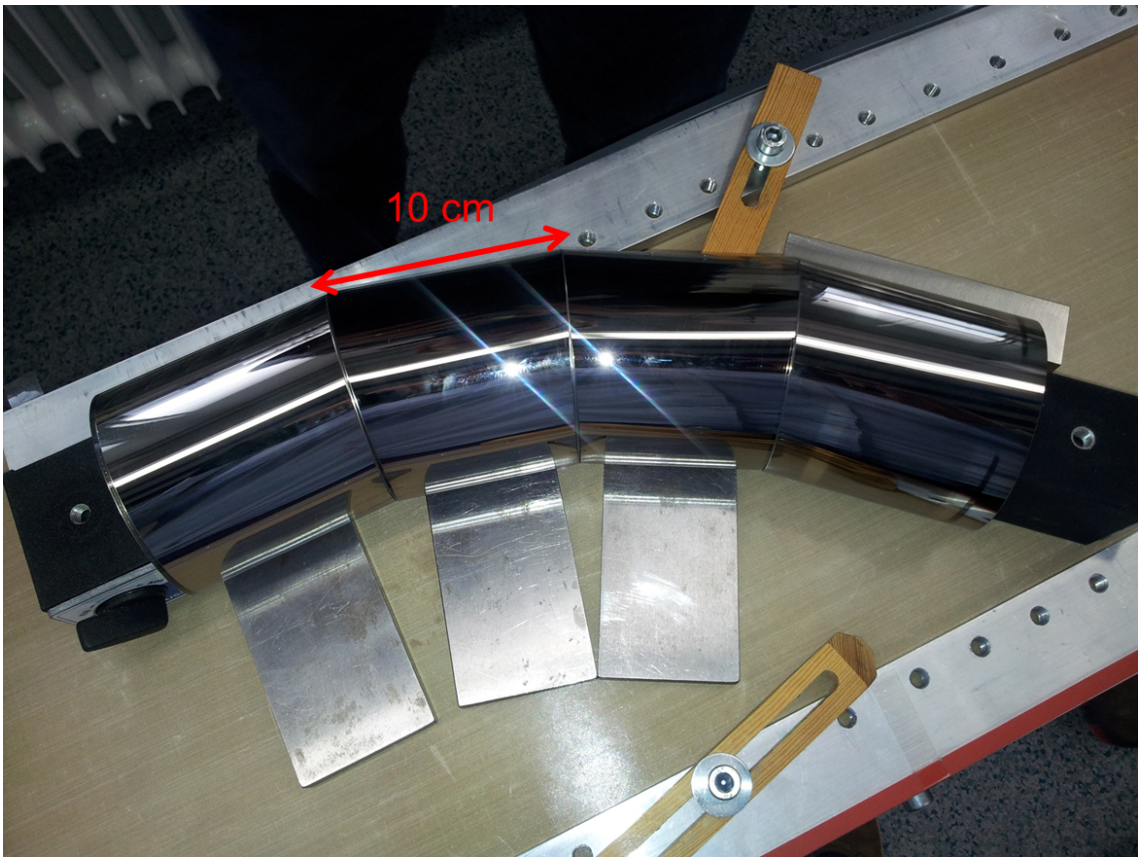

Figure C.1: Picture of a bend section with an inner diameter of 80 mm and a length of each segment of 10 cm at the outside of the bend. The bend has in sum an angle of 45°.

D Spin Flipper and Polarizers

D.1 Super Polarizer Layer Structure

Layer No.	[nm]	
1	15.3	Fe
2	11.7	Si
3	18.1	Fe
4	12.5	Si
5	22.6	Fe
6	13.3	Si
7	83.5	Fe
8	15.8	Si
9	128	Fe
10	25	Si

Table D.1: Layer structure of the super polarizer used for the nEDM measurement.

E Pictures of the Spin Flipper and Polarizer Characterization Measurements

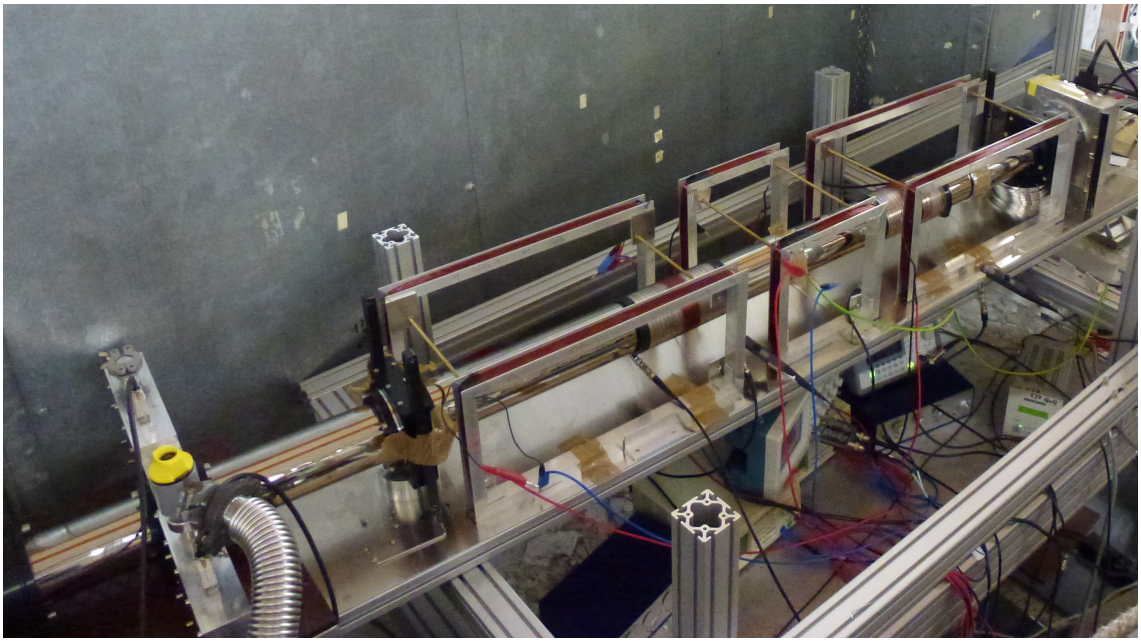

Figure E.1: Picture of spin flipper setup and polarizer test setup at the ILL in 2013. It shows all components described in Ch. 5.6

F Characteristics of the Superconducting Magnet

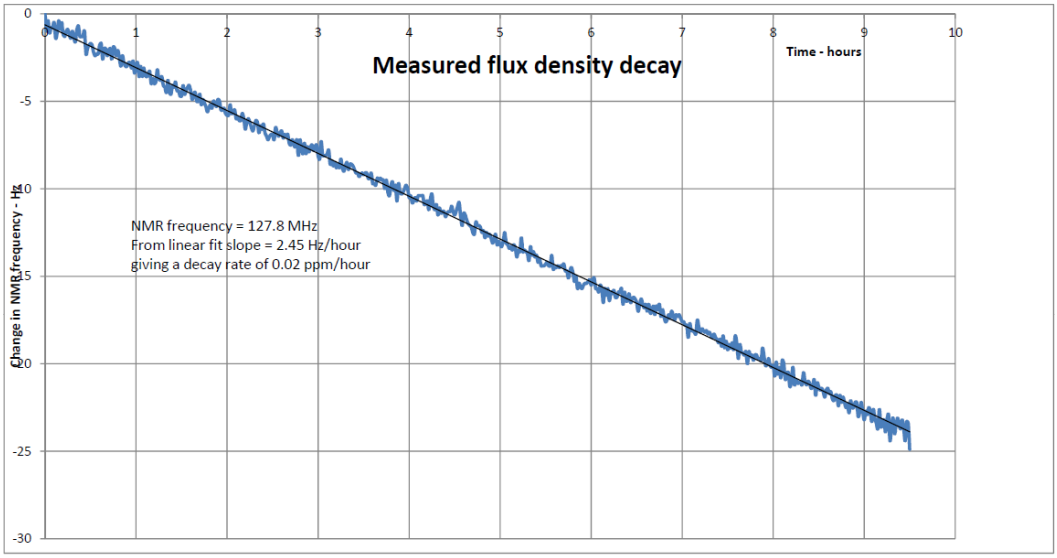

Figure F.1: Flux density decay of the superconducting magnet. Measured by Oxford Instruments.

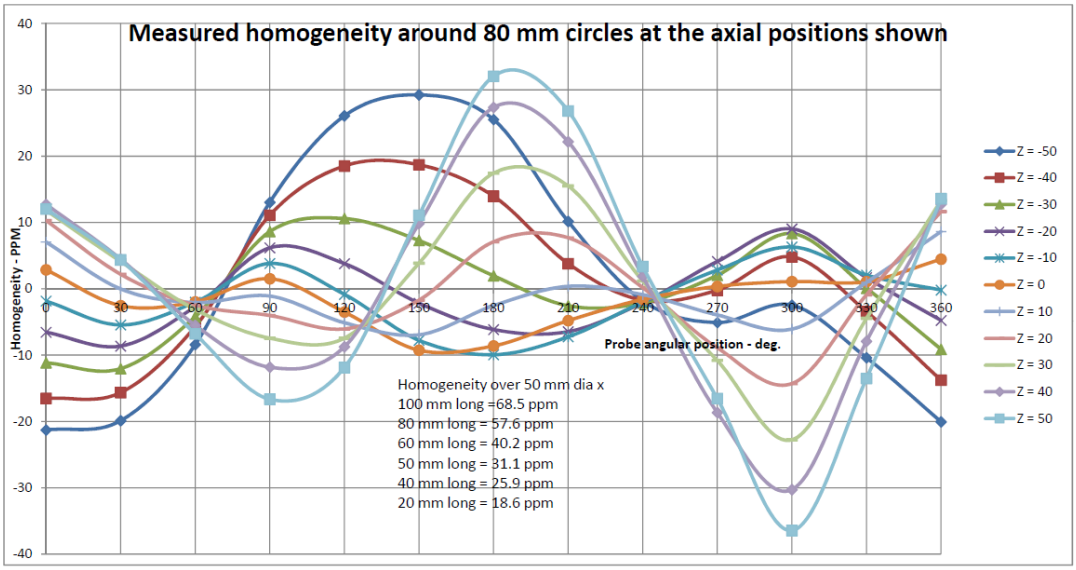

Figure F.2: Homogeneity around 80 mm cicles at the different axial positions for the superconducting magnet. Measured by Oxford Instruments.

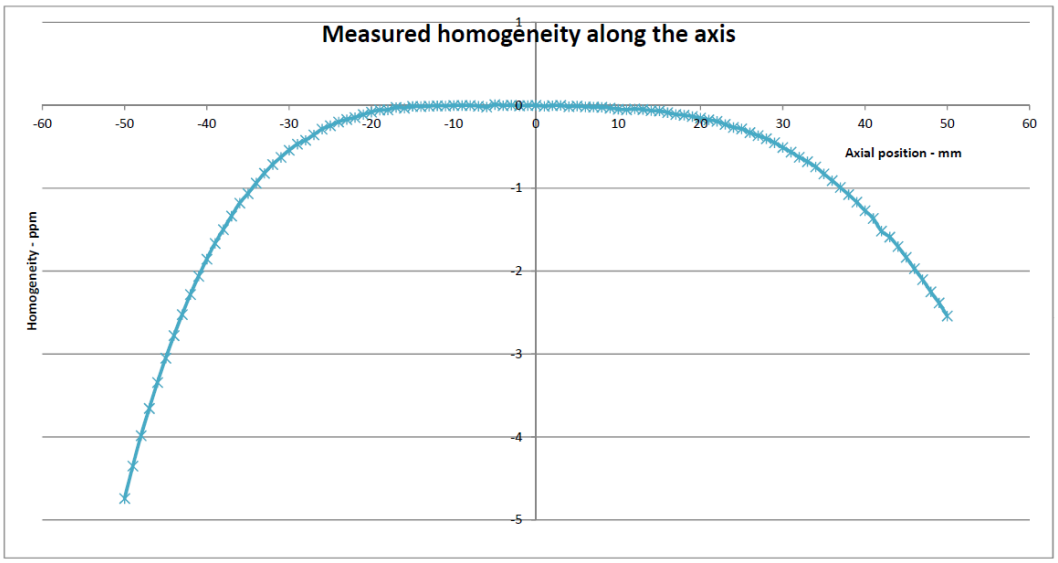

Figure F.3: Measured homogeneity along the neutron propagation axis for the superconducting magnet. Measured by Oxford Instruments.

G nEDM Test Measurements, Diagrams and Pictures

G.1 Data Acquisition Software Flow Charts

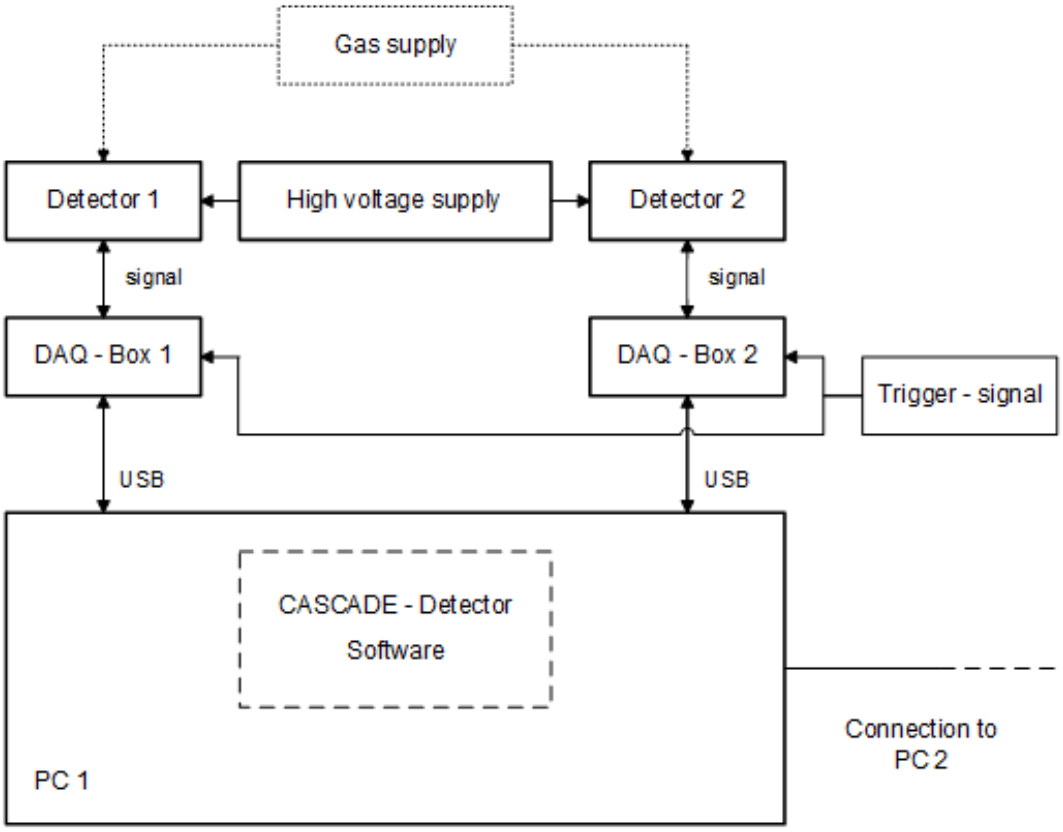

Figure G.1: Flow chart for PC 1 of the setup used for the characterization measurements. The shown components are described in detail in Ch. 6.1

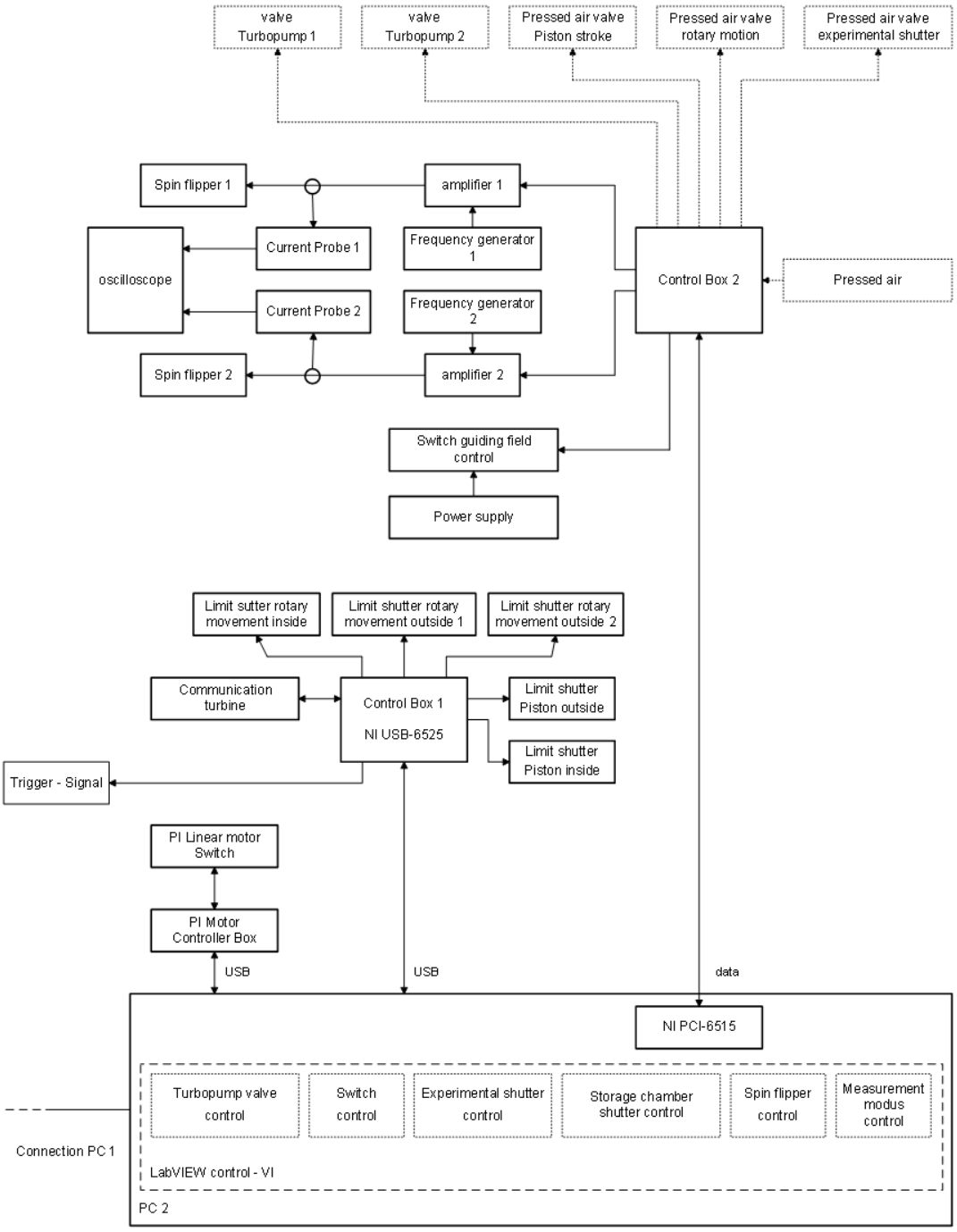

Figure G.2: Flow chart for PC 2 of the setup used for the characterization measurements. The shown components are described in detail in Ch. 6.1

G.2 Photos of the Test Setup

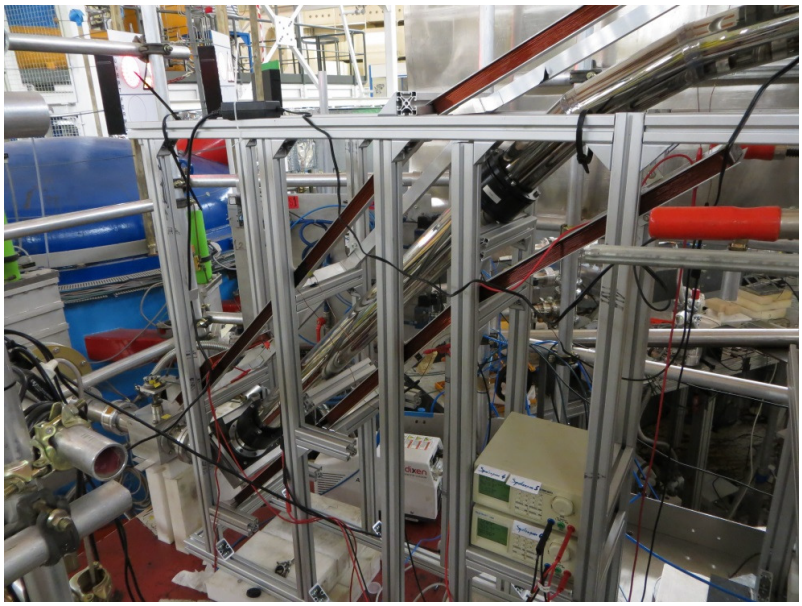

Figure G.3: Photo of the first 45 ° bend section with the at least 1 m rise with the rectangular guiding fields of the setup for the nEDM mockup test at the ILL.

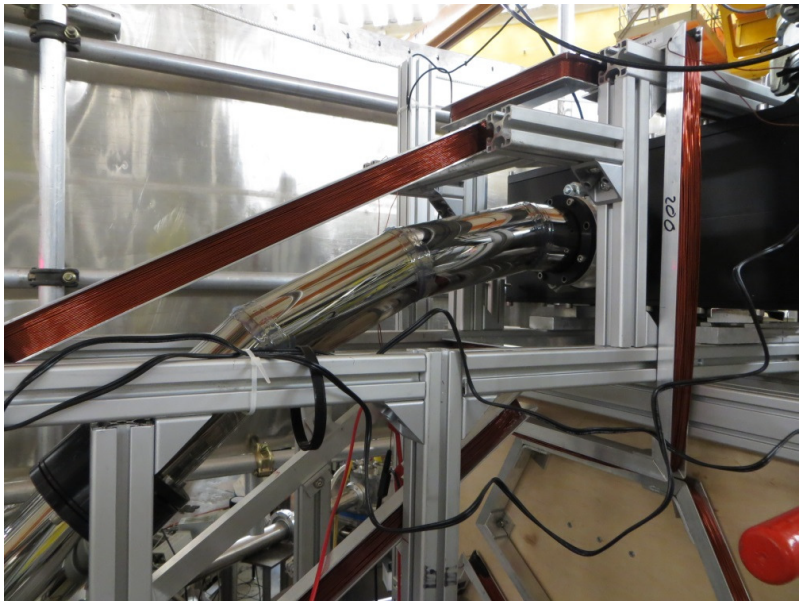

Figure G.4: Photo of the second 45 ° bend section with the switch and the guiding fields.

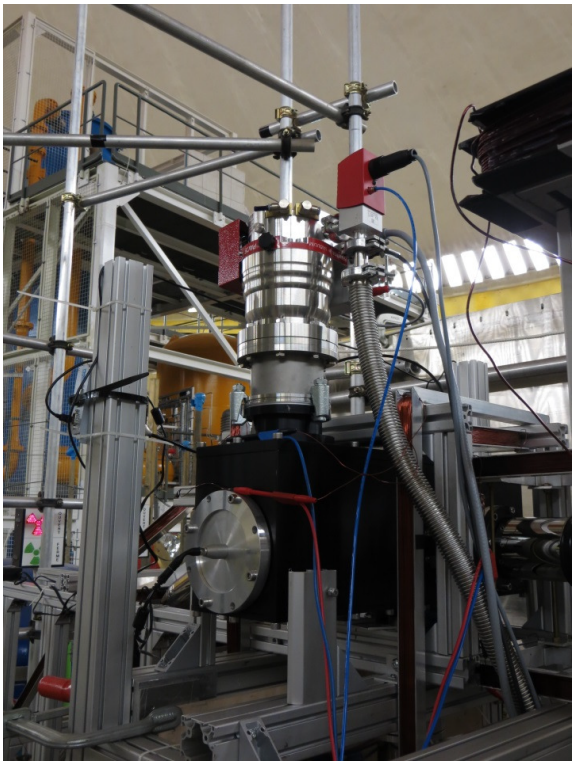

Figure G.5: Photo of the switch with an installed turbo molecular pump on top and the guiding fields

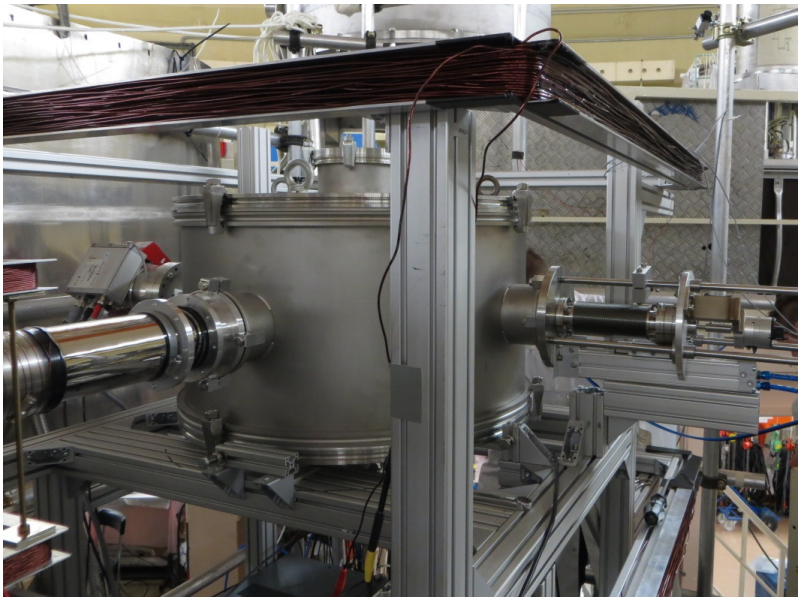

Figure G.6: Photo of the closed vacuum vessel with the 1.2 x 1.2 m Helmholtz field. On the left the outer part of the pressed air valve moving the piston stroke of the precession chamber shutter and the rotary motion to close the precession chamber plug.

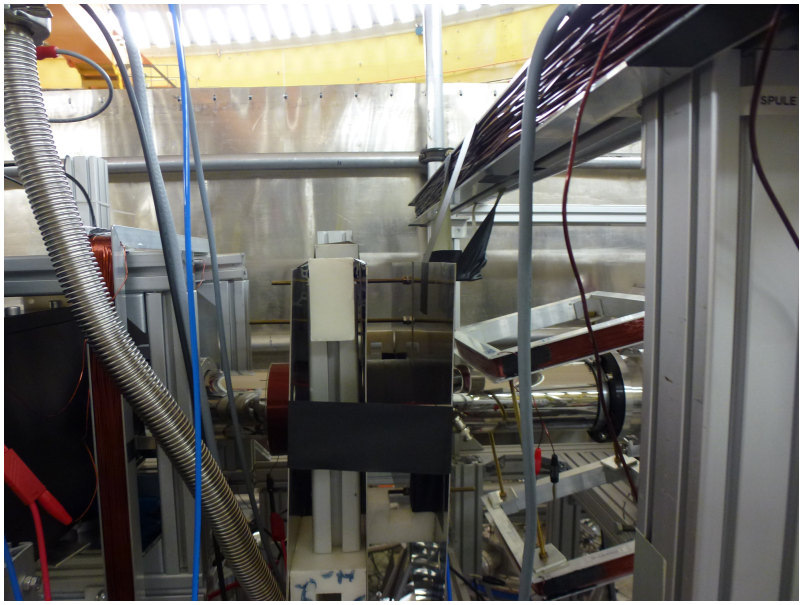

Figure G.7: Photo of the three μ metal plates installed at the feeding guide of the precession chamber. In Fig. 6.1 between (6) and (7).

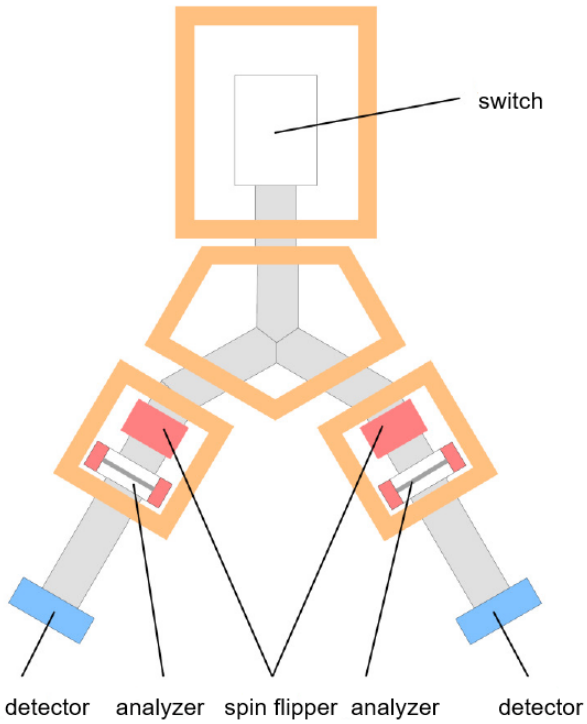

Figure G.8: Schematic drawing of the simultaneous spin analyzing system installed beyond the emptying arm of the setup. The description of the parts is like in Fig. 6.1. Taken from [124] Fig. 12.

G.3 Further Storage Curves

NiMo with Quartz before Leaning

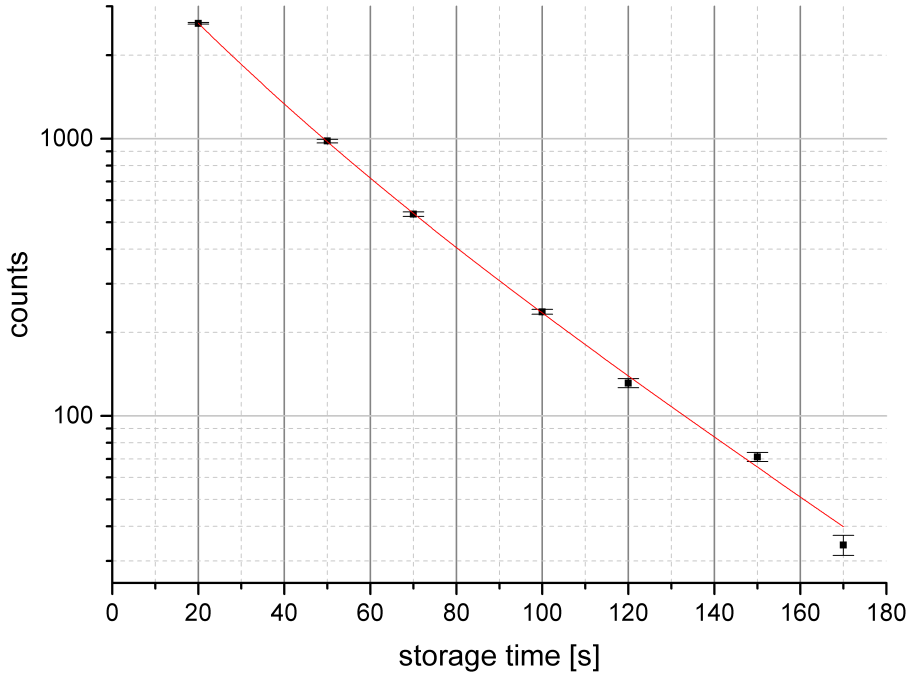

Figure G.9: Plot of the storage curve for NiMo coated electrodes and quartz insulator ring before cleaning and heating the quartz insulator ring. From the exponential decay fit t_1 is 21 ± 8 s and t_2 is 42 ± 7 s. The error bars arise from Poison statistics.

NiMo with Quartz after Contamination with Glass Shivers

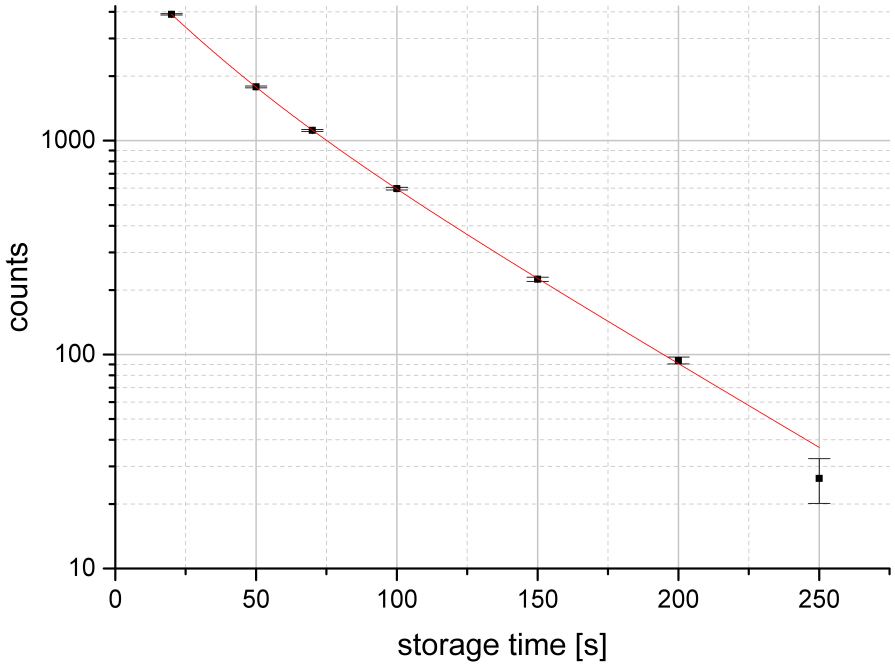

Figure G.10: Plot of the storage curve for NiMo coated electrodes and quartz insulator ring after the incident with the rectangular guide. From the exponential decay fit t_1 is $24 \pm 3\,\mathrm{s}$ and t_2 is $56 \pm 3\,\mathrm{s}$.The error bars arise from Poison statistics.

NiMo with dPE after Contamination with Glass Shivers

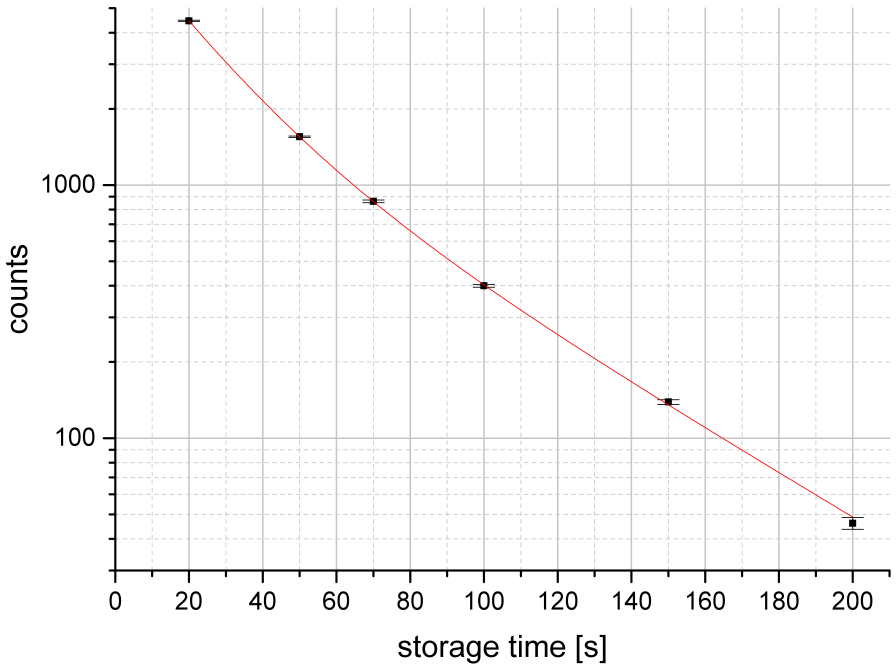

Figure G.11: Plot of the storage curve for NiMo coated electrodes and dPE coated insulator ring after the incident with the rectangular guide. From the exponential decay fit t_1 is $19 \pm 1\,\mathrm{s}$ and t_2 is $50 \pm 2\,\mathrm{s}$. The error bars arise from Poison statistics.

G.4 Storage Curves Statistics

NiMo(85/15 wt%) electrodes with quartz insulator before cleaning										
storage time	20 s	50 s	70 s	100 s	120 s	150 s	170 s			
No. measurements	10	5	5	10	5	10	4			
NiMo(85/15 wt%) electrodes with quartz insulator after cleaning										
storage time	20 s	50 s	70 s	100 s	150 s	200 s	250 s	300 s		
No. measurements	10	23	12	36	46	60	11	34		
NiMo(85/15 wt%) electrodes with quartz insulator after incident										
storage time	20 s	50 s	70 s	100 s	150 s	200 s	250 s			
No. measurements	8	8	14	14	15	14	1			
NiMo(85/15 wt%) electrodes with dPE insulator after incident										
storage time	20 s	50 s	70 s	100 s	150 s	200 s				
No. measurements	12	23	11	23	23	12				
Fomblin coated precession chamber										
storage time	20 s	50 s	100 s	150 s	200 s	250 s	300 s	350 s	400 s	450 s
No. measurements	12	12	11	10	10	14	17	19	19	17
storage time	500 s	550 s	600 s	650 s	700 s	750 s	800 s	850 s	900 s	
No. measurements	17	14	19	16	8	3	2	1	1	

Table G.1: Number of measurements for the different storage time in the different precession chamber configurations.

H Monte Carlo Simulations of the UCN Guide System Test

To analyze the measured TOF spectra in order to determine the defuse scattered neutrons in the system a Monte Carlo simulation is performed, basing on the already existing C code developed and described in detail in [42].
The geometrical model of the setup includes all components as in the test, beginning at the separation foil of the Turbine at the test beam line at the ILL and ending with the Cascade detector. A screen shot of the main panel with the guide system model of the full length is shown in Fig. H.1. The initial UCN spectrum is determined by six supporting points, for which the percentage of the spectrum for the respective velocity and the isotropy of the UCNs could be defined.
The velocity range of the UCNs is adapted to the measured spectrum and the range reached from 4.3 m/s to 20 m/s. For the interaction of the neutrons with the UCN guide walls standard specular and diffusive reflection laws are used. The diffuse reflection is considered by using the Knudsen law as next order reflection for UCN as described by [22]. In the simulation the diffuse reflection part of the guide system is variable and will be optimized for a measured spectrum. The loss per wall collision parameter calculated for the setup with the storage measurements is also used in this simulation as predefined. With this simulation it was possible to determine the percentage of diffuse scattered UCN in a long guide systems. More details on the simulation can be found in [42].

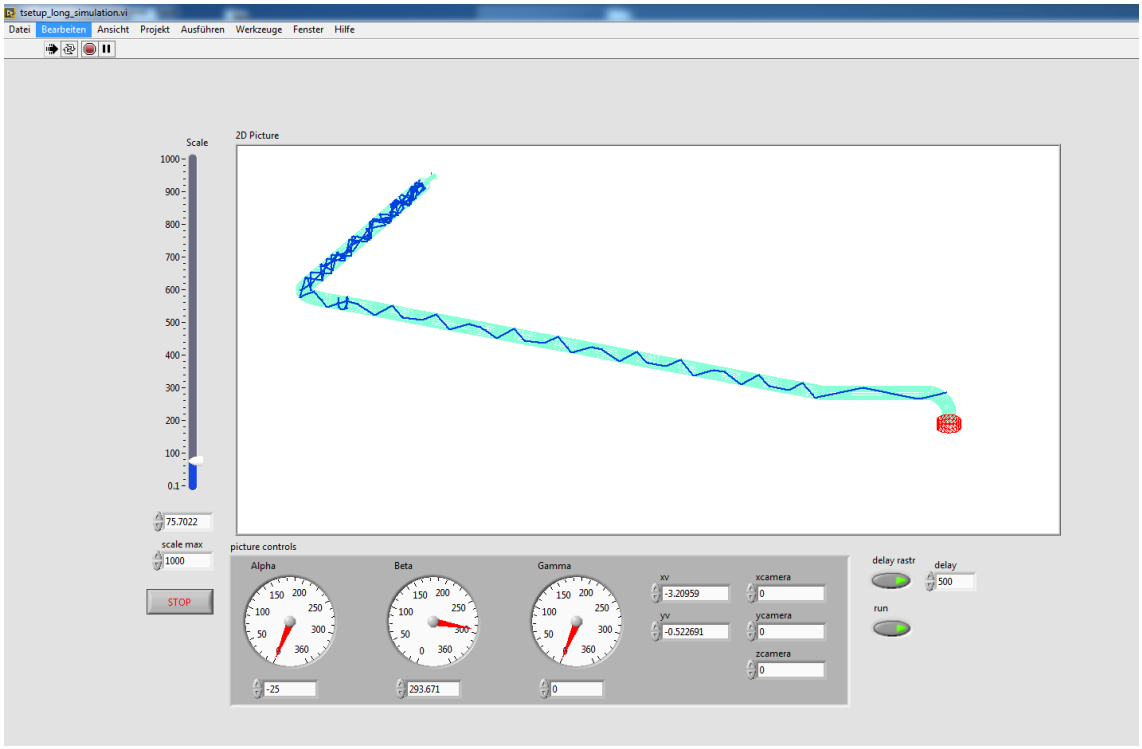

Figure H.1: Screen shot of the simulation main program with the model of the used guide system for the longest setup .

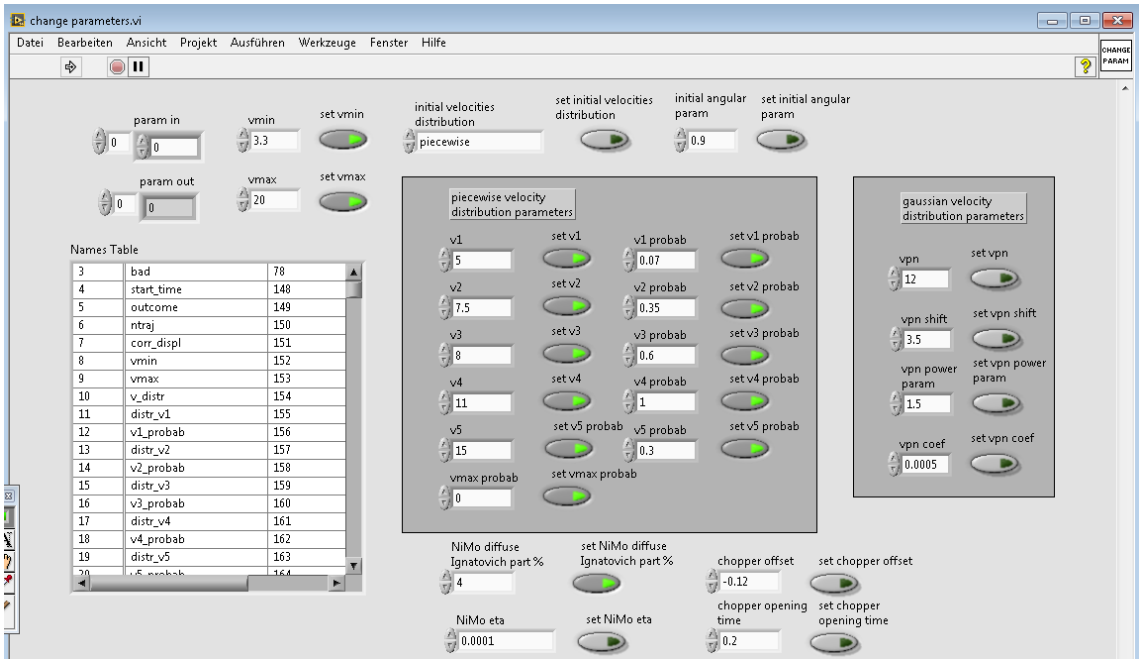

Figure H.2: Screen shot of the simulation parameter mask for the model of the used guide system for the longest setup.